Calculation of the Diffusion Tensor for the Galactic Magnetic Field and its Implementation in CRPropa

Berechnung des Diffusionstensors für das galaktische Magnetfeld und dessen Implementierung in CRPropa

Masterarbeit

im
Studiengang
„Master of Science“
im Fach Physik

an der Fakultät für Physik und Astronomie
der Ruhr-Universität Bochum

von
Patrick Reichherzer

aus
Ingolstadt

Bochum 2018

Abstract

Understanding the transport of energetic cosmic rays is among the most challenging topics in astrophysics. The complicated evolution of the cosmic ray distribution can be mathematically modeled by a diffusive process in the limit of large times. Consequently, diffusion is of fundamental importance in the transport of cosmic rays through partially ionized plasma. The transition from a ballistic to a diffusive-propagation regime is presented in direct numerical simulations and is used for the calculation of diffusion coefficients for homogeneous magnetic field lines B subject to turbulent perturbations b. The findings are compared with theoretical derivations of the parallel diffusion coefficient's dependencies on the energy and the fluctuation amplitudes in the limit of weak turbulence.

The present thesis shows that the widely-used extrapolation to high turbulence levels of the energy scaling for the parallel diffusion coefficient predicted by the quasi-linear approximation does not provide a universally accurate description in the diffusive-energy regime. It is highlighted that the numerically calculated diffusion coefficients are polluted for low energies due to missing resonant interaction possibilities of the particles with the turbulence. These findings form the basis for both the interpretation of the simulation results in the present thesis as well as a correction of the diffusion coefficient's energy dependency for data presented in previous studies. Agreement is found between the energy scaling in this thesis and that of previous studies after correcting the latter according to rules established in the present thesis.

Furthermore, theoretical predictions for the diffusion coefficient dependencies are developed for energies above the diffusive-energy regime and confirmed by simulation results. For these energies, the present study confirms agreement of the simulation data with classical theory, instead of agreement with quasi-linear theory. Based on the findings of the diffusion coefficient's dependencies on both the energy and the level of turbulence, the time of the transition from a ballistic to a diffusive-propagation regime can be calculated as a function of E and b/B.

This is an important step toward implementing a propagation software which is able to dynamically choose between solving the equation of motion and solving the transport equation for the modeling of cosmic ray transport so that high-energy extragalactic cosmic rays as well as Galactic cosmic rays can be consistently propagated within one framework. In addition, the propagation software will improve solving the transport equation, given the more realistic diffusion coefficient dependencies presented within the present thesis.

Zusammenfassung

Aktuell birgt der Ursprung der kosmischen Strahlung noch viele ungeklärte Rätsel, deren Erforschung durch die Beschreibung des Transports der kosmischen Strahlung ermöglicht wird. Die komplexe Entwicklung der kosmischen Teilchenverteilung kann durch einen Diffusionsprozess für lange Trajektorien mathematisch beschrieben werden. Folglich ist die Diffusion von grundlegender Bedeutung für den Transport der kosmischen Strahlung durch teilweise ionisiertes Plasma. Der Übergang von einem ballistischen zu einem diffusiven Energieregime wird anhand numerischer Simulationen veranschaulicht und zur Berechnung von Diffusionskoeffizienten für homogene Magnetfeldlinien B verwendet, die turbulenten Störungen b unterliegen. Die Ergebnisse werden mit theoretischen Herleitungen der Energie- und Magnetfeldabhängigkeiten des parallelen Diffusionskoeffizienten für schwache Turbulenz verglichen.

Die vorliegende Arbeit zeigt, dass die bisher angenommene Extrapolation der Energieskalierung hin zu hohen Turbulenzniveaus für den durch die quasi-lineare Näherung vorhergesagten parallelen Diffusionskoeffizienten keine genaue Beschreibung im diffusiven Energieregime liefert. Es wird gezeigt, dass die numerisch berechneten Diffusionskoeffizienten bei niedrigen Teilchenenergien Unsicherheiten aufgrund fehlender resonanter Wechselwirkungsmöglichkeiten der Teilchen mit der Turbulenz unterworfen sind. Diese Ergebnisse bilden die Grundlage sowohl für die Interpretation der Simulationsergebnisse in der vorliegenden Arbeit als auch für eine Korrektur der Energieabhängigkeit des Diffusionskoeffizienten für Daten in anderen Publikationen. Es wird, abgeleitet aus den neuen Erkenntnissen, eine Übereinstimmung zwischen der Energieskalierung in dieser Arbeit und der aus früheren Studien gefunden, nachdem diese gemäß den in dieser Arbeit gefundenen Bedingungen korrigiert wurde.

Darüber hinaus werden theoretische Vorhersagen für die Abhängigkeit der Diffusionskoeffizienten für Energien oberhalb des diffusiven Energieregimes entwickelt und durch Simulationsergebnisse bestätigt. Für diese Energien bestätigt die vorliegende Studie die Übereinstimmung der Simulationsdaten mit der klassischen Theorie und stellt damit eine Abweichung von der quasi-linearen Theorie fest. Basierend auf den Befunden der Abhängigkeiten des Diffusionskoeffizienten sowohl von der Energie als auch vom Turbulenz-niveau, kann die Zeit beim Übergang von einem ballistischen zu einem diffusiven Ausbreitungsregime als Funktion von E und b/B berechnet werden.

Diese Masterarbeit stellt einen wichtigen Schritt für die Realisierung des langfristigen Ziels dar, den Teilchentransport, welcher sowohl galaktischer als auch extragalaktischer Natur sein kann, einheitlich und in sich konsistent zu beschreiben.

Contents

1 | Introduction

When I meet God, I am going to ask him two questions: Why relativity? And why turbulence? I really believe he will have an answer for the first.

–*Werner Heisenberg*

Turbulence is the most important unsolved problem of classical physics.

–*Richard Feynman*

The cosmic ray composition above GeV energies is dominated by protons, followed by a smaller contribution from heavier nuclei. Electrons and positrons comprise only a billionth of interstellar particles by number [1]. The acceleration of cosmic rays up to those energies is described by Fermi mechanisms and is based on the accumulation of individual acceleration and escape processes in turbulent magnetic fields as they occur at collisionless shock fronts, leading to a power-law energy spectrum of E^{-2}. Observations of the cosmic ray spectrum suggest, however, a broken power law with three different regimes above 10^{15} eV [2–4]. The first spectral steepening appears at the so called 'knee' around $3{\cdot}10^{15}$ eV [2], followed by a flattening of the spectrum at the 'ankle' at around 10^{18} eV [4]. A change in acceleration site or mechanism [5] as well as different propagation effects from the source to its detection have been postulated to account for these features.

Scattering by magnetic fields is not only responsible for the most important acceleration mechanism but also provide the predominant transport mechanism based on resonant scatter processes with small-scale magnetic turbulence in which cosmic rays exchange energy and momentum with the prevailing medium. Cosmic rays are isotropized primarily due to those magnetic fluctuations. The isotropic arrival distributions together with the limited confinement due to deflections caused by the Galactic magnetic field constrain the cosmic ray energy for which a Galactic origin can not account. One of the most pressing questions relates to the exact transition from Galactic to extragalactic cosmic rays [6, 7]: what is the relation to the aforementioned spectral features – namely, knee and ankle – and where does this transition take place exactly?

The development of simulation frameworks for different regimes – low-energy, Galactic and high-energy extragalactic propagation – has significantly advanced the understanding of cosmic ray physics over the last decade [8–10]. CRPropa is a publicly available propagation software that provides both complementary approaches in two different modules of the program – solving the equation of motion and solving the transport equation – for the modeling of cosmic ray transport [5] such that high-energy extragalactic cosmic rays as well as Galactic cosmic rays can be propagated within one framework. The connection between those two complementary methods is facilitated by the spatial diffusion coefficients. The diffusion coefficients characterize the cosmic ray propagation in a partially turbulent magnetic field [11] and the diffusion coefficient's energy and magnetic field dependencies. Solving the

equation of motion, one can thus calculate the diffusion coefficient, such that its dependencies can then be used to solve the transport equation [12]. Consequently, understanding of the diffusion coefficient poses a fundamental challenge in the modeling of cosmic ray transport in turbulence [11, 13–17].
This fact bears directly on many astrophysical processes, such as the efficiency of Fermi acceleration mechanisms, the penetration of low-energy cosmic rays in the heliosphere [15, 18], the confinement of galactic cosmic rays in the interstellar magnetic field [5, 11, 19]. In Appendix A, this thesis presents an illustration of the physical implications that the exact energy dependency of the diffusion coefficient has for processes within active galactic nuclei (AGNs) [20, 21], in particular radio galaxies – AGNs with mis-aligned jets. AGNs are capable of accelerating particles and therefore contribute to the high-energy cosmic ray spectrum [20–24]. Debate continues about the detailed cosmic ray acceleration mechanisms within its jets and accretion disc and the resulting spectral index Γ_p of the accelerated cosmic ray energy spectrum [20, 21]. The first Section intends to cover the whole life span of cosmic rays starting from the description of the acceleration mechanisms, followed by an introduction to the transport of those particles and finishing with detection and observation methods.

1.1 Cosmic Rays

Cosmic rays were discovered more than a century ago and have been studied extensively since then. Some important results regarding the acceleration of cosmic rays at their sources, their transport toward Earth and their detection will be described here.

1.1.1 Acceleration

Fermi [25] suggested that cosmic rays gain their energy from large-scale fluid motion during the accumulation of individual acceleration and escape events in turbulent magnetic fields. The repeated processes of small accelerations with a gain $\Delta E = E \cdot \xi$ inevitably lead to a power-law energy spectrum (for the detailed derivation see Appendix B)

$$N \propto E^{-q} \Rightarrow \frac{dN}{dE} \propto E^{-q-1}, \tag{1.1}$$

where q is defined as $q \approx P_\mathrm{esc}/\xi$ and ξ denotes the energy gain factor and P_esc denotes the escape probability of the acceleration region in each encounter. The efficiency of the acceleration process on total is therefore depending on ξ and P_esc.
The second-order Fermi mechanism focuses on random motion through the turbulent fields, a scenario found in interstellar clouds [26]. Each acceleration cycle consists of an encounter between a cosmic ray and a cloud, in which the particles diffuse by collisionless scattering on the turbulent magnetic field (see Chapter 2 for details of the diffusion process). The acceleration cycle finishes with the escape of the particle in a random direction due to the diffusion within the cloud, leading either to an energy gain during a 'head-on' interaction or to an energy loss for a 'tail-on' encounter. The average cosmic ray energy gain is still positive, because due to the motion of the cloud through the interstellar medium (ISM), head-on encounters happen more frequently than tail-on encounters. Theoretical results point to an efficiency that is correlated with the cloud velocity. These results show that the average energy gain factor ξ for a cosmic ray of speed c during an interaction with a cloud of speed u results in $\xi \approx \frac{3}{4}\left(\frac{u}{c}\right)^2$. This scaling can be understood intuitively by taking under consideration the average fractional energy exchange for each encounter, together with the excess of head-on over tail-on encounters, which are both of order u/c. The $(u/c)^2$ dependency of the energy gain factor is responsible for the name second-order Fermi acceleration.

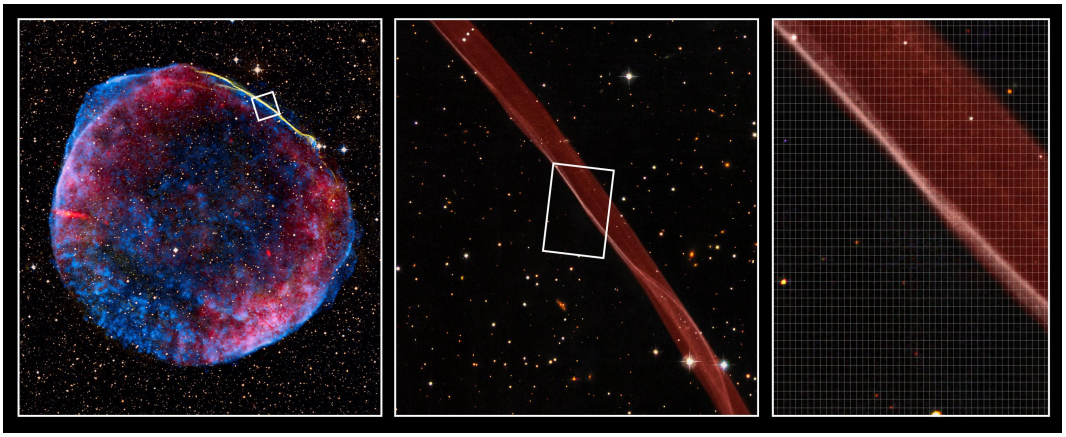

Figure 1.1: Observations by ESO [27] of a supernova remnant. The image on the left shows the entire SN 1006 supernova remnant. Data from the Very Large Array and Green Bank Telescope correspond to the red color, and data from the Chandra X-ray Observatory are plotted in blue. The yellow part is based on observations with the Curtis Schmidt optical telescope, while the Digitized Sky Survey adds the orange color to the images. The second and third panels each correspond to the boxed region of the previous panel. Overall, a shock-front is presented as discussed in the text.

Much attention has been paid to the first-order Fermi mechanism [28–30] with a u/c dependency of the energy gain factor, which occurs, for example, for collisionless shock fronts, as shown in Fig. 1.1. This mechanism is also based on turbulent fields moving with a bulk velocity, however, the shock front is taken to stretch to infinity [31]. Consequently, particles can only escape in the moving direction of the shock front. This presents a more effective acceleration mechanism compared with the second-order Fermi acceleration. The geometry of the plane shock is shown in Fig. 1.2 and consists of an upstream region with speed u_1 ahead of the shock and a downstream region with speed u_2 behind the shock. The first-order efficiency of this acceleration mechanism is based on the fact that the turbulent fields on one side of the shock always seem to move towards a particle on the opposite side of the shock. As a consequence, as soon as a particle crosses the shock, it will gain energy during a head-on encounter. The energy gain factor therefore reads

$$\xi \approx \frac{3}{4}\frac{u}{c}, \tag{1.2}$$

where $u = u_2 - u_1$ is the average speed of the shock in the laboratory frame. The escape probability P_{esc} in this context is defined as the flux $F_{\mathrm{CR}}^{\mathrm{esc}}$ of particles, for which the velocity component in the direction of the shock is larger than the shock velocity, divided by the isotropic comic ray flux in the upstream region which is projected onto the plane shock front $F_{\mathrm{CR}}^{\mathrm{u}\to\mathrm{d}}$

$$P_{\mathrm{esc}} = \frac{F_{\mathrm{CR}}^{\mathrm{esc}}}{F_{\mathrm{CR}}^{\mathrm{u}\to\mathrm{d}}} = \frac{u_2\rho_{\mathrm{CR}}}{\int_0^1 \mathrm{d}\cos\Theta \int_0^{2\pi} \mathrm{d}\Phi F_{\mathrm{CR}}^{\mathrm{iso}} \cos\Theta} = \frac{u_2\rho_{\mathrm{CR}}}{c\rho_{\mathrm{CR}}/4} = \frac{4u_2}{c}. \tag{1.3}$$

The ratio P_{esc}/ξ is estimated by using the ideal magneto-hydrodynamic equations. The Rankine-Hugoniot [32] relations supply a description of the jump conditions between the upstream and the downstream region. For strong shocks, it yields

$$\frac{u_1}{u_2} = 4, \tag{1.4}$$

such that the differential energy spectrum of cosmic rays follows a power law with spectral index 2,

$$N(E)\,\mathrm{d}E \propto E^{-2}\mathrm{d}E. \tag{1.5}$$

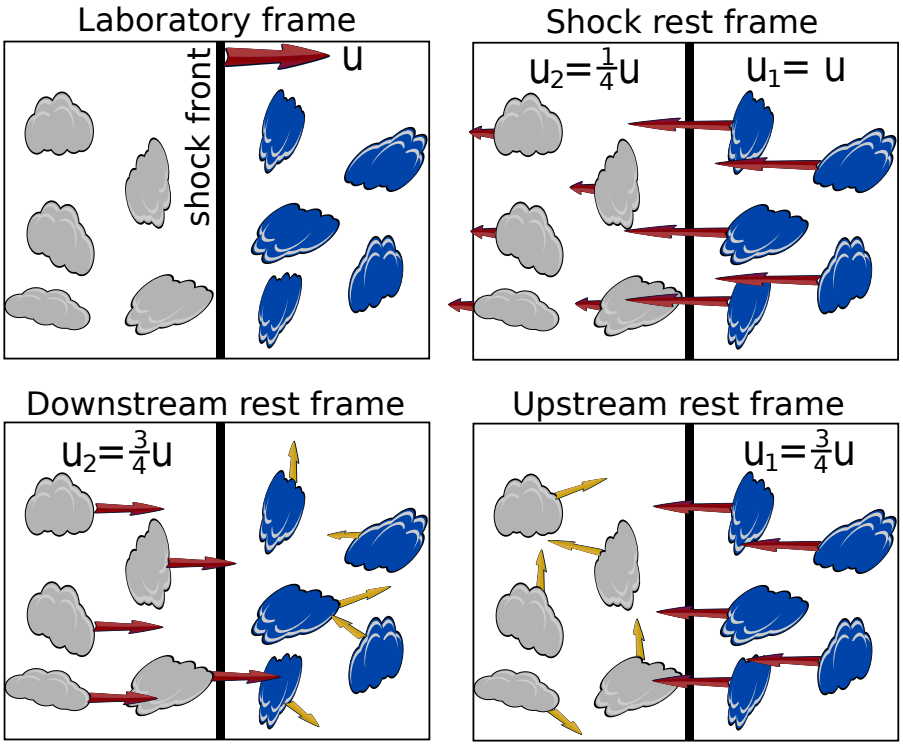

Figure 1.2: Geometry of a plane shock wave with an upstream region with speed u_1 ahead of the shock and a downstream region with speed u_2 behind the shock, created with [33]. Each panel presents the system in a different reference frame as denoted in the heading. When particles that are moving randomly on the downstream side in the downstream rest frame cross to the upstream side, they will gain energy during a head-on encounter (bottom on the left panel), because the clouds seems to come all towards the particle in its rest frame. The same argument is true for particles crossing to the opposite side of the shock as presented in the right panel on the bottom.

1.1.2 Transport

This thesis focuses on the diffusive transport of cosmic rays. However, for completeness, the two complementary propagation descriptions are presented here:

- **Single-particle approach**: The trajectory of a test particle within a magnetic field is described solely by the Lorentz force. This offers an explicit description of particle trajectories. The particles are treated individually and do not interact with each other. Practical implementations of this approach tend to be computationally intense.
- **Multi-particle approach**: The particle evolution in phase space is described under the assumption of a collisionless plasma by the Vlasov equation and leads to the Fokker-Planck equation. These derivations are discussed shortly in Chapter 2 when only taking diffusive processes into account. A more general form of the transport equation for an isotropic distribution in momentum reads

$$\frac{\partial f}{\partial t} + \overbrace{v_i \frac{\partial f}{\partial x_i}}^{\text{Advection}} = \overbrace{\frac{\partial}{\partial v_i}\left(D_{ij}\frac{\partial f}{\partial x_j}\right)}^{\text{Spatial Diffusion}} + \overbrace{\frac{1}{p^2}\frac{\partial}{\partial p}\left(p^2 D_{pp}\frac{\partial f}{\partial p}\right)}^{\text{Momentum Diffusion}} + \underbrace{\frac{1}{3}\frac{\partial v_i}{\partial x_i}\frac{\partial f}{\partial \ln p}}_{\text{Adiabatic Energy Changes}} + \underbrace{Q(\vec{x},p,t)}_{\text{Source}}. \tag{1.6}$$

Diffusion

The fluctuations b due to plasma waves enable scattering processes of the cosmic rays and therefore lead to a random walk. The structure of the turbulent magnetic field is therefore crucial for the diffusion process. Without drift terms and in the local frame of the magnetic field line, the diffusion tensor is diagonal. A non-isotropic distribution introduces additional (non-diagonal) terms in the diffusion coefficient. The turbulent power spectrum $G(k)$ follows a power law with a specific index α and the minimum wave vector k_{low}

$$G(k) \propto \left(\frac{k}{k_{\mathrm{low}}}\right)^{-\alpha} . \tag{1.7}$$

The index $\alpha = -5/3$ is used for the turbulent magnetic field according to *Kolmogorov diffusion* which is expected for example in extragalactic jets [15]. The turbulent power spectrum $G(k)$ can be specified to derive analytical approximations for the energy dependency of the diffusion coefficients as presented in detail in Chapter 2 for different energy regimes.

1.1.3 Detection

The direct observation of cosmic rays is only feasible above Earth's atmosphere, because they interact inelastically with the atmosphere and produce a shower of secondary particles. The cosmic ray flux decreases as a power-law, space-bound detectors at some point have too small effective areas to collect enough particles. The indirect detection of cosmic rays is possible at Earth: The fact that cosmic rays generate an air shower as soon as they strike Earth's atmosphere can be used to reconstruct their properties by measuring the air shower at ground. This is done, for example, by the Pierre Auger Observatory [34]. Further indirect observation methods are used in IceCube [35] and CTA [36], where neutrinos and gamma rays are observed that originate from interactions of highly energetic cosmic rays in the vicinity of their source.

1.1.4 Challenges

Even though there have been many improvements in the area of detection, simulation and analytical theory, as presented above, there are still many remaining unsolved questions concerning the interpretation of cosmic ray data. The most challenging problems are discussed below.

Issue 1 – Features in Energy Spectrum Data from the Telescope Array and the Pierre Auger Observatory together with many more observation sites have been accumulated and analyzed, resulting in the comprehensive knowledge of the cosmic ray energy spectrum presented in Fig. 1.3. The differential flux $\mathrm{d}N/\mathrm{d}E$ measured in [GeV cm^2 sr s]$^{-1}$ in the three different energy regimes can be approximated as [2–4]

$$\frac{\mathrm{d}N}{\mathrm{d}E} \propto \begin{cases} E^{-2.6\pm0.04} & \text{for } E \lesssim 10^{15}\,\mathrm{eV} \\ E^{-3.0\pm0.05} & \text{for } 10^{15}\,\mathrm{eV} \lesssim E \lesssim 10^{18}\,\mathrm{eV} \\ E^{-2.65\pm0.3} & \text{for } 10^{18}\,\mathrm{eV} \lesssim E \end{cases} . \tag{1.8}$$

A lot of research has been done to explain the observed power laws [2–4, 37, 38]. There is some evidence that the acceleration processes themselves already provide power laws.

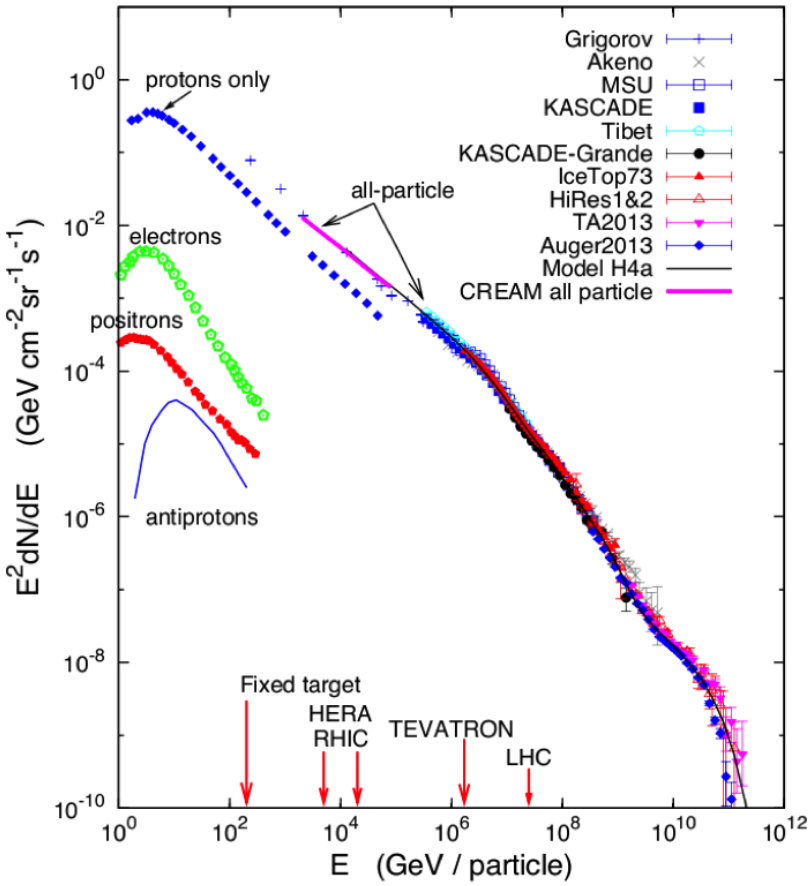

Figure 1.3: Spectrum of cosmic rays at Earth taken from [39]. Data from different experiments are accumulated as illustrated in the legend.

It is believed that the measured energy spectrum results from the combination of particle acceleration and diffusive transport [4, 37, 38].

Issue 2 – Origin Basic assumptions regarding the cosmic ray confinement in magnetic fields can be used to deduce possible acceleration sites and origins. Sources can only accelerate cosmic rays as long as the latter are confined within the magnetic field of the source. This basic assumption yields an upper limit $E_{\mathrm{p,max}} = ZeBLc$ for the energy of particles from that source, which is known as the Hillas criterion. This argument, together with the mostly isotropic arrival directions of the cosmic rays, inevitably leads to the conclusion that particles above a certain energy can not originate from within the Milky Way. Instead, acceleration for higher-energy cosmic rays has to occur in an extragalactic source. The exact energy for this transition is subject of current research [40–43].
Possible sources for Galactic cosmic rays are supernova remnants (SNRs). The magnetic shock fronts expand into the surrounding interstellar medium resulting in an acceleration based on the first-order Fermi mechanism. White dwarfs as well as neutron stars are additional candidates for sources of Galactic cosmic rays.
Promising candidates for extragalactic cosmic rays are AGNs. Assuming the central region of order $R \sim 10^{13}\,\mathrm{cm}$ to accommodate a black hole of mass $M_{\mathrm{bh}} \sim 100\,M_{\odot}$, the equipartition magnetic field in the central region yields $B \sim 300\,\mathrm{G}$ [44, 45]. Cosmic rays can be accelerated and confined up to $E_{\mathrm{p,max}} \sim 150\,\mathrm{EeV}$ [44]. Jets within radio loud galaxies present another possible acceleration site of cosmic rays up to energies of $E_{\mathrm{p,max}} \sim 300\,\mathrm{EeV}$, given that the product of BR in a typical jet yields $\sim 0.3\,\mathrm{G\,pc}$ [45, 46]. Similar maximal energies can be found within hot spots and bow shocks at the termination of the AGN jets with the intergalactic medium [46–49].

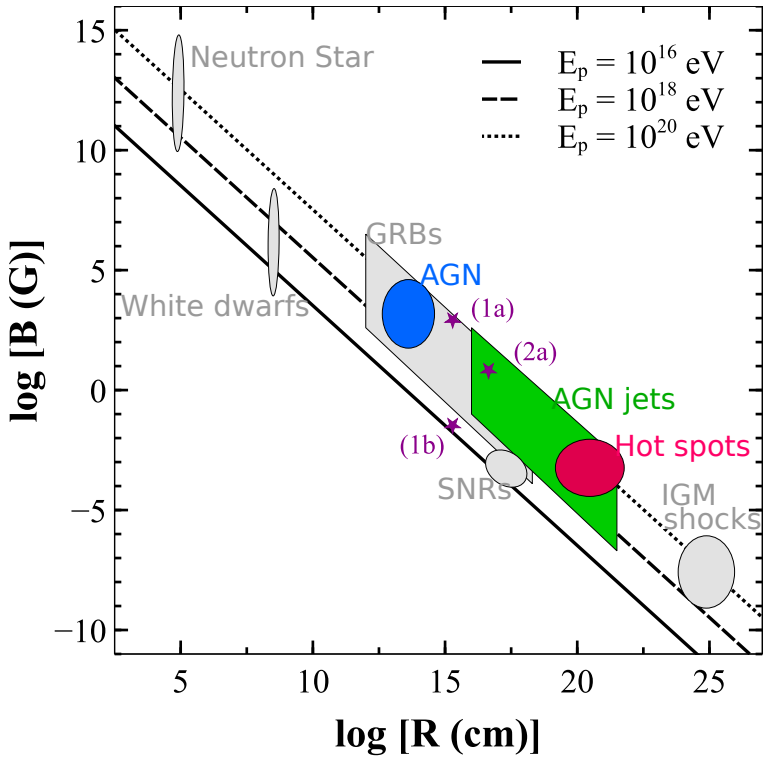

Figure 1.4: Updated Hillas (1984) diagram adapted from Fig. 11 in [45]. Magnetic field strength versus radius for possible sources which are able to confine accelerated protons. If cooling effects are ignored, the maximum energy $E_{\mathrm{p,max}}$ is proportional to the product of the size of the accelerating region and the magnetic field. The possible acceleration sites for extragalactic cosmic rays are AGNs (center, jets and hot spots), GRBs and IGM shocks. The most promising acceleration sites for Galactic cosmic rays are supernova remnants (SNRs).

Gamma ray bursts (GBRs) lead to the formation of additional shock regions and are therefore potential acceleration candidates. Furthermore, intergalactic magnetic (IGM) shocks could accelerate cosmic rays to energies above 10^{20} eV [50]. All of these possible sources are capable of accelerating the protons up to energies around 10^{20} eV. Based on the assumed magnetic field strengths B and the radius R of each possible cosmic ray source, the upper limits of the energies to which protons can be accelerated within these sources are presented in Fig. 1.4.

Issue 3 – Arrival Directions The cosmic ray arrival directions at Earth depend on the positions of the sources and transport effects during their travel towards Earth. Based on the limitation of this argument to distant sources, resulting in long trajectories of the cosmic rays, the interaction with turbulent magnetic fields constitutes a diffusive process in which the particles are decorrelated completely from their initial direction when they are detected at Earth. The influence of this effect regarding the isotropization depends on the energy regime of the particle. There are two dominant regimes: the diffusive-energy regime, in which the particles scatter resonantly within the turbulent magnetic field, and the ballistic-energy regime without those resonant interactions and thus less isotropization of arrival directions. This thesis, however, suggests a further classification within the ballistic-energy regime regime – namely, the intermediate-energy regime and the high-energy regime. In the latter, more efficient isotropization of arrival directions occurs than previously expected [11, 14, 15, 17, 51–53]. More details on this approach will be provided in Chapter 2. Considering the limit of short trajectories caused by surrounding sources, a local density gradient is present as soon as the sources are distributed anisotropically around the observer. In such a case, a net cosmic ray flux $\vec{J}_{\mathrm{CR}}$ is predicted

[54, 55]

$$\vec{J}_{\mathrm{CR}} = -\kappa_{\parallel}\vec{\nabla}_{\parallel}n - \kappa_{\perp}\vec{\nabla}_{\perp}n + \kappa_{\mathrm{H}}\frac{\vec{B}}{B} \times \vec{\nabla}n, \tag{1.9}$$

where $\kappa_{\parallel}$ and $\kappa_{\perp}$ denote the parallel and perpendicular diffusion coefficient, respectively, $\vec{B}$ the regular background field and n the cosmic ray density. In addition, κ_{H} denotes the Hall diffusion coefficient, which can be interpreted as a drift of cosmic rays in the large-scale guide magnetic field [56, 57]. It represents the antisymmetric term of the general diffusion coefficient

$$\kappa_{ij} = (\kappa_{\perp} - \kappa_{\parallel})\frac{B_i B_j}{B^2} + \kappa_{\perp}\delta_{ij} + \kappa_{\mathrm{H}}\epsilon_{ijk}\frac{B_k}{B}. \tag{1.10}$$

Mathematically, the cosmic ray flux $\vec{J}_{\mathrm{CR}}$ results in such a dipole anisotropy with a dipole vector $\vec{d}_{\mathrm{CR}} = -3\vec{J}_{\mathrm{CR}}/n$. Such dipole has been detected, with changing amplitude, but constant dipole vector direction at energies between TeV and PeV [58]. Above PeV-energies, both the direction of the dipole vector and the amplitude change [58]. The correctional between certain sources and local anisotropies is still subject of current research and scientific discussion as summarized, for example, in [55, 59].

Issue 4 – Composition For low-energy Galactic cosmic rays, a comparison of their composition with that of the Sun indicates the similarity of a higher abundance of particles with an even atomic charge Z compared to nuclei with an odd Z. It is believed that this is a result of the stellar nucleosynthesis in which He is burned. Besides this common feature of the solar and cosmic ray compositions, there are some differences:

- The acceleration regions of cosmic rays have a large ionization potential of H and He and thus lead to a lower abundance in cosmic rays relative to the solar composition.
- There is a higher abundance of lighter elements in the cosmic ray composition in comparison with that of the solar system, caused by interactions of cosmic rays with the interstellar medium. Spallation describes the process in which heavier elements produce lighter nuclei during interactions. That is the reason for the higher abundance of the lighter elements from Li to B of the cosmic ray composition.

The latter difference originates from the transport of the cosmic rays, while the former difference is caused by the source injection.

1.2 CRPropa

CRPropa is a publicly available tool for simulations of cosmic ray transport and their secondaries. The framework is based on a modular architecture and provides various interaction, observer, deflection and boundary modules as presented in Fig. 1.5. In each simulation, the modules can be chosen individually as needed for the specific application. In the following paragraphs, the different modules and their properties are summarized.

1.2.1 Source

A source in CRPropa emits particles from a position within the simulation volume. There are various injection options, including an isotropic emission from one point in space, homogeneous injection of particles inside a cylinder as well as injection along a specified direction. The particle energy either follows a power-law spectrum or has a specified value.

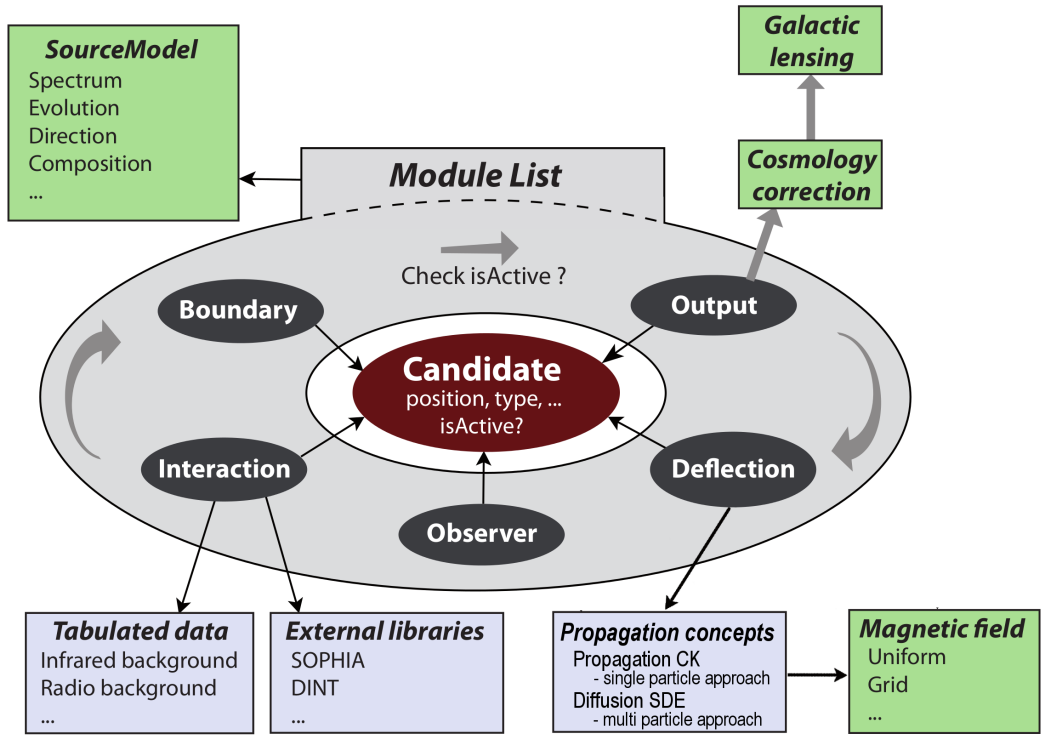

Figure 1.5: Illustration of the CRPropa 3.1 modular architecture taken from [12] based on [8]. CRPropa is based on a modular structure and therefore allows both a simulation setup with only those modules which are needed and a straightforward extension to additional modules. In every simulation step, each included module is activated as long as the candidate is still active, as indicated by the *isActive* flag.

1.2.2 Propagation

Currently, there exist two separate modules for the description of low-energy particles and high-energy particles. While the numerical solution of the equation of motion is useful for high-energy particles as implemented in the PropagationCK, this approach is not feasible for low-energy particles due to time-consuming calculations. Low-energy particles are usually simulated by solving the transport equation within the DiffusionSDE module, as it is assumed that their dominant contribution comes from below the knee.

1.2.3 Interactions

Hadronic interactions included in CRPropa are hadron-photon interactions in particular with the cosmic microwave background and the cosmic infrared background [8]. Processes included are pion production, Bethe-Heitler pair production, photo-disintegration and nuclear decay [8].

1.2.4 Magnetic Field

CRPropa provides a range of different options to include magnetic fields in the simulation [60]. Those fields use mainly discrete storage of the magnetic field vectors on a symmetric grid structure in the Cartesian coordinate system. Besides the possibility to include one of the established models, for example the JF12 magnetic field based on [61], a custom magnetic field consisting of a background field as well as a turbulent field can be used. An example of a trajectory in such a custom magnetic field without further interaction channels is given in Fig. 1.6.

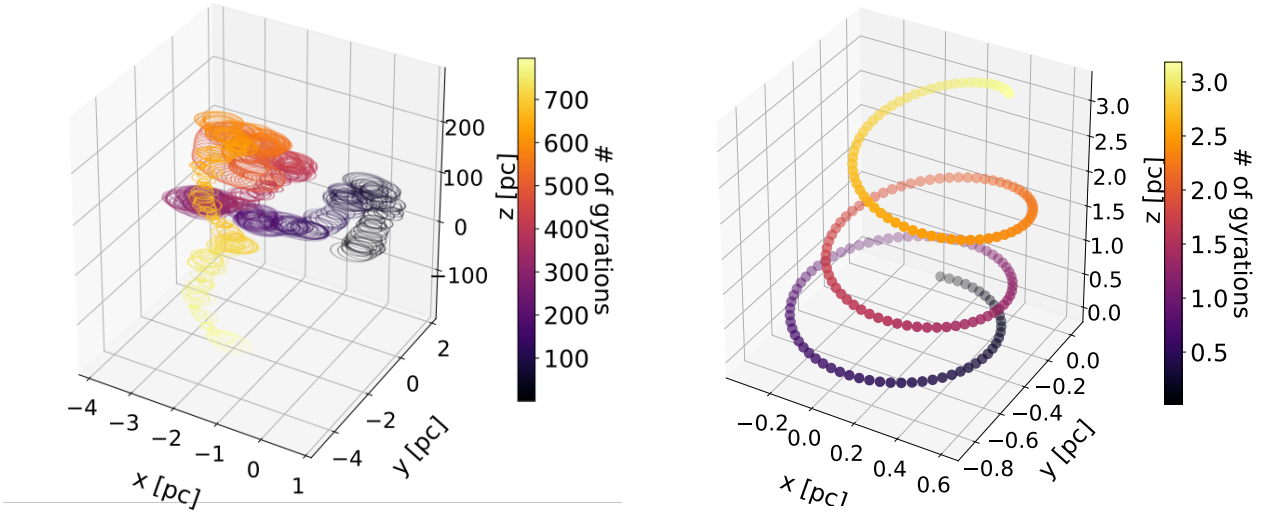

Figure 1.6: Example of a trajectory of a particle in a turbulent plus guide magnetic field, simulated with CRPropa using the following parameters: $N_{\text{grid}} = 801^3$; spacing $= 0.014\,\text{pc}$; $l_{\text{low}} = 1\,\text{pc}$; $l_{\text{high}} = 4\,\text{pc}$; $b = 10^{-7}$ Gauss; $B = 10^{-6}$ Gauss (aligned in the z-direction); E $= 400$ TeV. The pictures correspond to two different transport effects on complementary scales, illustrating the macroscopic versus the microscopic view. *Left panel*: Over the $50 \cdot 10^5$ positions by the particle in the magnetic field, its path is dominated on the large scale by scattering off the turbulent magnetic field. *Right panel*: Over the first 200 positions, the particle manages to finish only three gyrations. The turbulent magnetic field barely influences the trajectory.

1.2.5 Observer

This module generates the output of the simulation. The amount of information that will be exported during the simulation can be specified by the user. One may set particles to be detected once they cross a surface or enter a sphere; CRPropa also provides the functionality of tracking the complete trajectory of the particle. The so-called *ObserverTimeEvolution* detects all candidates at sparse, regular time intervals such that the output size is decreased, which is important for either long trajectories or many particles within one simulation.

1.3 Thesis Overview

After discussing the whole life span of cosmic rays as well as CRPropa, a software dedicated for simulating their transport, the second Chapter examines the theoretical description of the diffusion coefficient and its dependencies in the limit of weak turbulent magnetic fields. One of the major topics to be investigated in this thesis is the reduction of numerical artifacts for the calculation of the diffusion coefficient. Chapter 3 provides an important step towards investigating physical diffusion coefficient dependencies by addressing the numerical implementation as well as convergence testing. An especially challenging problem arises in the low-energy domain due to missing resonant interaction possibilities of the particles with the turbulence, resulting in mirror effects under certain conditions. This effect will also be subject of the discussion in Chapter 3. Chapter 4 tests theoretical predictions from Chapter 2 against simulated data. This thesis concludes with a study of the relation between different components of the spatial diffusion coefficient in Chapter 5.

2 | Theory

Cosmic rays undergo diffusive transport when traveling through (partially) ionized plasma along continuous magnetic field lines B subject to turbulent perturbations b. The turbulent power spectrum $G(k)$ can be specified to derive analytical approximations for the energy dependency of the diffusion coefficients as presented in this Chapter. First, three different techniques for calculating the diffusion coefficients are presented.

2.1 Diffusion Coefficient

The diffusion tensor is diagonal without drift terms and in the local frame of the magnetic field line.

2.1.1 The TGK-Formalism

This Section introduces a useful tool to calculate the diagonal entries of the diffusion coefficient tensor. The inclusion of a diffusion term in the transport equation that is based on the scattering of particles off magnetic field inhomogenities is motivated in the Taylor-Green-Kubo formalism (Taylor, 1922; [62]; Shalchi, 2011) [63]. The mean square displacement is defined as the mean square of the time-integrated particle velocity [63]

$$\left\langle (\Delta x_i)^2 \right\rangle (t) = \left\langle \left(\int_0^t \mathrm{d}\tau v_i(\tau) \right)^2 \right\rangle , \tag{2.1}$$

where Δx_i is defined as the spatial displacement along the x_i-axis at a given time with respect to its origin. The correlation between the mean of the products of two velocities at different times τ and ξ can be expressed as [63]

$$\langle v_i(\tau) v_i(\xi) \rangle = \langle v_i(\tau - \xi) v_i(0) \rangle . \tag{2.2}$$

With these correlations, the integral can be split in the following way

$$\begin{aligned} \langle (\Delta x_i)^2 \rangle (t) &= \int_0^t \mathrm{d}\tau \int_0^t \mathrm{d}\xi \langle (v_i(\tau) v_i(\xi) \rangle \\ &= \int_0^t \mathrm{d}\tau \int_0^\tau \mathrm{d}\xi \langle (v_i(\tau) v_i(\xi) \rangle + \int_0^t \mathrm{d}\tau \int_\tau^t \mathrm{d}\xi \langle v_i(\tau) v_i(\xi) \rangle \\ &= \int_0^t \mathrm{d}\tau \int_0^\tau \mathrm{d}\xi \langle (v_i(\tau - \xi) v_i(0) \rangle + \int_0^t \mathrm{d}\tau \int_\tau^t \mathrm{d}\xi \langle (v_i(\xi - \tau) v_i(0) \rangle . \end{aligned} \tag{2.3}$$

Finally transforming into new coordinates [63] in both integrals $\tau - \xi \to \xi$ and $\xi - \tau \to \xi$, respectively. The coordinate transformation implies a change of the integration bounds $0 \to \tau$ and $\tau \to 0$ in the first integral, as well as $\tau \to 0$ and $t \to t - \tau$ in the second integral, simplifying the problem. Inserting

$1 = \mathrm{d}\tau/\mathrm{d}\tau$ in combination with partial integration yields the result

$$\langle(\Delta x_i)^2\rangle(t) = 2\int_0^t \mathrm{d}\tau(t-\tau)\langle(v_i(\tau)v_i(0)\rangle. \tag{2.4}$$

It can be shown that the diagonal entries of the diffusion coefficient $\kappa_{ii}(t)$ can be expressed as [63]

$$\kappa_{ii} = \frac{1}{2}\frac{\mathrm{d}}{\mathrm{d}t}\langle(\Delta x_i)^2\rangle = \langle(v_i(t)\Delta x_i)\rangle. \tag{2.5}$$

The latter expression can be used for the numerical calculation of the diagonal elements of the diffusion tensor and will be denoted as TGK-method. The expression $\frac{1}{2}\frac{\mathrm{d}}{\mathrm{d}t}\langle(\Delta x_i)^2\rangle$ corresponds to $\frac{\langle(\Delta x_i)^2\rangle}{2t}$ in the limit of large times, as will be derived below. The latter method will be denoted as the second moment method.

2.1.2 Diffusion Equation based on Fokker-Planck-Equation

As a first approximation, the quasi-linear theory (QLT) derived by Jokipii [64] is presented. The mechanism is based on the Vlasov equation in the realm of the *test particle approach*

$$\frac{\partial f_a}{\partial t} + \mathbf{v}\frac{\partial f_a}{\partial \mathbf{x}} + \dot{\mathbf{p}}\frac{\partial f_a}{\partial \mathbf{p}} = S_a(\mathbf{x},\mathbf{p},t). \tag{2.6}$$

The test particle distribution function f is constrained by angular scattering [65, 66]

$$\frac{\partial f}{\partial t} + v_i\mu\frac{\partial f}{\partial x_i} = \frac{\partial}{\partial \mu}\left(D_{\mu\mu}\frac{\partial f}{\partial \mu}\right), \tag{2.7}$$

where μ is the cosine of the pitch angle and $D_{\mu\mu}$ is the diffusion coefficient, which is defined as [67]

$$D_{\mu\mu} = \lim_{t\to\infty}\int_0^t \mathrm{d}t'\langle\dot{\mu}(t')\dot{\mu}(0)\rangle \overset{\text{iso.}b}{=} (1-\mu^2)D. \tag{2.8}$$

D is the scattering rate and an isotropic turbulent magnetic field is assumed in the last step [67]. The calculation of the pitch angle diffusion coefficient with numerical methods is in disagreement with the results within QLT [68]. The limitation of possible pitch angle scattering around $\mu \sim 0$ is the reason for this problem because particles cannot interact resonantly with the fluctuations b anymore [69]. This leads toward a $D_{\mu\mu} \propto t^{-1}$ behavior of the running pitch angle diffusion coefficients $D_{\mu\mu}$ for long times instead of the predicted plateau. After motivating the transformation from pitch angle diffusion toward spatial diffusion, ensuring a constant diffusion coefficient κ_{ii} in the limit of large t, the derivation starts by applying the operator $\int_{-1}^{1}\mathrm{d}\mu$ on both sides of the Fokker-Planck equation

$$\int_{-1}^{1}\mathrm{d}\mu\ \frac{\partial f}{\partial t} + \int_{-1}^{1}\mathrm{d}\mu\ v_i\mu\frac{\partial f}{\partial x_i} = \int_{-1}^{1}\mathrm{d}\mu\ \frac{\partial}{\partial \mu}\left(D_{\mu\mu}\frac{\partial f}{\partial \mu}\right). \tag{2.9}$$

Under the use of the definitions of the particle density (averaged over pitch angles)

$$M(x_i,t) = \frac{1}{2}\int_{-1}^{1}\mathrm{d}\mu\ f(\mu,x_i,t) \tag{2.10}$$

and the current density

$$j(x_i,t) = \frac{v}{2}\int_{-1}^{1}\mathrm{d}\mu\ \mu f(\mu,x_i,t), \tag{2.11}$$

the continuity equation

$$\frac{\partial M(x_i,t)}{\partial t} = -\frac{\partial j(x_i,t)}{\partial x_i} \tag{2.12}$$

can be derived. By applying the operator $\int_{-1}^{\mu'} \mathrm{d}\mu$ on the Fokker-Planck equation and multiplying with $(1-\mu'^2)/D_{\mu'\mu'}$ afterwards, one finds

$$\frac{1-\mu'^2}{D_{\mu'\mu'}}\left(\frac{\partial}{\partial t}\int_{-1}^{\mu'} \mathrm{d}\mu f(\mu,x_i,t) + v_i\frac{\partial}{\partial x_i}\int_{-1}^{\mu'} \mathrm{d}\mu\ \mu f(\mu,x_i,t)\right) = (1-\mu'^2)\frac{\partial f(\mu',x_i,t)}{\partial \mu'}. \tag{2.13}$$

Applying the operator $\int_{-1}^{1} \mathrm{d}\mu'$ on both sides and afterwards renaming μ' to μ results in

$$\int_{-1}^{1} \mathrm{d}\mu\ \frac{1-\mu^2}{D_{\mu\mu}}\left(\frac{\partial}{\partial t}\int_{-1}^{\mu} \mathrm{d}\mu f(\mu,x_i,t) + v_i\frac{\partial}{\partial x_i}\int_{-1}^{\mu} \mathrm{d}\mu\ \mu f(\mu,x_i,t)\right) = \int_{-1}^{1} \mathrm{d}\mu\ (1-\mu^2)\frac{\partial f(\mu,x_i,t)}{\partial \mu}, \tag{2.14}$$

$$\overset{\text{p.I.}}{=} -\int_{-1}^{1} \mathrm{d}\mu\ \frac{\partial(1-\mu^2)}{\partial \mu} f(\mu,x_i,t) \overset{\text{Equ. (2.11)}}{=} \frac{v_i}{4} j(x_i,t). \tag{2.15}$$

Taking the limit of large t in which $f(\mu,x_i,t)$ is replaced by $M(x_i,t)$ yields

$$j(x_i,t) = \frac{v_i}{4}\frac{\partial M(x_i,t)}{\partial t}\int_{-1}^{+1} \mathrm{d}\mu \frac{(1-\mu^2)(1+\mu)}{D_{\mu\mu}} - \frac{v_i^2}{8}\frac{\partial M(x_i,t)}{\partial x_i}\int_{-1}^{+1} \mathrm{d}\mu \frac{(1-\mu^2)^2}{D_{\mu\mu}}. \tag{2.16}$$

According to Equ. (2.12), $\partial M(x_i,t)/\partial t$ can be replaced with $-\partial j(x_i,t)/\partial x_i$. Using the fact that $\lim\limits_{t\to\infty} j(x_i,t) = 0$ results in

$$j(x_i,t) = -\frac{v_i^2}{8}\int_{-1}^{+1} \mathrm{d}\mu \frac{(1-\mu^2)^2}{D_{\mu\mu}}\frac{\partial M(x_i,t)}{\partial x_i^2}. \tag{2.17}$$

To complete the switch from the description of the pitch angle diffusion toward the spatial diffusion, the following definition is used [63]

$$\kappa_{ii} = \frac{v_i^2}{8}\int_{-1}^{+1} \mathrm{d}\mu \frac{(1-\mu^2)^2}{D_{\mu\mu}}, \tag{2.18}$$

such that the general expression of the continuity equation reads

$$\frac{\partial M(x_i,t)}{\partial t} = \kappa_{ii}\frac{\partial^2 M(x_i,t)}{\partial x_i^2}. \tag{2.19}$$

A point-like source as the initial condition of the problem is represented by a *Dirac Delta* distribution at $t = 0$

$$M(x_i',0) = \delta(x_i'). \tag{2.20}$$

As derived in Appendix C and shown in Appendix H, the distribution at sufficient large times yields

$$M(x_i,t) = \frac{1}{2\sqrt{\pi\kappa_{ii}t}}\exp\left(-\frac{x_i^2}{4\kappa_{ii}t}\right). \tag{2.21}$$

Diffusive transport from a point source leads to a Gaussian distribution of the pitch angle averaged particle density in all three dimensions. By reasoning in the same way as in the previous paragraph, the diffusion coefficient is found by calculating the second moment

$$\langle(\Delta x_i)^2\rangle = \int_{-\infty}^{+\infty} \mathrm{d}x_i x_i^2 f(x_i, t) = 2t\kappa_{ii}. \tag{2.22}$$

The 3D case is investigated in Appendix D and shows that each component can be treated individually.

Limit of Long Times The diffusive process is based on scattering off turbulent fluctuations. This mechanism necessitates for a sufficiently long duration of the simulation in order to enter the diffusive regime, typically requiring a number of gyrations about the static background field. Reshaping Equ. (2.22) provides an expression for calculating the diffusion coefficient numerically in the limit of long times

$$\kappa_{ii} = \lim_{t\to\infty} \frac{\langle(\Delta x_i)^2\rangle}{2t}. \tag{2.23}$$

This is called the second moment method and will be used, besides the TGK-method, to calculate the running diffusion coefficient. This running diffusion coefficient will be presented as a function of the time or the distance measured in gyrations for a constant particle speed (see Fig. 3.10 for an example). After a certain time, which will be discussed in Section 3.3.1, the running diffusion coefficient converges to its final value. Consequently, the converged value is the final diffusion coefficient.

2.1.3 Momentum Diffusion Coefficient

In Appendix E, the momentum diffusion coefficient D_v is introduced and the relation with the spatial diffusion coefficient $\kappa_\parallel$ is derived [65, 70, 71]

$$\kappa = \frac{v^4}{6D_v}. \tag{2.24}$$

This relation is especially useful because the calculation of D_v simplifies significantly for high-energy particles, constituting an elegant way of deriving $\kappa_\parallel$ in the limit of $R_\mathrm{g} \gg l_\mathrm{corr}$. Here, the correlation length l_corr is defined as the characteristic length over which fluctuations in the interstellar magnetic field are correlated [72].

TGK-Formalism: Extension of the Spatial Diffusion Coefficient An intuitive derivation of the momentum diffusion coefficient is carried out in the TGK-Formalism. The idea is similar to the description that can be found in Chapter 2.1.1. As a consequence, Equ. (2.4) can be extended easily. The momentum diffusion coefficient is expressed in terms of the velocity

$$\langle(\Delta v_i)^2\rangle(t) = 2\int_0^t \mathrm{d}\tau\ (t-\tau)\left\langle \frac{\mathrm{d}v_i}{\mathrm{d}\tau}(\tau)\frac{\mathrm{d}v_i}{\mathrm{d}\tau}(0)\right\rangle, \tag{2.25}$$

This equation is obtained by exchanging the spatial displacement with the momentum. The momentum diffusion coefficient is defined similar to the spatial diffusion coefficient

$$D_{ij}(t) = \lim_{t\to\infty} \frac{\langle(\Delta v_i)^2\rangle}{2t}. \tag{2.26}$$

The general form of the momentum diffusion coefficient is therefore

$$D_{ij}(t) = \lim_{t\to\infty} \int_0^t \mathrm{d}\tau \left\langle \frac{\mathrm{d}v_i}{\mathrm{d}\tau}(\tau) \frac{\mathrm{d}v_i}{\mathrm{d}\tau}(0) \right\rangle. \tag{2.27}$$

The change of the momentum in a certain direction is caused by the interaction of the particles with the plasma waves and the background field. Cosmic rays undergo a diffusive transport when traveling through (partially) ionized plasma along homogeneous magnetic field lines B with a perturbation of a turbulent magnetic field b. The fluctuations of b due to plasma waves enable scattering processes of the cosmic rays and therefore lead to a random walk in momentum space.

2.2 Diffusive-Energy Regime

The gyroresonance condition relates the range of plasma waves l with which a particle with a certain gyroradius R_g resonantly interacts

$$|\mu| = \frac{l}{2\pi R_\mathrm{g}}, \tag{2.28}$$

where $|\mu|$ is defined as the absolute value of the cosine of the pitch angle Θ_0. The pitch angle Θ_0 is defined as the angle between the particle direction and the magnetic field. The diffusive regime is defined as the energy range of particles, where particles resonantly interact with the fluctuations for $-1 \leq \mu \leq 1$. Decreasing the energy of the particles for a given l_low, increases the range around $|\mu| = 0$, where no resonant interactions are possible. Finally, no resonant interactions are possible over the complete range of $|\mu|$ for

$$R_\mathrm{g} \leq l_\mathrm{low}/(2\pi). \tag{2.29}$$

In the diffusive-energy regime of particles, $\kappa_\parallel$ is inversely proportional to the scattering rate ν

$$\kappa_\parallel \propto \frac{v^2}{\nu}, \tag{2.30}$$

which can be expressed as $\nu \propto \omega G(k)/B^2$ [70]. The gyroresonance condition $k = \omega/(\mu v)$ can be used to derive ν as a function of the energy

$$\nu \propto v k_\mathrm{low} \left(\frac{k}{k_\mathrm{low}}\right)^{-\alpha+2} \frac{b^2}{B^2}. \tag{2.31}$$

This can be inserted back into Equ. (2.30)

$$\kappa_\parallel \propto \frac{v}{k_\mathrm{low}} \left(\frac{k}{k_\mathrm{low}}\right)^{\alpha-2} \frac{B^2}{b^2} \propto v l_\mathrm{corr} \left(\frac{R_\mathrm{g}}{l_\mathrm{corr}}\right)^{2-\alpha} \frac{B^2}{b^2}, \tag{2.32}$$

where the correlation length is used according to Equ. (3.7) so that $k_\mathrm{low} = 2\pi/l_\mathrm{high} = 2\pi/(5l_\mathrm{corr})$.

2.3 Above the Diffusive-Energy Regime

When studying particles with high energies obeying

$$|\mu_\mathrm{high}| = \frac{l_\mathrm{high}}{2\pi R_\mathrm{g}} \lesssim 1, \tag{2.33}$$

they cannot interact with plasma waves in a resonant way over the whole range of possible pitch angles. Here, l_{high} is the largest present plasma wavelength and $|\mu_{\mathrm{high}}|$ the upper boundary of the interaction range. It is then reasonable to neglect the resonant scattering of the charged particles at the turbulent magnetic field b. The change of momentum projected onto a certain direction is, in general, complicated. The change of momentum is described by the relativistic Lorentz force

$$\frac{\mathrm{d}\mathbf{v}}{\mathrm{d}t} = \frac{q}{m\gamma c}(\mathbf{v} \times (\mathbf{b} + \mathbf{B})), \tag{2.34}$$

with the Lorentz factor γ, mass m and charge q of the particle. For the parallel diffusion coefficient only the change of the parallel velocity has to be considered

$$\begin{aligned}
\frac{\mathrm{d}\mathbf{v}_\parallel}{\mathrm{d}t} &= \frac{q}{m\gamma c}(\mathbf{v}_\perp \times \mathbf{b}), && (2.35)\\
&= \frac{q}{m\gamma c}\mathbf{v}_\perp \times (\nabla \times \mathbf{A}_1), && (2.36)\\
&= \frac{q}{m\gamma c}\nabla(\mathbf{v}_\perp \cdot \mathbf{A}_1) - (\mathbf{v}_\perp \cdot \nabla)\mathbf{A}_1, \overset{\mathbf{E}=0}{=} \frac{q}{m\gamma c}\nabla(\mathbf{v}_\perp \cdot \mathbf{A}_1), && (2.37)
\end{aligned}$$

where it is used that $\mathbf{B} = (0, 0, B_3)$ and a vanishing electric field $\mathbf{E} = 0$, which is motivated in Section 3.1.1. A_1 is the magnetic vector potential of b. Inserting Equ. (2.37) in Equ. (2.27) yields

$$D_\parallel(v) = D_{33}(v) = \lim_{t\to\infty}\left(\frac{q}{m\gamma c}\right)^2 \int_0^t \mathrm{d}\tau \ \langle(\nabla(\mathbf{v}_\perp(\theta)\cdot\mathbf{A}_1(0)))(\nabla(\mathbf{v}_\perp(\theta)\cdot\mathbf{A}_1[\mathbf{x}=\mathbf{X}(\tau)+R_{\mathrm{g}}\cdot\mathbf{s}]))\rangle\,. \tag{2.38}$$

For small ratios of b/B (discussion below and in Fig. F.1 and Fig. F.3), particles follow a helical trajectory caused by the background magnetic field in the x_3-direction. This motion can be separated into the motion of the gyrocenter with a position $\mathbf{X}$ and the circular motion along the trajectory $\mathbf{s}$

$$\mathbf{s} = \begin{pmatrix} \sin(\theta) \\ -\cos(\theta) \\ 0 \end{pmatrix} \ ; \ \mathbf{X} = \begin{pmatrix} 0 \\ 0 \\ v_\parallel(0)\tau \end{pmatrix}, \tag{2.39}$$

which orders out drift velocities. The velocity $\mathbf{v}$ of a gyrating particle can therefore be parameterized together with its positions as

$$\mathbf{v} = \begin{pmatrix} v_\perp\cos(\theta) \\ v_\perp\sin(\theta) \\ v_\parallel\tau \end{pmatrix} = v_\parallel\mathbf{e}_3 + v_\perp\mathbf{c}(\theta) \ ; \ \mathbf{c} = \begin{pmatrix} \cos(\theta) \\ \sin(\theta) \end{pmatrix}. \tag{2.40}$$

The calculation of the diffusion coefficients is based on long trajectory lengths of the particles. Consequently, Equ. (2.38) yields

$$D_\parallel(v) = \lim_{t\to\infty}\left(\frac{q}{m\gamma c}\right)^2 \int_0^t \mathrm{d}\tau \ \langle\nabla(\mathbf{v}_\perp(0)\cdot\mathbf{A}_1(0))\rangle\,\langle\nabla(\mathbf{v}_\perp(\tau)\cdot\mathbf{A}_1[\mathbf{x}=\mathbf{X}(\tau)+R_{\mathrm{g}}\cdot\mathbf{s}])\rangle\,. \tag{2.41}$$

2.3.1 Intermediate-Energy Regime

The intermediate-energy regime is defined by particle energies that correspond to gyroradii that are on the same order or slightly larger than l_{corr}. As motivated above, resonant interactions of the particles at the fluctuations are not possible. It is assumed that the turbulent magnetic field vectors are correlated along each particle trajectory. It is worth noting that even if the particles do not scatter

resonantly with the plasma waves, they can get deflected by those same plasma waves.
Below, the gyroaveraging of the relevant term in Equ. (2.41) is presented based on the derivations presented in [73]

$$\begin{aligned}\langle\nabla(\mathbf{v}_\perp(\tau)\cdot\mathbf{A}_1[\mathbf{x}=\mathbf{X}(\tau)+R_\mathrm{g}\cdot\mathbf{s}])\rangle &= \frac{1}{2\pi}\int_0^{2\pi}\mathrm{d}\theta\ \nabla(\mathbf{A}_1[\mathbf{x}=\mathbf{X}(\tau)+R_\mathrm{g}\cdot\mathbf{s}]\cdot\mathbf{v}_\perp(\tau))\\ &= -v_\perp\int\frac{\mathrm{d}^3k}{(2\pi)^3}\ i\mathbf{k}\mathbf{A}_1(\mathbf{k})\mathrm{e}^{i\mathbf{k}\mathbf{X}}\frac{1}{2\pi}\int_0^{2\pi}\mathrm{d}\theta\ \mathrm{e}^{i\mathbf{k}\mathbf{r}}\mathbf{c}(\theta)\\ &= v_\perp\int\frac{\mathrm{d}^3k}{(2\pi)^3}\ (k_2\mathbf{e}_1-k_1\mathbf{e}_2)\frac{\mathbf{k}}{k_\perp}J_1\mathbf{A}_1(\mathbf{k})\mathrm{e}^{i\mathbf{k}\mathbf{X}}\\ &= -v_\perp\int\frac{\mathrm{d}^3k}{(2\pi)^3}\ (ik_2A_{11}(\mathbf{k})-ik_1A_{12}(\mathbf{k}))\frac{i\mathbf{k}}{k_\perp}J_1(\mathbf{k})\mathrm{e}^{i\mathbf{k}\mathbf{X}}\\ &\overset{\text{p.I.}}{=} v_\perp\frac{I_1(iR_\mathrm{g}\nabla_\perp)}{2}b_\parallel,\end{aligned}\tag{2.42}$$

where $J_1(R_\mathrm{g}k_\perp)$ is the Bessel function and the function $I_1(iR_\mathrm{g}\nabla_\perp)$ is defined as [73]

$$I_1(x)=\sum_{\nu=0}^{\infty}\frac{\left(-\frac{1}{4}x^2\right)^\nu}{\nu!(\nu+1)!}\ ,\quad J_1(x)=\left(\frac{x}{2}\right)^2\sum_{\nu=0}^{\infty}\frac{\left(-\frac{1}{4}x^2\right)^\nu}{\nu!(\nu+1)!}.\tag{2.43}$$

Equ. (2.41) yields

$$D_\parallel(v)=\left(\frac{v_\perp qI_1}{2m\gamma c}\right)^2\lim_{t\to\infty}\int_0^t\mathrm{d}\tau\ b(0)b(\mathbf{x}=\mathbf{X}(\tau))=\left(\frac{v_\perp qI_1}{2m\gamma c}\right)^2\frac{b^2l_\mathrm{corr}}{c}.\tag{2.44}$$

To compare the spatial parallel diffusion coefficient with simulation results based on CRPropa, the particle velocity will be set to the speed of light c, as it is done in CRPropa. The relativistic particle energy E is given by

$$E=\gamma mc^2\tag{2.45}$$

and the gyroradius is proportional to E

$$R_\mathrm{g}=\frac{E}{B_{\mathrm{tot},3}cq},\tag{2.46}$$

where $B_{\mathrm{tot},3}$ is the magnitude of the magnetic field along the x_3-axis, which averages to

$$B_{\mathrm{tot},3}=\frac{1}{2\pi}\int_0^{2\pi}\mathrm{d}\phi\ \frac{1}{\pi}\int_0^{\pi}\mathrm{d}\theta\ |B+b\cdot\cos(\phi)\cdot\cos(\theta)|.\tag{2.47}$$

The result of this integration is presented in Appendix F for the 3D case numerically as well as for the 2D case both analytically and numerically. The calculations are presented as functions of the ratio b/B. The analytical solution for the 2D case (without θ) yields

$$B_{\mathrm{tot},3}=\begin{cases}B & \text{if } b\le B\\ \frac{1}{2\pi}[B\,(4\cos^{-1}(-B/b)-2\pi)+4\,b\,\sin(\cos^{-1}(-B/b))] & \text{if } b\ge B\end{cases}.\tag{2.48}$$

For the 3D case it yields $B_{\mathrm{tot},3}=B$ for $b\le B$. Using a fit to the numerically evaluated results for the 3D case in the limit $b\ll B$, see Fig. F.1, one may write the total magnetic field as $B_{\mathrm{tot},3}\propto b$. Figure F.3 in Appendix F presents the ratio of the magnetic field components as functions of the ratio b/B, which is based on the numerically determined projections of B_tot in the parallel and perpendicular

directions of the used magnetic field. As long as $B_\parallel$ is dominant with respect to the perpendicular magnetic field, the classification into the parallel and perpendicular diffusion coefficient is reasonable. These findings suggest that the classification is reasonable for values up to ratios b/B above 1.
Using Equ. (2.44), Equ. (2.45), Equ. (2.46) and Equ. (F.4) in Equ. (2.24) yields for $b \leq B$

$$\kappa_\parallel = \frac{2}{3}\left(\frac{m\gamma c^2}{qI_1}\right)^2 \frac{c}{l_{\mathrm{corr}} b^2} = \frac{2cl_{\mathrm{corr}}}{3I_1^2}\left(\frac{R_{\mathrm{g}}}{l_{\mathrm{corr}}}\right)^2\left(\frac{B}{b}\right)^2. \tag{2.49}$$

Determining the ratio of $R_{\mathrm{g}}/l_{\mathrm{corr}}$ at which the abovementioned assumptions of this regime break down is out of the scope of this thesis. This ratio is denoted with χ in the following. Further research with more focus on determining the transition between the intermediate and the high-energy regime is planned.

2.3.2 High-Energy Regime

In the limit $R_{\mathrm{g}} \gg l_{\mathrm{corr}}$, it is assumed that the turbulent magnetic field vectors are deccorrelated between two following particle positions along the particle trajectory. It is now possible to put the magnetic field in front of the integral as shown below.
Equ. (2.27) yields together with Equ. (2.35) and the Levi-Civita symbol $\epsilon_{\nu\gamma\eta}$

$$\begin{aligned} D_{33}(v) &= \left(\frac{q}{m\gamma c}\right)^2 \epsilon_{3\alpha\beta}\epsilon_{3\gamma\eta}\int_0^t \mathrm{d}\tau\ \langle v_\alpha(0)v_\gamma(\tau)b_\beta(0)b_\eta[\mathbf{x}(\tau)]\rangle\,, \\ &= \left(\frac{q}{m\gamma c}\right)^2 \epsilon_{3\alpha\beta}\epsilon_{3\gamma\eta}\int_0^t \mathrm{d}\tau\ \frac{1}{2\pi}\int_0^{2\pi}\mathrm{d}\theta\ v_\alpha(0)v_\gamma(\tau)b_\beta(0)b_\eta[\mathbf{X}(\tau)+R_{\mathrm{g}}\cdot\mathbf{s}], \end{aligned} \tag{2.50}$$

The turbulent magnetic field $\mathbf{b}$ at an arbitrary position points into a random direction, so that b_i is also arbitrary: $-b < b_i < b$. The importance is, however, that b_i scales proportionally with b so that it yields $b_i \propto b$. Together with the cyclic definition of the Levi-Civita symbol, Equ. (2.50) yields

$$D_{33}(v) = \left(\frac{bq}{m\gamma c}\right)^2 \int_0^t \frac{\mathrm{d}\tau}{2\pi}\int_0^{2\pi}\mathrm{d}\theta\ (v_1(0,\theta)v_1(\tau,\theta)+v_2(0,\theta)v_2(\tau,\theta)-v_2(0,\theta)v_1(\tau,\theta)-v_1(0,\theta)v_2(\tau,\theta)). \tag{2.51}$$

Using the definition of Equ. (2.40) for the parameterized particle velocity results in

$$\begin{aligned} D_{33}(v) &= \left(\frac{qbv_\perp}{m\gamma c}\right)^2 \int_0^t \mathrm{d}\tau\ \left(\cos\left(\frac{v_\perp}{R_g}\tau\right)-\sin\left(\frac{v_\perp}{R_g}\tau\right)\right)\ \frac{1}{2\pi}\int_0^{2\pi}\mathrm{d}\theta\ (\cos^2\theta\ +\sin^2\theta), \\ &= \left(\frac{qbv_\perp}{m\gamma c}\right)^2 \int_0^t \mathrm{d}\tau\ \left(\cos\left(\frac{v_\perp}{R_g}\tau\right)-\sin\left(\frac{v_\perp}{R_g}\tau\right)\right). \end{aligned} \tag{2.52}$$

Substituting $\hat{\tau} = \tau v_\perp/R_{\mathrm{g}}$ together with $\mathrm{d}\tau = R_{\mathrm{g}}/v_\perp\ \mathrm{d}\hat{\tau}$ results in

$$D_{33}(v) \propto \left(\frac{qbv_\perp}{m\gamma c}\right)^2 \frac{R_{\mathrm{g}}}{v_\perp}\int_0^{t'}\mathrm{d}\hat{\tau}\ (\cos\hat{\tau}-\sin\hat{\tau}). \tag{2.53}$$

With this parallel momentum diffusion coefficient, it is possible to derive the parallel spatial diffusion coefficient based on Equ. (2.24), Equ. (2.44), Equ. (2.45), Equ. (2.46) and Equ. (F.4)

$$\kappa_\parallel \propto \left(\frac{m\gamma c v^2}{qbv_\perp}\right)^2 \frac{v_\perp}{R_{\mathrm{g}}} \propto \frac{m^2\gamma^2c^2v^4}{b^2v_\perp R_{\mathrm{g}}} \propto \frac{B_{tot,3}}{b^2}\frac{E}{q} \propto \left(\frac{B_{tot,3}}{b}\right)^2 R_{\mathrm{g}}c \overset{b\leqq B}{=} \left(\frac{B}{b}\right)^2 R_{\mathrm{g}}c. \tag{2.54}$$

3 | Calculation of Diffusion Coefficients and its Challenges

Diffusion has long been described by a quasi-linear theory approach in the limit $b \ll B$ [64, 74]. However, in many physical applications b is of similar order of magnitude as B so that these theoretical descriptions are not applicable. Several studies have investigated the diffusion coefficient tensor in numerical simulations in pure turbulence ($B = 0$) [17, 71, 75–80] or with an additional regular component B for varying ratios of b/B [11, 14–17, 52, 71, 75, 77–80]. The main challenge in numerical simulations arises from the necessity for a large range of particle energies to investigate the diffusion coefficient's energy dependency in different regimes. It is difficult to preserve the accuracy of the simulated diffusion coefficients over the whole range of particle energies, given that the particle energy determines the range of plasma wavelengths with which the particles can resonantly interact, i.e. $l = |\mu| 2\pi R_\mathrm{g}$. As a consequence, the range of wavelengths l of the fluctuations b has to extend over a large range of scales, from the dissipation scale l_low to the outer scale l_high. In order to cope with this large range of scales, simulations employ a synthetic random magnetic field, either composed of a superposition of static plane waves [11, 17] or specified on a discrete mesh [6, 14, 52].
Table 3.1 reviews different parameters used in previous studies focusing on the range of different ratios b/B and $R_\mathrm{g}/l_\mathrm{corr}$. As will be demonstrated in detail throughout this Chapter, the dependencies of the simulation parameters on the diffusion coefficient are multilayered and highly entangled. Subtle details of the magnetic field structure, such as the magnetic modes density together with the range of wave numbers involved, influence the diffusion coefficient. Table 3.1 lists the range of wave numbers together with the magnetic modes density for the different studies.
Previous work has focused on extending the energy range toward lower energies without addressing the question of how far this approach can be pursued without initiating numerical artifacts due to missing resonant interactions. The discussion about the diffusive regime in Chapter 2 revealed the range of particle energies for which diffusion is expected. Around $R_\mathrm{g}/l_\mathrm{corr} \lesssim 5/(2\pi)$ particles can scatter over the whole range of μ. Decreasing the energy of the particles increases the gap around $|\mu| \sim 0$ where resonant interactions are not possible as described in Equ. (2.29). Finally, no interactions are possible at $R_\mathrm{g} = l_\mathrm{low}/(2\pi)$. This lower border is consequently the start of the transition into the diffusive regime while the upper border at $R_\mathrm{g}/l_\mathrm{corr} = 5/(2\pi)$ is really the upper border of the diffusive regime. The details will be discussed in Section 3.3.2.
The different power-law indices γ of the energy dependency of the diffusion coefficient $\kappa_\parallel \propto E^\gamma$ have to account for all data points until the upper border. $\gamma_\mathrm{corrected}$ presents two fits in table 3.1. The first fit takes all simulated data within the lower and upper border into account, while the second fit is only based on the two closest values at the upper border in Equ. (2.33) around $R_\mathrm{g}/l_\mathrm{corr} \lesssim 5/(2\pi)$. The latter fit reduces the numerical artifacts introduced by missing interactions around $\mu = 0$, while increasing the uncertainties. In the column γ, the slopes are listed as stated in each paper. The input parameters of simulations in this thesis are defined in Section 3.1 are shown in the gray hexagons in Fig. 3.1.

Table 3.1: Review of the different parameters used in previous studies, which are cited in the first column. The different power-law indices γ from the energy dependency of the diffusion coefficient $\kappa_{\parallel} \propto E^{\gamma}$ are presented for different ratios of b/B as stated in each paper for Kolmogorov fluctuations except [51]$^{|}$ and use superposition of plane waves for generating the fluctuations except of those marked with **. All models are based on isotropic turbulence except [16]*. The first value of $\gamma_{\text{corrected}}$ presents the fit over all data points in the diffusive regime between the borders defined in Equ. (2.29) calculated in the seventh column and Equ. (2.33), which always yields $R_{\text{g}}/l_{\text{corr}} = 5/(2\pi)$. The second value is based on the fit of the two closest values at the upper border in Equ. (2.33) around $R_{\text{g}}/l_{\text{corr}} \lesssim 5/(2\pi)$. For details see Appendix M.

	b/B	B_{g} [μG]	l_{high} [pc]	$k_{\text{high}}/k_{\text{low}}$	$N_{\text{m}}/\text{d}k$	$R_{\text{g}}/l_{\text{corr}}{}^{\ddagger}$	$R_{\text{g}}/l_{\text{corr}}$	γ	$\gamma_{\text{corrected}}$
[52]	∞	100	100	256^{**}	8179	0.003	$0.005 - 5.000^{\ddagger}$	–	$0.47 - 0.83$
[52]	2	2.236	100	256^{**}	8179	0.003	$0.024 - 2.417^{\ddagger}$	1/3	$0.55 - 0.92$
[52]	1	1.414	100	256^{**}	8179	0.003	$0.038 - 3.822^{\ddagger}$	1/3	$0.49 - 0.89$
[52]	0.5	1.118	100	256^{**}	8179	0.003	$0.048 - 4.834^{\ddagger}$	1/3	$0.44 - 0.50$
[17]	∞	1	100	128^{**}	16358	0.006	$0.054 - 5.405$	1/3	$0.81 - 1.15$
[17]	4	1	100	128^{**}	16358	0.006	$0.054 - 5.405$	1/3	$0.84 - 1.14$
[17]	2	1	100	128^{**}	16358	0.006	$0.054 - 5.405$	1/3	$0.71 - 1.09$
[17]	1	1	100	128^{**}	16358	0.006	$0.054 - 5.405$	1/3	$0.56 - 0.82$
[17]	0.5	1	100	128^{**}	16358	0.006	$0.054 - 5.405$	1/3	$0.51 - 0.82$
[17]	0.1	1	100	128^{**}	16358	0.006	$0.054 - 5.405$	1/3	$0.49 - 0.78$
[15]	∞	–	–	128^{**}	16384	0.001	$7.96 \cdot 10^{-5} - 5$	1	$0.62 - 1.72$
[15]	9.95	–	–	128^{**}	16384	0.049	$0.0062 - 5$	1/3	$1.09 - 1.92$
[15]	0.92	–	–	128^{**}	16384	0.049	$0.0062 - 5$	1/3	$0.61 - 0.60$
[15]	0.52	–	–	128^{**}	16384	0.049	$0.0062 - 5$	1/3	$0.53 - 0.46$
[15]	0.33	–	–	128^{**}	16384	0.049	$0.0062 - 5$	1/3	$0.61 - 0.76$
[11]	∞	–	–	200^{**}	671089	$-^{\dagger}$	$0.015 - 20$	1	$0.58 - 1.17$
[11]	9.95	–	–	200^{**}	671089	$-^{\dagger}$	$0.015 - 20$	1/3	$0.72 - 1.01$
[11]	3	–	–	200^{**}	671089	$-^{\dagger}$	$0.015 - 20$	1/3	$0.59 - 0.93$
[11]	1	–	–	200^{**}	671089	$-^{\dagger}$	$0.015 - 20$	1/3	$0.42 - 0.62$
[11]	0.33	–	–	200^{**}	671089	$-^{\dagger}$	$0.015 - 20$	1/3	$0.36 - 0.63$
[16]*	5	–	–	–	–	$-^{\dagger}$	$0.001 - 1^{\ddagger\ddagger}$	0.84	$0.69 - 0.72$
[16]*	1	–	–	–	–	$-^{\dagger}$	$0.001 - 1^{\ddagger\ddagger}$	0.76	$0.60 - 0.76$
[16]*	0.6	–	–	–	–	$-^{\dagger}$	$0.001 - 1^{\ddagger\ddagger}$	0.60	$0.48 - 0.56$
[16]*	0.2	–	–	–	–	$-^{\dagger}$	$0.001 - 1^{\ddagger\ddagger}$	0.43	$0.33 - 0.40$
[51]$^{\|}$	10	10.05	100	$10^3 - 10^+$	$0.1 - 10^+$	0.0008^+	$0.005 - 0.498$	1/3	$0.44 - 1.08$
[51]$^{\|}$	7.07	7.14	100	$10^3 - 10^+$	$0.1 - 10^+$	0.0008^+	$0.007 - 0.700$	1/3	$0.58 - 1.30$
[51]$^{\|}$	5.48	5.57	100	$10^3 - 10^+$	$0.1 - 10^+$	0.0008^+	$0.009 - 0.898$	1/3	$0.43 - 0.64$
[51]$^{\|}$	3.16	3.31	100	$10^3 - 10^+$	$0.1 - 10^+$	0.0008^+	$0.015 - 1.509$	1/3	$0.52 - 0.70$
[51]$^{\|}$	2.24	2.45	100	$10^3 - 10^+$	$0.1 - 10^+$	0.0008^+	$0.020 - 2.038$	1/3	$0.53 - 0.77$
[51]$^{\|}$	1.73	2.00	100	$10^3 - 10^+$	$0.1 - 10^+$	0.0008^+	$0.025 - 2.502$	1/3	$0.52 - 0.78$
[51]$^{\|}$	1	1.41	100	$10^3 - 10^+$	$0.1 - 10^+$	0.0008^+	$0.035 - 3.536$	1/3	$0.38 - 0.39$
[51]$^{\|}$	0.71	1.23	100	$10^3 - 10^+$	$0.1 - 10^+$	0.0008^+	$0.041 - 4.077$	1/3	$0.40 - 0.44$
[51]$^{\|}$	0.55	1.14	100	$10^3 - 10^+$	$0.1 - 10^+$	0.0008^+	$0.044 - 4.381$	1/3	$0.40 - 0.44$
[51]$^{\|}$	0.32	1.05	100	$10^3 - 10^+$	$0.1 - 10^+$	0.0008^+	$0.048 - 4.762$	1/3	$0.37 - 0.43$
[14]	1	70.71	$2.4 \cdot 10^{-7}$	10^4	–	0.00008	$0.0193 - 1.93^{\ddagger\ddagger}$	2/3	
[75]	∞	0.01	10^6	–	10	$-^{\dagger}$	$0.0054 - 54$	1/3	$0.52 - 1.13$
[76]	∞	0.01	10^6	–	–	$-^{\dagger}$	$0.0054 - 54$	1/3	$0.56 - 1.08$
[77]	∞	0.01	10^6	–	–	$-^{\dagger}$	$0.00054 - 54$	1/3	$0.48 - 0.94$
[71]	∞	0.01	50	$-^{**}$	–	$-^{\dagger}$	$0.001 - 20$	1/3	$0.52 - 0.97$

* This study applies the turbulence as a superposition of two individual models: 20% slab and 80% 2D.

** This study uses a discrete cubic grid instead of the superposition of plane waves for generating the fluctuations.

† The lower boundary of the validity range can only be determined with the information of l_{low} (see Equ. (2.29)).

‡ The gyroradius had to be transformed from $R_{\text{g}} \propto 1/B$ into $R_{\text{g}} \propto 1/\sqrt{B^2 + b^2}$ together with all related parameters.

‡‡ The definition of the gyroradius is not given. A transformation as presented in the footnote ‡ may be necessary.

$^{|}$ The findings were converted from the Kraichnan case to the Kolmogorov case by using $\gamma_{\text{Ko}} = \gamma_{\text{Kr}} - 1/6$

The Figure 3.1 highlights also the dependencies of the diffusion coefficients on simulation parameters and combines them such that their origin – either physical or numerical – is shown. The present Chapter therefore provides an important step toward investigating physical diffusion coefficient dependencies by resolving those numerical issues, most notably by introducing parameter combinations from which the diffusion coefficient has a real functional dependence, in addition to convergence tests for those combinations that depict a numerical influence.

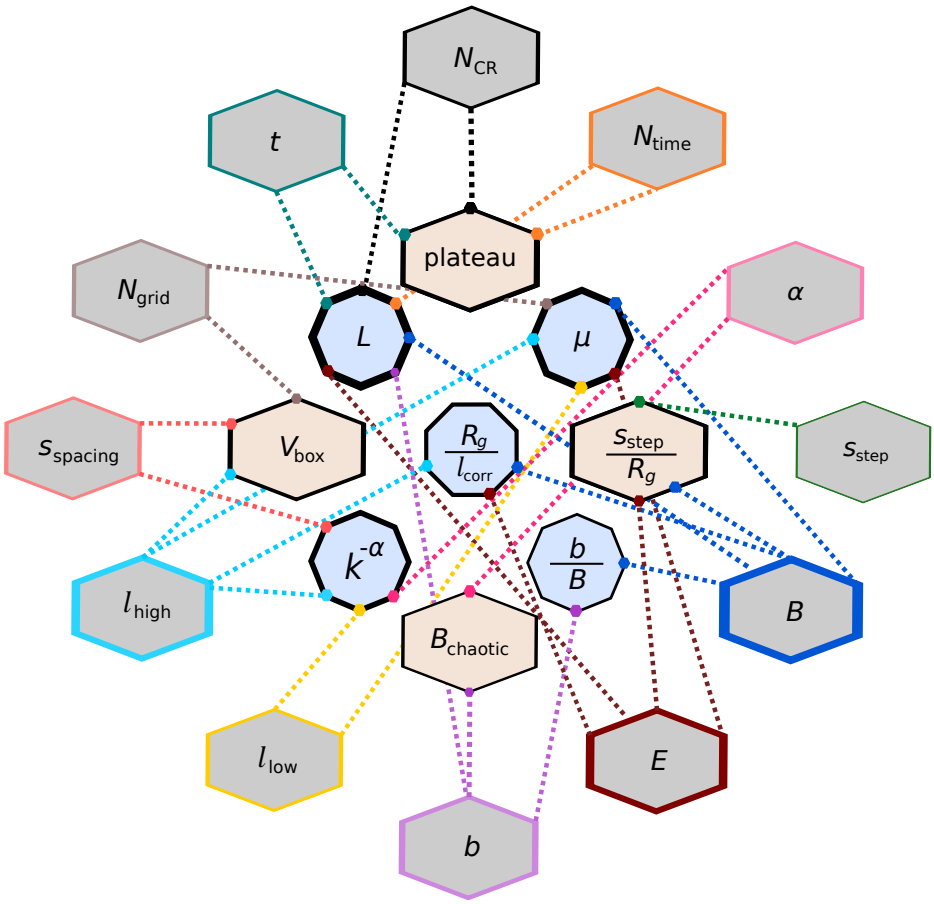

Figure 3.1: The gray hexagons embody the simulation parameters which can influence the diffusion coefficient but are not necessarily independent of each other. The inner nine colored boxes, on the other hand, comprise the parameter combinations on which the diffusion coefficient has a functional dependence. The colors distinguish their different origin - parameter combinations in beige derive from numerical settings, while the parameter combinations in light blue depict a physical influence. The stroke width indicates either the total influence of each simulation parameter (gray hexagon) on the inner parameter combinations or how much an inner combination (colored box) depends on the individual simulation parameters (see Chapter 3.1 for their definition).

3.1 Simulation Setup with CRPropa

As already mentioned, the simulations were performed within the CRPropa framework. This Section introduces all simulation parameters and places them in the appropriate context.

3.1.1 Magnetic Field

- **Stationary Magnetic Fields**: The diffusion time of relativistic charged particles is much shorter than the time scale of electrostatic acceleration effects [80]. As a consequence, electric fields are neglected and magnetic fields are set to be stationary.

- **Background Magnetic Field**: The regular field $\mathbf{B}$ is chosen to be aligned with the x_3-axis, i.e. $\mathbf{B} = B \cdot \mathbf{e}_{x_3}$ with $B = 1\,\text{Gauss}$.
- **Test Particle Approach**: Cosmic rays do not only change their trajectories due to the magnetic field, but also influence the magnetic field lines because of their charge. This feedback from the particles on the magnetic fields, however, is neglected in CRPropa. This is a reasonable assumption for high-energy particles at TeV-energies, as the effects are stronger for the lowest (GeV-) energies in the Galactic environment.
- **Grid Structure**: A discrete storage of the turbulent magnetic field b on a symmetric grid structure with N^3_{grid} grid points and a spacing s_{spacing} constrains the possible plasma waves that can fit into the box size, being subject to the conditions

$$l_{\text{low}} \geq 2 \cdot s_{\text{spacing}}, \tag{3.1}$$

$$l_{\text{high}} \leq N_{\text{grid}} \cdot s_{\text{spacing}}/2 \leq N_{\text{grid}} l_{\text{low}}/4, \tag{3.2}$$

  where l_{low} is defined as the smallest wavelength and l_{high} represents the largest wavelength of the plasma waves that are allowed by the simulation.
- **Interpolation Routine**: The magnetic field at an arbitrary trajectory position has to be interpolated based on the surrounding discrete magnetic field vectors at the grid points. The interpolation is achieved by a linear interpolation routine.
- **Turbulent Spectrum**: With those constraints on the possible range of plasma wavelength, the energy spectrum $G(k)$ with the wave vector $k = 2\pi/l$ is given by

$$G(k) \propto \begin{cases} 0 & \text{if } k < k_{\text{low}} \\ \left(\frac{k}{k_0}\right)^{-\alpha} & \text{if } k_{\text{low}} \leq k \leq k_{\text{high}} \\ 0 & \text{if } k_{\text{high}} < k \end{cases}, \tag{3.3}$$

  where α is the spectral index. Different well-known cases are presented in Fig. 3.2.
- **Turbulent Magnetic Field**: The complex turbulent magnetic field vectors $\mathbf{b}(\mathbf{k})$ are first defined on a regular grid in the three-dimensional wave number space

$$\mathbf{b}(\mathbf{k}) = \chi(\mathbf{k})\, G(k)^{1/2} k^{-1} [\mathbf{e}_1(\mathbf{k}) \cos(\Phi(\mathbf{k})) + \mathbf{e}_2(\mathbf{k}) \sin(\Phi(\mathbf{k}))] \exp(\mathrm{i}\Theta(\mathbf{k})) \tag{3.4}$$

  where $\mathbf{e}_1(\mathbf{k})$ and $\mathbf{e}_2(\mathbf{k})$ are randomly oriented vectors confined to the plane perpendicular to the random wave vectors $\mathbf{k}$. The polarization of the turbulent magnetic field depends on the random phases $\Theta(\mathbf{k})$ and $\Phi(\mathbf{k})$. $\chi(\mathbf{k})$ is introduced to guarantee the mean of $\mathbf{b}(\mathbf{k})$ to be 0. The orthogonal base $\mathbf{k}_{\text{n}}/k_{\text{n}}$, $\mathbf{e}_1$, $\mathbf{e}_2$ ensures that $\nabla \cdot \mathbf{b} = 0$. The turbulent magnetic field on a regular, three-dimensional Cartesian grid is generated using the inverse Fourier transformation of Equ. (3.4).
- **Gyroradius**: The gyroradius R_{g} is defined in accordance to [11, 14, 15, 17] as

$$R_{\text{g}} \propto \frac{E}{\sqrt{b^2 + B^2} cq}. \tag{3.5}$$

- **Correlation Length**: The correlation length, further denoted as l_{corr}, is defined as the characteristic length over which fluctuations in the interstellar magnetic field are correlated. This quantity is calculated using l_{high} and the ratio $r = l_{\text{low}}/l_{\text{high}}$ as well as on the spectral index of the turbulence spectrum α [72]

$$l_{\text{corr}} = \frac{l_{\text{high}}}{2} \cdot \frac{\alpha - 1}{\alpha} \cdot \frac{1 - r^{\alpha}}{1 - r^{\alpha - 1}}. \tag{3.6}$$

In general, r should be set as small as possible in order to study a wider range of parameters. This results in an equation for l_{corr} that depends only on the spectral index α and the maximum wavelength of the plasma waves. For a Kolmogorov spectrum with $\alpha = 5/3$, the correlation length yields

$$l_{\text{corr}} = \frac{l_{\text{high}}}{5}. \tag{3.7}$$

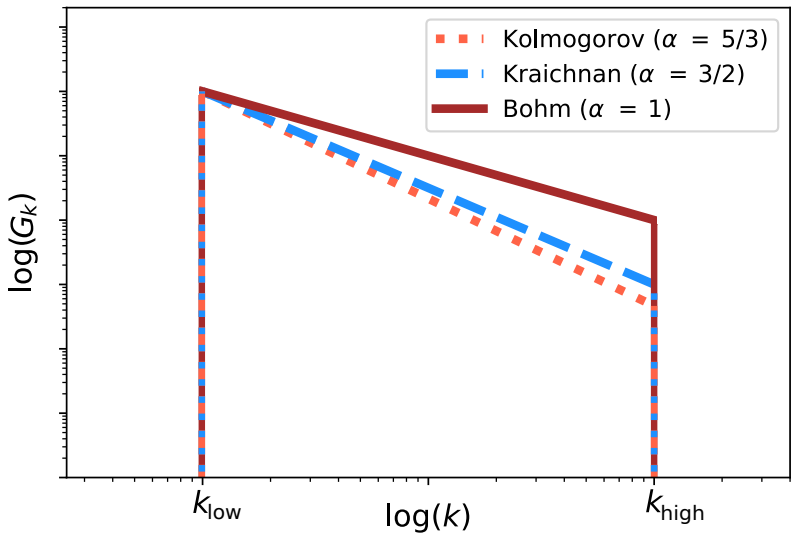

Figure 3.2: Energy spectrum of the turbulent magnetic field normalized at k_{low}. Comparison of three different spectral indexes as denoted in the legend.

3.1.2 Source – Particle Injection

Two different injection methods are used in this thesis. One method generates isotropic pitch angles, while the other method restricts the pitch angle of the injected particles to a certain value. The pitch angle Θ_0 is defined as the angle between the particle direction and the magnetic field. μ is defined as $\mu = \cos(\Theta_0)$.

- **Calculation of Diffusion Coefficient**: Isotropic emission from the center of the simulation volume. This isotropic particle injection is applied during the diffusion coefficient calculation.
- **Investigation of Mirror Effects**: The mirror effect is investigated using low energy particles which are injected with the same pitch angle.

3.1.3 Integration Routine

There exist many different numerical solvers of differential equations. An increasing number of studies have found that there are two algorithms, which work in general best for propagating charged particles within a magnetic field [81–83]. Both are introduced below and compared in a general test in Fig. 3.3. Convergence tests for both algorithms for the special case of computing the spatial diffusion coefficients, are presented in Fig. 3.7 including also a comparison of their computation times.

- **Cash-Karp**: The Cash-Karp method [81] is an integrator and based on adaptive Runge–Kutta methods. The method estimates the local truncation error of a single Runge–Kutta step. However, the long-term truncation error is not restricted, which may rise energy conservation issues. There

exist both implicit and explicit algorithms, with different advantages. Propagation algorithms, however, have high requirements of the computation time spend in each step, such that the advantage of fast computation of the implicit method surpasses the greater range of stability of the explicit algorithm.

- **Boris Push**: The Boris push resolves the implicit velocity dependence in the equations of motion, stated in the Lorentz force, by exploiting the rotational character of the magnetic field contribution. It thus provides a fully explicit particle pusher and due to its fast computation and longterm precision, it has become the standard for advancing a charged particle within a magnetic field [82, 83]. The Boris push guarantees the conservation of phase space volume, even though it is not symplectic.

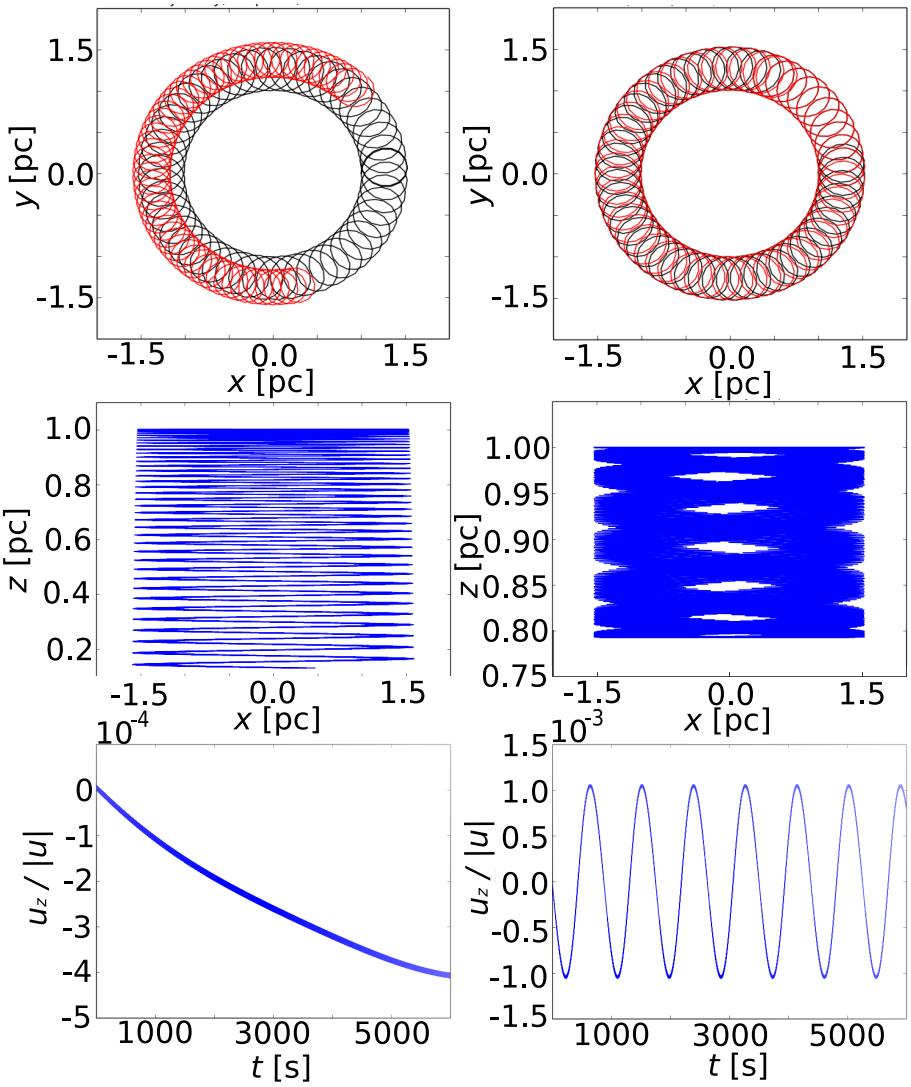

Figure 3.3: Comparison of a third-order Runge-Kutta algorithm (left side) with the Boris push method (right side) in a magnetic field $B_z \propto R$ together with an electric field $E_R \propto R^{-2}$. The configuration of electromagnetic fields results in gradient and $(E \times B)$ drifts. The first two rows display the spatial trajectory of the particles in the $(x-y)$- and $(x-z)$-plane, respectively. The last row indicates the local truncation error of the velocity in z-direction. Even though the local truncation error on the velocity is smaller with the Runge-Kutta algorithm, it sums up and leads to a longterm error in the particle trajectory. On the right side, the longterm precision of the Boris push method is indicated. This test is taken from [84] and edited with [33].

3.2 Numerical Influences on Diffusion Coefficients

This Section analyses the parameter combinations that influence the diffusion coefficient by adding numerical artifacts. The parameters that influence the diffusion coefficient by adding numerical artifacts are presented as the beige hexagons in Fig. 3.1. Their investigation is subject of this Section. In addition to unraveling the diffusion coefficient dependencies on numerical effects, parameters are presented that minimize this influence, which were discovered during convergence tests.

3.2.1 Reaching of the Plateau

Three simulation parameters may either prevent the running diffusion coefficient to reach the plateau or add a wiggling effect due to statistical uncertainties.

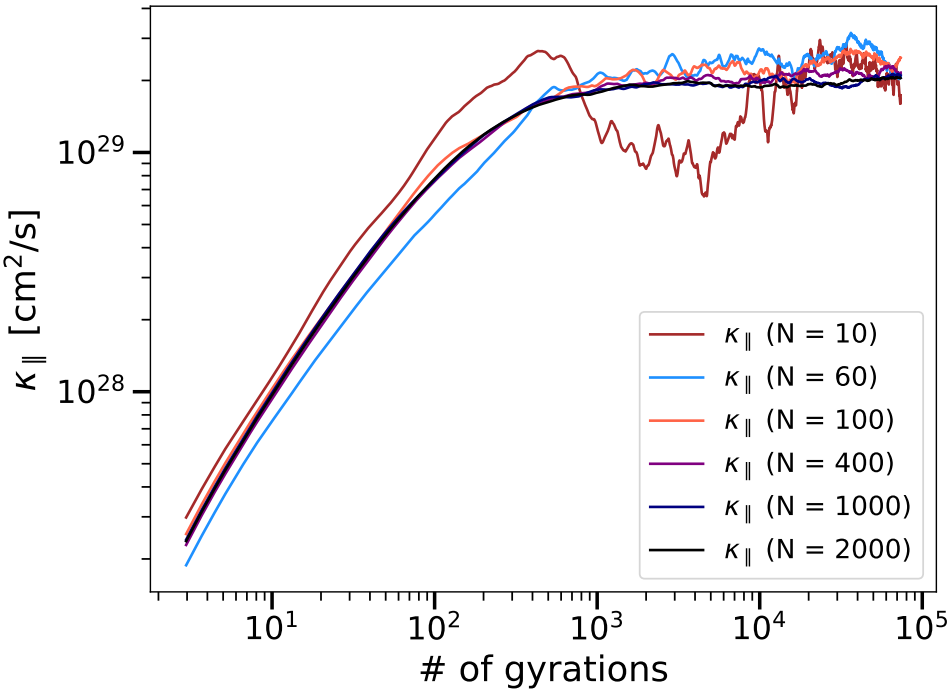

Figure 3.4: Running diffusion coefficient for simulations with different numbers of grid points and particles with $E = 100000$ TeV. Each running diffusion coefficient converges to a plateau with different values. Simulated with $l_{\text{low}} = 1.7$pc, $l_{\text{high}} = 82.45$pc, $s_{\text{spacing}} = 0.17$pc, $N_{\text{grid}} = 1024$, $N_{\text{time}} = 100000$, $b = 0.1\mu$G and $B = 1\mu$G.

- **Simulation Time**: The former influence is caused by the simulation time. The particles need some time to reach the plateau, which is, however, a physical effect and therefore covered in Chapter 3.3.
- **Number of Particles**: In Fig. 3.4, the running parallel diffusion coefficients are presented as functions of the number of gyrations. Simulations with different numbers of particles are indicated with different colors. Further lin-lin plots as well as log-log plots for different energies are presented in Appendix I. The wiggling of the running diffusion coefficient is due to an insufficient number of particles. An increased number of particles does not only stabilize the plateau, but also helps to find the exact transition between an increasing running diffusion coefficient and its plateau.
- **Number of Measurements**: The number of time steps during the trajectory of the particle at which information are written out, influences the diffusion coefficient calculated with the TGK method, since it is based on all previous time steps. The smaller the steps at which information is

available, the faster the diffusion coefficient based on the TGK method converges. Consequently, this parameter has no influence on the second moment method.

In addition, the method to compute the diffusion coefficient based on position and momentum information of the particles, can influence the quality of the plateau as well, as discussed below and presented in table 3.2.

Calculation Method Previous work has applied the straightforward method of calculating the diffusion coefficient based on the squared particle displacement $\langle \Delta x_\mathrm{i}^2 \rangle$ averaged over all particles as presented in Equ. (2.23) (see [63] and references within it). This method will be further denoted as 'second moment'. It has been suggested recently [11] to apply an alternative method, which is based on the TGK formalism and derived in Chapter 2.1.1. The angular brackets in Equ. (2.5) indicate averaging over the product of particle displacements and velocities for multiple time intervals Δt on a specific particle trajectory. Afterwards, the running diffusion coefficient is averaged over all simulated particles. Another method is based on Equ. (2.21) which is the solution to the diffusion Equ. (2.7). The Gaussian fit to the particle distribution delivers the diffusion coefficient from its fit parameters. The three methods are summarized in table 3.2.

Table 3.2: Methods for numerical calculation of the diffusion coefficient.

Method	Calculation	Equ.
TGK-Formalism	$\kappa_{x_i x_i} = \langle (v_{x_i}(t) \Delta x_i) \rangle$	(2.5)
Diffusion Equation	$\kappa_{x_i x_i} = \sigma/(2t)$	(2.7)
Second Moment	$\kappa_{x_i x_i} = \lim_{t \to \infty} \frac{\langle (\Delta x)^2 \rangle}{2t}$	(2.23)

The running diffusion coefficient converges faster toward its final value in the TGK-method because this method depends on the local changes within two time steps and by construction does take previous particle distributions into account. The method based on the second moment of the distribution, on the other hand, solely depends on the displacement at a certain time with respect to the starting point. However this advantage vanishes for large numbers of particles and long trajectories. Instead of determining a method in advance, both the TGK-formalism and the second method will be used to calculate the diffusion coefficient by averaging the running diffusion coefficient as soon as the plateau is reached. The values with the smaller uncertainties will be chosen.

3.2.2 Influence of the Box Size

The box size is defined by the number of grid points N_grid and the spacing s_spacing between them. The volume is given by $V_\mathrm{box} = (N_\mathrm{grid} \cdot s_\mathrm{spacing})^3$. All relevant parameters are first listed below independently from each other, followed by a discussion of their connection.

- **Largest Plasma Wavelength**: The largest plasma wavelength l_high has to fit into the simulation volume. As a consequence, $l_\mathrm{high} \leq N_\mathrm{grid} \cdot s_\mathrm{spacing}/2$ has to be fulfilled.
- **Number of Grid Points**: Fig. 3.5 presents the parallel running diffusion coefficients for different numbers of grid points. Interestingly, each running diffusion coefficient converges into a plateau, yet resulting in a different diffusion coefficient. There should be, however, just one value of the parallel diffusion coefficient, which is not yet known.
  Fig. 3.5 summarizes in the upper subplot the simulation results of varying the number of grid points, while varying the spacing between them at the same time. This subplot indicates that the

final value of the diffusion coefficient does not only depend on the number of grid points. This finding motivates the discussion of the spacing between the grid points before discussing afterwards the total influence of the box size.

- **Spacing between Grid Points**: In addition to the number of grid points, their spacing between each other changes the diffusion coefficient, as shown in the second upper subplot in Fig. 3.5.

As explained above, Fig. 3.5 presents in the upper two subplots the values of the parallel diffusion coefficient as functions of the number of grid points while varying the spacing between them and the spacing while varying the number of grid points, respectively. Consequently, the parallel diffusion coefficient depends on the number of grid points and on the spacing between them, however, has no functional dependency of them, since there exist many diffusion coefficients for a specific number of grid points and spacing respectively. This makes it impossible to limit numerical influence by restricting those two parameters independently. Fig. 3.5 introduces the box size as a combined parameter that can resolve this issue. The lowest subplot presented in Fig. 3.5 shows the parallel diffusion coefficient for different values of the product of the number of grid points with the spacing between them. This product delivers a criterion for minimizing this numerical effect. The third upper subplot in Fig. 3.5 indicates with a colormap the simulation time for simulations with different numbers of grid points and different spacings between them. Increasing the number of grid points for a constant spacing, the numerical influence not only decreases, but the simulation time decreases as well. More discrete magnetic field vectors can be stored, which decreases the time consuming interpolation of the magnetic field at each particle position. The number of grid points is costly with respect to memory and therefore limited by the amount of available RAM.

3.2.3 Chaotic Magnetic Field

A chaotic system requires at least a three-dimensional field [85]. The configuration chosen in this work to guarantee a chaotic system is as follows: This thesis uses the construction of the turbulent magnetic field as described in Section 3.1.1. By construction, the distribution of Fourier modes follows a power law in wavenumber as predicted for instance in the Kolmogorov case. Its transformation on a spatial three dimensional grid structure guarantees a chaotic system [15]. A Kolmogorov-type spectrum with $\alpha = 5/3$ is used. In order to prove the chaotic character of the magnetic field used in this thesis, the diffusion coefficient is simulated several times with different magnetic field realizations, while all parameters remain constant. Fig. 3.6 presents simulated parallel diffusion coefficients in ten different simulation sets based on 10000 particles each. The y-axis shows the averaged parallel diffusion coefficient averaged over the number of sets denoted on the x-axis together with its statistic error. A slightly different injection direction results in complete different trajectories in such a chaotic field, such that it is sufficient to simulate just with one magnetic field realization as long as the particles are injected with different directions.

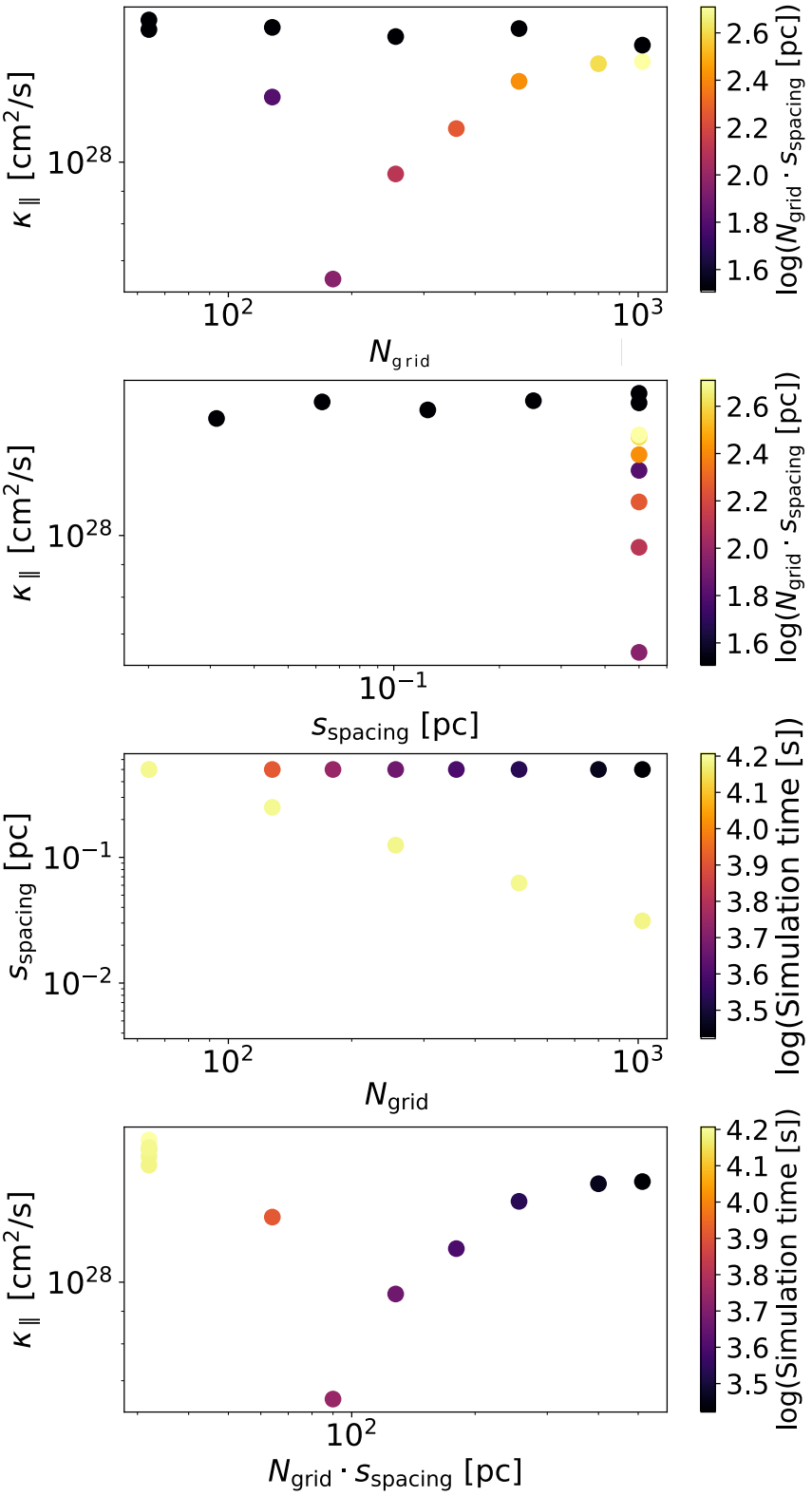

Figure 3.5: The first two upper plots present the influence from the number of grid points and the spacing between them. Both plots imply that those parameters depend on each other. The third upper subplot in Fig. 3.5 indicates with a colormap the simulation time for simulations with different numbers of grid points and different spacings between them. The lowest subplot presents the parallel diffusion coefficient for different values of the product of the number of grid points with the spacing between them. Simulated with $l_{\mathrm{low}} = 1.7$pc, $l_{\mathrm{high}} = 82.45$pc, $N_{\mathrm{time}} = 100000$, $b = 0.1\mu$G and $B = 1\mu$G.

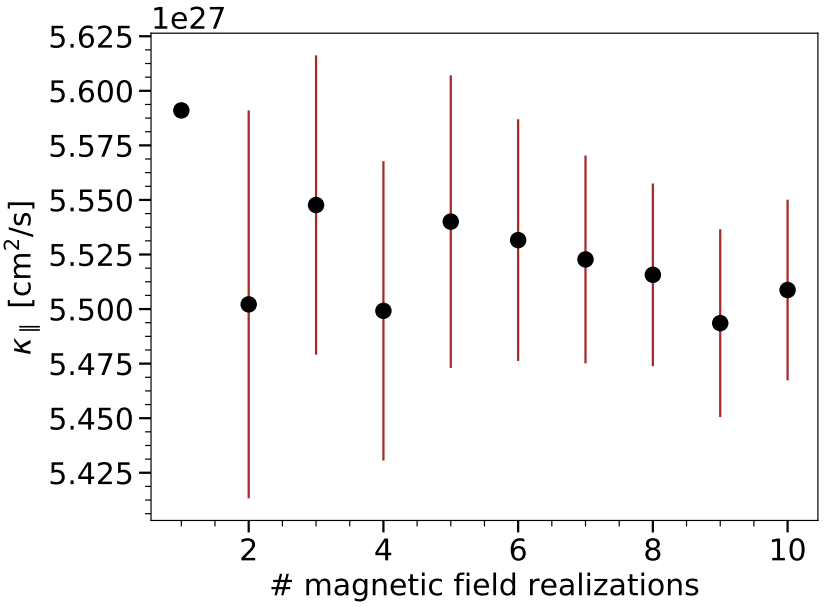

Figure 3.6: Diffusion coefficient averaged over different number of simulation sets as indicated in the x-axis together with its statistic error. Each set is based on 10000 particles with the same ratio of $b/B = 0.1$, however, different orientation of the turbulent magnetic field vectors according to Equ. (3.4).

3.2.4 Step Length of the Integration Routine

This Section continues the discussion already started in Chapter 3.1.3 for advancing a charged particle within a magnetic field. It compares the Cash-Karp algorithm with the Boris push method for the propagation within a magnetic field that consists of a background magnetic field and a turbulent component. Moreover, the trajectory length between two steps is set in relation to the gyroradius of the particle, such that the propagation is sufficiently accurate to completely resolve the gyromotion.

- **Step Length**: The propagation of particles within CRPropa is based on a repetitive process. At a given particle position, the equation of motion is solved. Afterwards, the particle will be propagated along the calculated direction for a certain distance. This distance between two steps is further denoted by the step length s_{step}. The trajectory length between two steps is crucial for the accuracy of the particle propagation within a magnetic field because numerical artifacts are introduced as soon as the magnetic field changes at faster scales than s_{step} or the given step length cannot resolve the gyromotion of the particle anymore.
- **Magnitude of Background Field**: For the case of a magnetic field with a background magnetic field aligned along a certain direction, gyration motions will dominate at least on short time scales as pointed out in Fig. 1.6. To resolve this gyration of the particle, the step length has to be significantly smaller than the gyroradius of the particle. The background magnetic field is related to the gyroradius as described in Equ. (2.46) and therefore has to be sufficiently large.
- **Energy of Particle**: Equ. (2.46) not only connects the magnitude of the background field with the gyroradius, but relates also the particle energy with it. In order to resolve the gyromotion of the particle, the energy has to be sufficiently small, such that the resulting gyroradius for the given background magnetic field is small enough.

Fig. 3.7 quantifies the above statements: it presents the comparison of both propagation methods with respect to the value of the diffusion coefficient and with respect to the computation time. The shown data confirms the intuitive guess that a spacing on order of the gyroradius is necessary in order to resolve the gyration motion of the particle. The diffusion coefficient converges for $s_{\text{step}} = R_{\text{g}}$ for both

methods. Depending on the step length, the simulation time differs by a factor of at least 5, in favor of the Boris push.

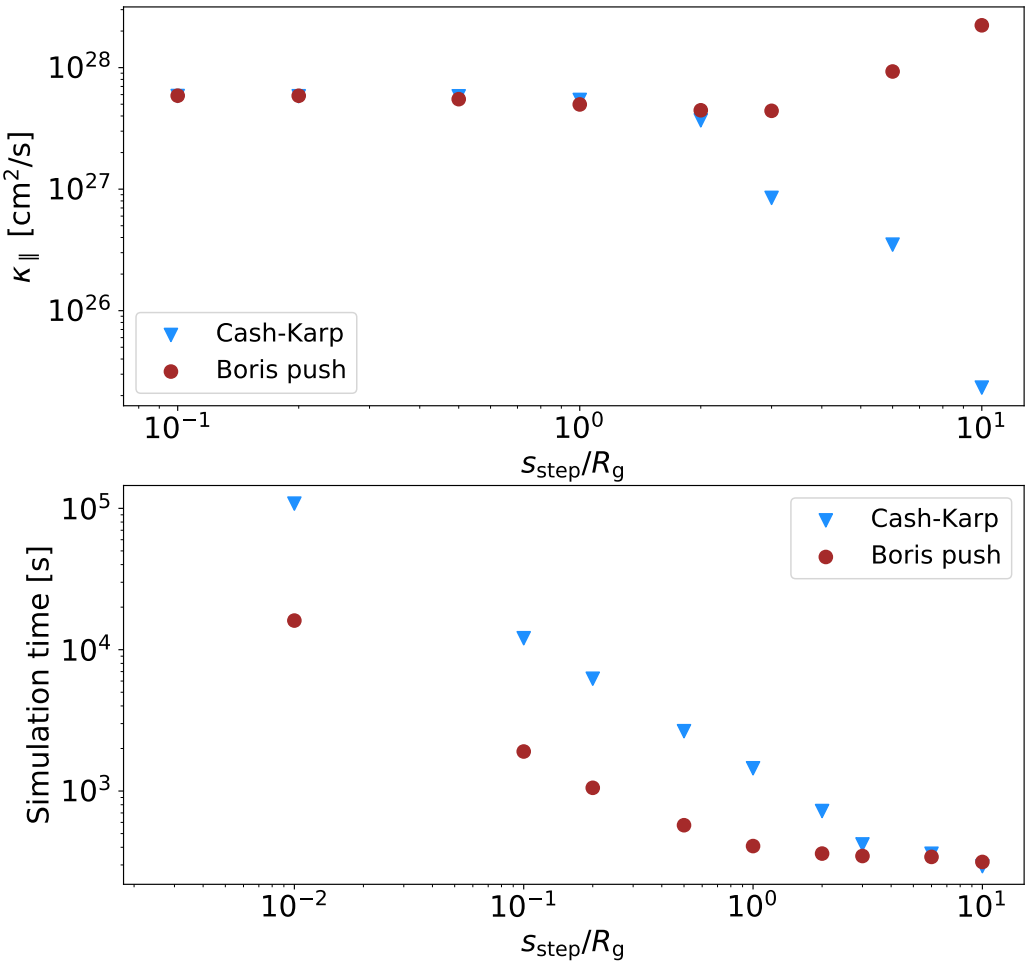

Figure 3.7: Comparison of both propagation methods – namely the Kash-Carp algorithm and the Boris push – with respect to the value of the diffusion coefficient (upper plot) and with respect to the computation time (lower plot) as a function of the step lengths. Simulated with $l_{\mathrm{low}} = 1.7$pc, $l_{\mathrm{high}} = 82.45$pc, $E = 8900$ TeV, $N_{\mathrm{grid}} = 1024$, $N_{\mathrm{time}} = 100000$, $b = 0.1\mu$G and $B = 1\mu$G.

3.2.5 Interpolation Influence

The turbulence spectrum is generated on the grid points as explained in Section 3.1.1 using the power-law described by the Kolmogorov turbulence in Fourier Space. Despite the accuracy of the turbulence energy spectrum on the grid points, it deviates from the expected energy spectrum for interpolated fluctuations in between the surrounding grid points. Fig. 3.8 shows the value of $(-\alpha - 2)/2$ averaged over the complete volume of the simulation box. This value is presented because it enters equation 3.4, given that $G(k)^{1/2}k^{-1})$ yields $k^{(-\alpha-2)/2}$. It takes measurements of the turbulent spectrum (as sketched in Fig. 3.2) at various positions into account for which the values of α are calculated for different ranges of the plasma wavelengths l. The measurements at different positions between the

grid points are averaged such that the spectrum represents that of the average particle interaction position as illustrated and discussed in detail in the appendix B.

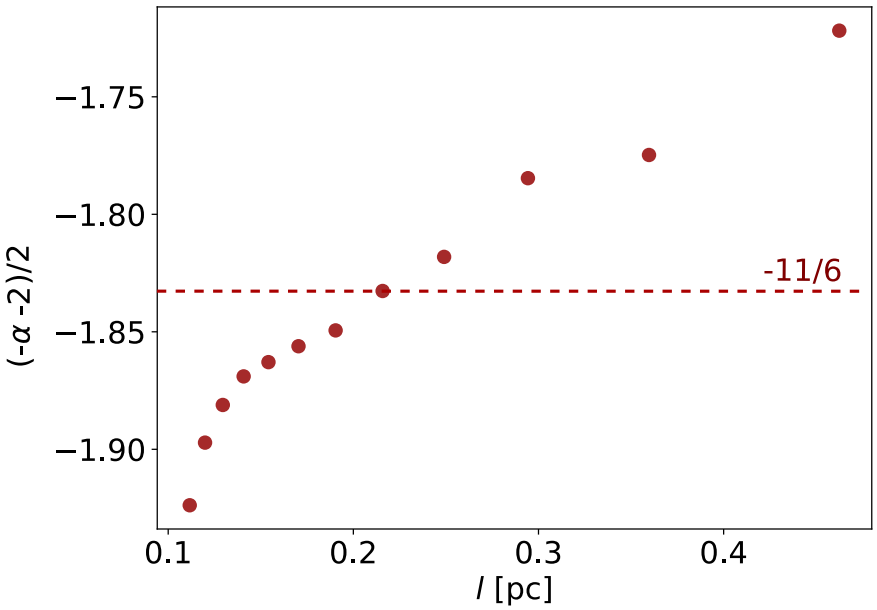

Figure 3.8: Interpolated averaged spectral index for different ranges of the plasma wavelength. This differs significantly from the constant spectral index, that is put into the simulation on the grid points as indicated with the red dashed line. The slope is steeper for regions with lower wavelengths and consequently flatter for higher wavelengths.

Interestingly, the spectrum is steeper for small wavelengths of the turbulence than what is set in the simulation in the first place, which is $(-\alpha - 2)/2 = -11/6$ for the case of Kolmogorov turbulence with $\alpha = 5/3$.
In order to highlight the importance of these findings, an outlook to the detailed discussion about the pitch angle scattering efficiency (see Section 3.3.2) is presented below. The gyroresonance condition relates the range of plasma waves l with which a particle with a certain gyroradius R_g resonantly interacts

$$|\mu| = \frac{l}{2\pi R_\mathrm{g}}, \tag{3.8}$$

where $|\mu|$ is defined as the absolute value of the cosine applied to the pitch angle Θ_0. The pitch angle Θ_0 is defined as the angle between the particle direction and the magnetic field. Fig. 3.9 presents the diffusion coefficients as functions of $R_\mathrm{g}/l_\mathrm{corr}$. In addition, the range of plasma waves are presented with which a particle could interact resonantly with a certain ratio of $R_\mathrm{g}/l_\mathrm{corr}$ according to Equ. (3.8). The gray line presents the upper border of the fluctuation wavelengths within the shown simulations. Up to a ratio of $R_\mathrm{g}/l_\mathrm{corr} = 5/(2\pi)$, the present fluctuation wavelengths between l_low and l_high are sufficient for the resonant scattering processes. The green area shows the fraction of plasma waves which is available for resonant interactions with a particle of a specific ratio $R_\mathrm{g}/l_\mathrm{corr}$. Increasing the ratio $R_\mathrm{g}/l_\mathrm{corr}$ further, results in the necessity of larger fluctuation wavelengths which are not presented in the simulation. The red area in the lower subplot marks the increasing fraction of missing resonant scattering.
Particles with a ratio of $R_\mathrm{g}/l_\mathrm{corr} \lesssim 1$ can interact over the whole range of l between l_low and l_high and therefore both large and small plasma waves are used. The influences of the different spectral slopes presented in figure 3.8 cancel each other out so that there is a vanishing net influence of the interpolation issue. However, by reducing the energy of the particle, only fluctuations with smaller

wavelengths are able to resonantly interact with the particle.
Consequently, this figure indicates a higher influence of the interpolation issue for low energy particles since they favor interactions with short-wavelength fluctuations as will be discussed in detail in Section 3.3.2 and stated in Equ. (3.12).

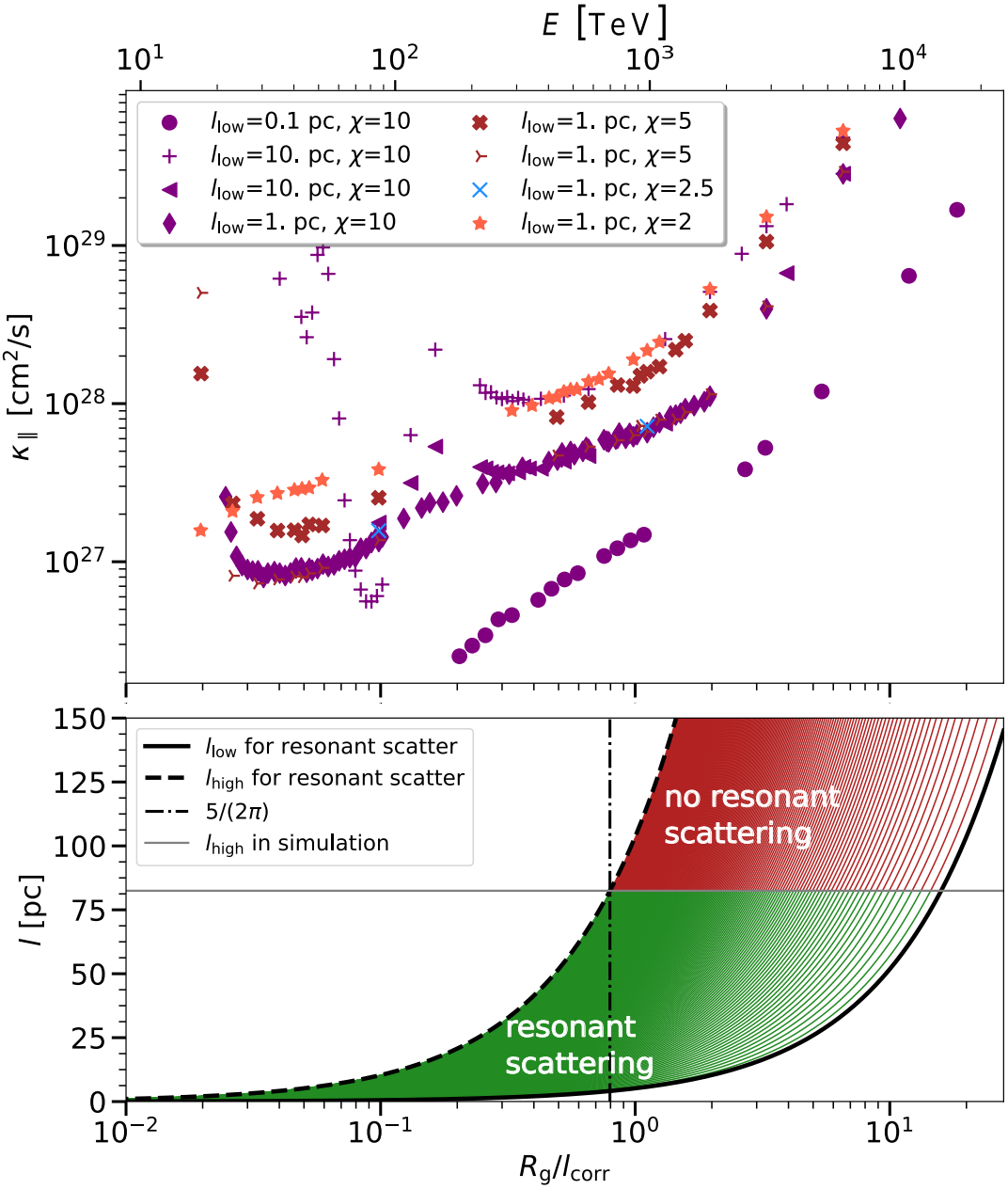

Figure 3.9: *Upper panel*: Parallel diffusion coefficients as functions of the gyroradius divided by the correlation length of the turbulent magnetic field. Each diffusion coefficient is calculated, as outlined in Section 3.2.1, based on 1200 particles and varying parameters according to the legend, however, without adjusting the magnetic field strength and the maximum plasma wavelength, which are set to $b = 10^{-7}$ Gauss, $B = 10^{-6}$ Gauss and $l_{\mathrm{corr}} = 82.45/5.$ pc, respectively. χ is defined as $s_{\mathrm{spacing}}/l_{\mathrm{low}}$. *Lower panel*: Presents the range of the plasma wavelengths that can scatter resonantly with particles with a certain ratio $R_{\mathrm{g}}/l_{\mathrm{corr}}$ according to Equ. (3.8).

3.3 Physical Influences on Diffusion Coefficients

3.3.1 Trajectory Length of Particles

In Fig. 3.10, the running diffusion coefficients are presented as functions of the propagated distance in units of the gyrorations. Different ratios are investigated and presented with different colors. Particles injected isotropically from a point source into a partially ordered magnetic field, are dominated by the background field in an early phase and therefore gyrate around it. Each gyration equals a distance of $2\pi R_\mathrm{g}$ and can therefore be interpreted as the time $t = 2\pi R_\mathrm{g}/c$ traveled. After a certain time, the particle trajectories will be characterized by the turbulent magnetic field. The plateau of the running diffusion coefficient can be identified with the final diffusion coefficient and does not appear before the chaotic character of the trajectories dominates the gyromotion due to the background field. Consequently, the running diffusion coefficient can be classified into two time-resolved regimes:

1. **Weakly Perturbed Propagation Regime**: The background dominated regime (see left panel of Fig. 1.6 for a visualization) is revealed in in Fig. 3.10. During this phase it is reasonable to assume a constant parallel velocity (with respect to the background magnetic field), resulting in a proportional increase of distance in the x_3-direction with respect to its initial position. The parallel running diffusion coefficient therefore yields

$$\kappa_\parallel = \frac{\langle(\Delta x_3)^2\rangle}{2t} \propto \frac{t^2}{2t} = \frac{t}{2}. \tag{3.9}$$

   This regime is visible at least for the first ten gyrations in Fig. 3.10. The perpendicular diffusion coefficient is based on the movement in the perpendicular plane with respect to the background magnetic field. This movement is characterized by the constant gyromotion. The distance to the origin just varies between 0 and $2R_\mathrm{g}$. Without a turbulent magnetic field, all particles would come back to their origin after each gyration, resulting in a vanishing perpendicular diffusion coefficient. The turbulent magnetic field, however, is the reason for a slight displacement from their origin after one gyromotion, such that the running diffusion coefficient is not vanishing in its local minima after each gyration. Besides this wiggling effect, the perpendicular running diffusion coefficient decreases linearly with time in this first regime after $t = R_\mathrm{g}/c$ as a first approximation

$$\kappa_\perp = \frac{\langle(\Delta x_\perp^2)\rangle}{2t} \propto \frac{1}{2t}, \tag{3.10}$$

   as the displacement in perpendicular direction is of order of the gyroradius.
2. **Diffusive Propagation Regime**: For large times, the trajectories are mainly influenced by the turbulent magnetic field, and therefore best characterized by chaotic movement (see right panel in Fig. 1.6). In this limit, the diffusion coefficients are constant for both the parallel as well as the perpendicular component. The distance traveled, before diffusion starts will be approximately one mean free path

$$\lambda_\parallel = \frac{3\kappa_\parallel}{c}. \tag{3.11}$$

   After the traveled distance $\lambda_\parallel$, the direction of the particle is on average decorrelated from its initial direction. Consequently, this statistical process results in $\Delta x_i \sim \sqrt{t}$.

The simulation parameters below determine the particle trajectory length that is necessary in order to reach the plateau:

- **Simulation Time**: As a consequence of those two different regimes explained above, the simulation time has to be chosen to be long enough for the diffusion coefficient to reach the plateau. It is important to simulate at least ten times longer than what is supposed to be enough according to Equ. (3.11) to reach the plateau. There might be just an intermediate plateau due to some numerical issues, that might vanish after some time and result in another plateau with a different value for the diffusion coefficient. This additional expense is outweighed by reaching a correct and more accurate result, especially for low energies and low magnitudes of the fluctuating magnetic field.
- **Magnitude of Turbulent Field**: Decreasing the magnitude of the magnetic fluctuations increases the parallel diffusion coefficient due to less scattering. The effect is already indicated in Fig. 3.10. According to Equ. (3.11), larger diffusion coefficients need longer trajectories for reaching the plateau.
- **Energy of Particle**: Increasing the energy of the particle does also increase the diffusion coefficient. This means that the plateau is located at a higher value and thus the running diffusion coefficient requires more time to reach it.

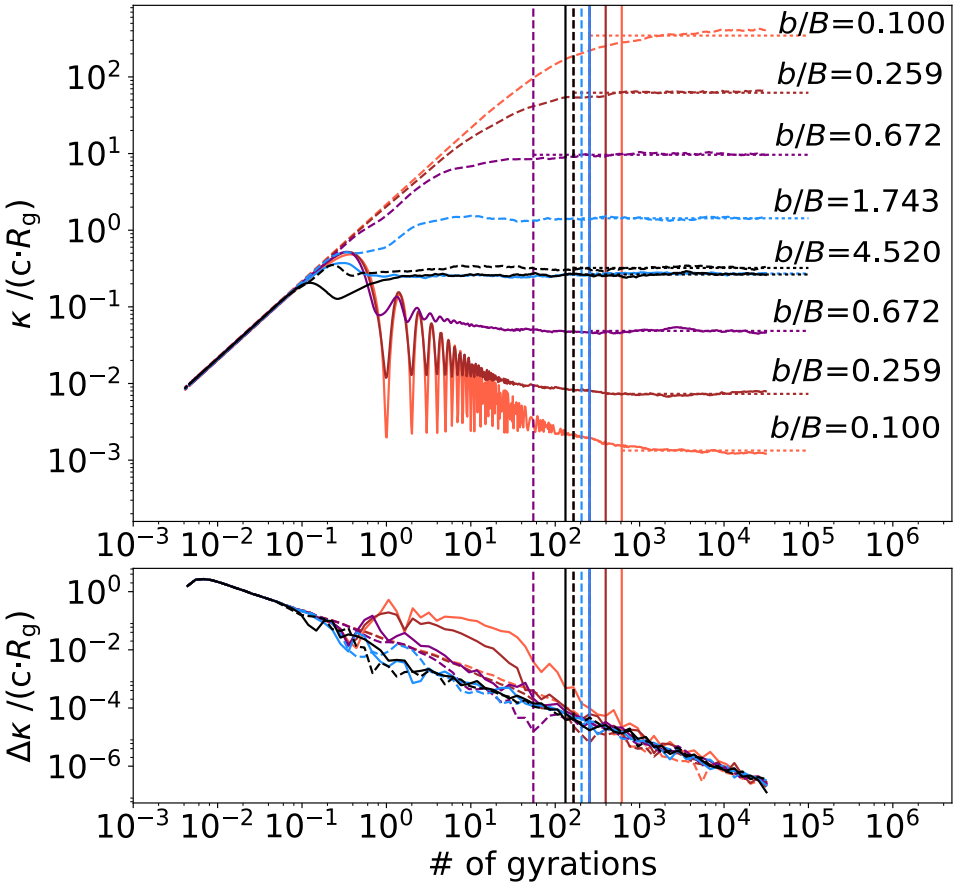

Figure 3.10: *Upper panel*: Diffusion coefficients divided by gyroradius as a function of number of gyrations at 10^5 TeV. Parallel diffusion coefficients are shown with ratios of b/B as indicated. *Lower panel*: Averaged derivation (over 10 data points) of the diffusion coefficient. The vertical lines are drawn as soon as the averaged derivations of the parallel diffusion coefficients are below an arbitrary critical value ($\approx 10^{-5}$).

3.3.2 Pitch Angle Scattering Efficiency – Classification in Regime

This Section addresses the question of the simulation parameters for which efficient scattering between the particles and the magnetic field fluctuations is possible. In doing so, the gyroresonance condition

is applied

$$|\mu| = \frac{l}{2\pi R_{\mathrm{g}}}. \tag{3.12}$$

This equation has to cover values for μ in the range of $|\mu| \leq 1$ such that particles can scatter efficiently with the magnetic field fluctuations without being restricted in their direction with regard to the background magnetic field orientation. Scatter is defined as the change in pitch angle. The successful fulfillment of this criterion depends on the range of wavelengths of the magnetic fluctuations and the gyroradius, which is based on the particle energy and the magnetic field magnitude (see Equ. (3.5)). These constraints can be summarized in the following condition

$$|\mu_{\mathrm{low}}| = \frac{l_{\mathrm{low}}}{2\pi R_{\mathrm{g}}} \leq |\mu| \leq \frac{l_{\mathrm{high}}}{2\pi R_{\mathrm{g}}} = |\mu_{\mathrm{high}}|, \tag{3.13}$$

where $|\mu_{\mathrm{low}}|$ should be close to 0 and $|\mu_{\mathrm{high}}|$ should be larger than 1, such that μ can cover the whole range between -1 and $+1$.

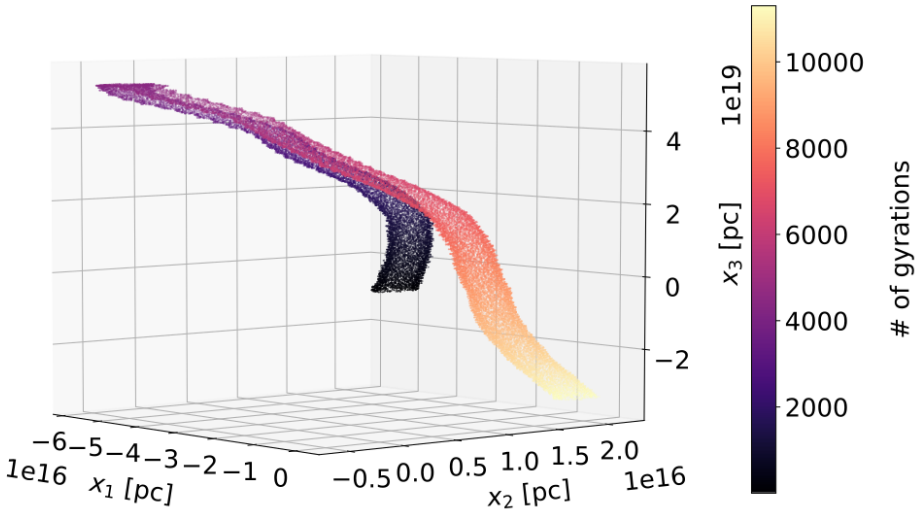

Figure 3.11: Example of a trajectory of a particle in a turbulent plus guide magnetic field, simulated with CRPropa using the following parameters: b = 10^{-8} Gauss, B = 10^{-6} Gauss, R_{g} = 0.109 pc. This 3D plot indicates a mirroring effect caused by the magnetic field lines, because the particle turns around completely with respect to the background field.

The central question is now: what is the influence of these (physical or unphysical) boundaries on the propagation of cosmic rays, and in particular on the diffusion coefficient? The physical motivation for the case, where scattering processes may be prevented around $\mu \approx 0$, however, is given by the idea to repair the diffusion coefficient so as to account for both gyroresonant scattering and mirroring [86, 87]. In any real plasma there is a minimum l_{low} in the wave spectrum and therefore a minimum μ_{low} at which particles can be gyroresonantly scattered given a certain gyroradius. This does depend in general on conditions in the plasma. For example, if the plasma is very hot, the thermal ions will be able to resonantly damp the waves. Whatever μ_{low} may be in astrophysical environments, the two questions which are addressed in this Section are related to possible mirror effects: is there enough power in long wavelength modes to mirror effectively? And are the necessary conditions for mirroring

fulfilled around $\mu \approx 0$? A first hint of the existence of mirror effects is illustrated in Fig. 3.11 and Fig. 3.12. Both show the same section of a particle within a magnetic field. In Fig. 3.13, the μ from 24 individual particles is presented as functions of the number of gyrations, also indicating the existence of mirror effects.

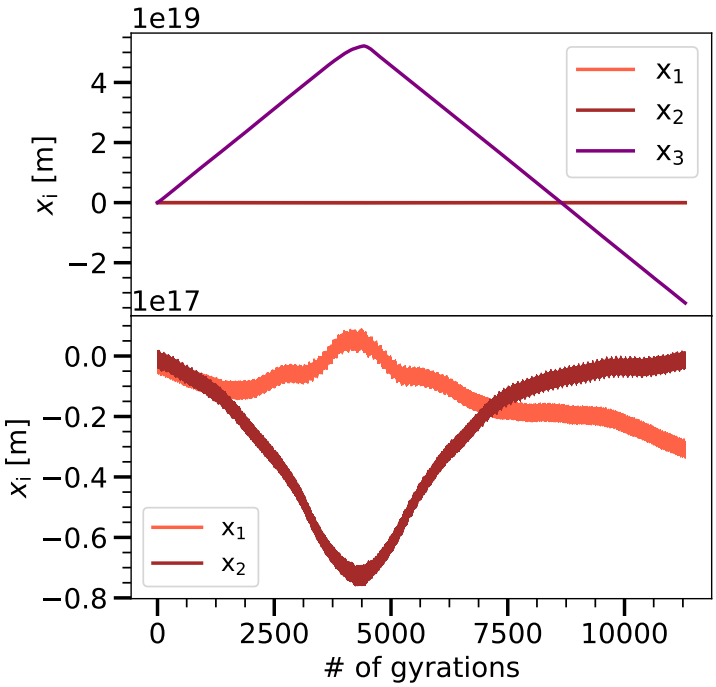

Figure 3.12: Projection of the particle trajectory shown in Fig. 3.11 onto the three coordinate axes. *Upper panel*: Comparison of particle motion in all three directions. The motion is dominated by its component in x_3-direction as it is expected for a strong guide field. *Lower panel*: The gyromotion in the perpendicular plane with respect to the background field is shown.

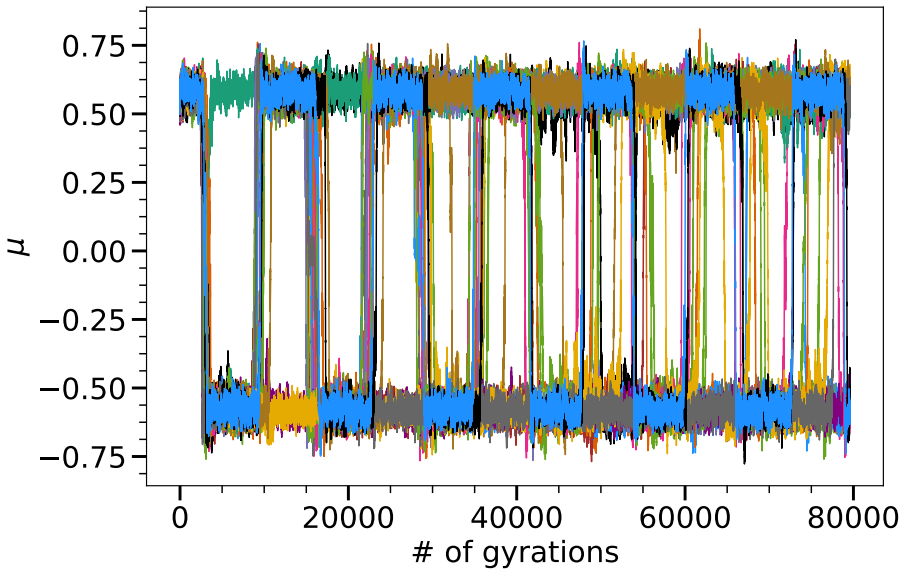

Figure 3.13: Study of 24 particles, which were all injected with $\mu = 0.5$. The magnetic field is dominated by the background field: $b/B = (1.05 \cdot 10^{-7}\,\text{Gauss})/(10^{-6}\,\text{Gauss})$.

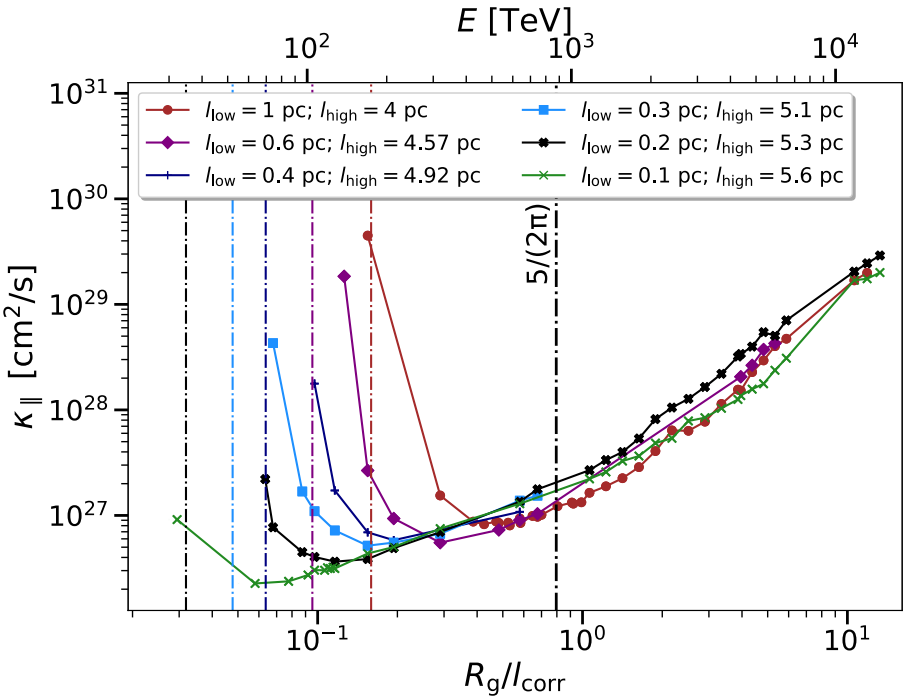

Figure 3.14: Diffusion coefficients as functions of the ratio R_g/l_{corr} for different values of l_{low} as indicated in the legend. l_{high} is chosen so that the correlation length is constant according to Equ. (3.6). The colored vertical lines are plotted according to Equ. (3.14) and mark the start into the transition into the diffusive-energy regime. The black line is plotted according to Equ. (3.18) and indicates the upper border of the diffusive regime.

1. **No Resonant Scattering** ($1 < |\mu_{low}|$): Particles cannot resonantly interact with the fluctuations for

$$\frac{R_g}{l_{corr}} \leq \frac{l_{low}}{2\pi l_{corr}}, \tag{3.14}$$

according to the gyroresonance condition in Equ. (3.12). The parallel diffusion coefficients are presented as functions of the ratio R_g/l_{corr} for $b/B = 0.1$ in Fig. 3.14. The boundary for resonant scattering according to Equ. (3.14) is indicated with the vertical dashed line for the different parameters l_{low}. As expected, the diffusion coefficient is larger without interactions for $R_g/l_{corr} \leq l_{low}/(2\pi)$, given that the particles do not turn around which would decrease their displacement to traveled distance to the center. Increasing either the energy or decreasing the correlation length decreases the gap of forbidden resonant interactions around $\mu = 0$. Therefore, Equ. (3.14) marks the start into the diffusive-energy regime. In Fig 3.16, data from [15] are presented. This plot shows the parallel diffusion coefficient as functions of the range R_g/l_{corr} for different ratios b/B as indicated in the legend. The start of the transition into the diffusive-energy regime is also presented. The end of this transition regime can be calculated in principle as discussed below, however, requiring the knowledge of parameters that are not given in [15].
2. **Missing Resonant Scattering** ($0 < |\mu_{low}| < 1$): This regime is the transition between the regime explained above and the diffusive-energy regime. The missing resonant scattering around $|\mu| = 0$ enables magnetic mirror effects as explained in the following:

i. First Criterion for Magnetic Mirroring: Without scattering, the magnetic moment of the particles with $\mu \approx 0$ is conserved. This is the first criterion for magnetic mirroring.

ii. Second Criterion for Magnetic Mirroring: The criterion for magnetic mirroring of particles with conserved magnetic moment yields $v_\perp/v > \sqrt{B_0/(B_1)}$, where $v_\perp$ is the perpendicular particle velocity with respect to the total magnetic field $\mathbf{B}_0$ ($\mathbf{b}$ + $\mathbf{B}$). B_1 is the total magnetic field at a future time on the particle trajectory. Therefore, particles are reflected when their perpendicular motion is high. Rearranging of the inequality delivers a new useful inequality

$$B_1 > B_0 \cdot \left(\frac{v}{v_\perp}\right)^2, \tag{3.15}$$

with which the mirror effect can be investigated. In doing so, this Section presents simulations with particles that were injected with the same value $\mu = \cos(\phi_0) = 0.5$, and thus demonstrates that a simple configuration of a background magnetic field together with a turbulent magnetic field (isotropic in 3D) can act as a magnetic mirror. Figure 3.15 presents different relevant quantities related to mirror effects as functions of the number of gyrations. The value of the right side term of the inequality (3.15) is depicted in Fig. 3.15 (see also Appendix K for different ranges of the number of gyrations) to color the upper two subplots. The color in those subplots represents therefore the minimum B_1 which is then needed for mirroring. Low values mean a higher probability of mirroring. The third subplot presents the magnetic moment as a function of the number of gyrations. The last subplot summarizes the first two subplots. It indicates if the inequality (3.15) is fulfilled. Fig. 3.15 shows that the magnetic moment of the particle is conserved (last subplot) and that the criterion (3.15) is fulfilled (third subplot). Consequently, both criteria for mirroring are fulfilled. Interestingly, the calculated range of μ with missing interactions agrees with the range of μ for which no resonant scattering is predicted according to the gyroresonance criterion

$$|\mu_{\mathrm{low}}| = \frac{l_{\mathrm{low}}}{2\pi R_{\mathrm{g}}} = \frac{0.04\mathrm{pc}}{2\pi \cdot 0.109\mathrm{pc}} \approx 0.06. \tag{3.16}$$

The upper range of the mirror regime can be defined so that no mirroring events take place above

$$\frac{R_{\mathrm{g}}}{l_{\mathrm{corr}}} = \frac{l_{\mathrm{low}}}{2\pi l_{\mathrm{corr}} \xi}, \tag{3.17}$$

where ξ is a parameter that depends on b/B ($\xi = 0.06$ for $b/B \ll 1$). Further studies have to reveal the exact relation between b/B and ξ. Appendix K presents a first attempt to relate the number of mirror effects with the energy of the particle as well as the ratio b/B. The main findings are that the number of magnetic mirror events increases for higher b/B even though the range of μ remains unchanged. This is caused by the fact that the change of μ increases in average with higher ratios of b/B. Consequently, the particles can faster scatter resonantly toward low values of μ and afterwards mirror around $\mu = 0$.

3. **Complete Resonant Scattering** ($|\mu_{\mathrm{high}}| > 1$; $|\mu_{\mathrm{low}}| \approx 0$): The previous discussion of the mirror effect is beneficial, since it delivers a lower boundary $|\mu_{\mathrm{low}}|$ for which particles still can scatter resonantly around $\mu \approx 0$ and presents consequently a lower border of the diffusive-energy regime. By considering the largest plasma wavelength $\mu_{\mathrm{max}} \stackrel{!}{=} 1 = l_{\mathrm{high}}/(2\pi \cdot R_{\mathrm{g}}) = 5 \cdot l_{\mathrm{corr}}/(2\pi \cdot R_{\mathrm{g}})$, an upper border of the diffusive-energy regime can be calculated as

$$\frac{R_{\mathrm{g}}}{l_{\mathrm{corr}}} = \frac{5}{2\pi}. \tag{3.18}$$

Fig. 3.17 presents in the lower panel an graphical illustration of the gyroresonance condition for the given range of plasma wavelengths in the simulations. The area with the gray vertical lines

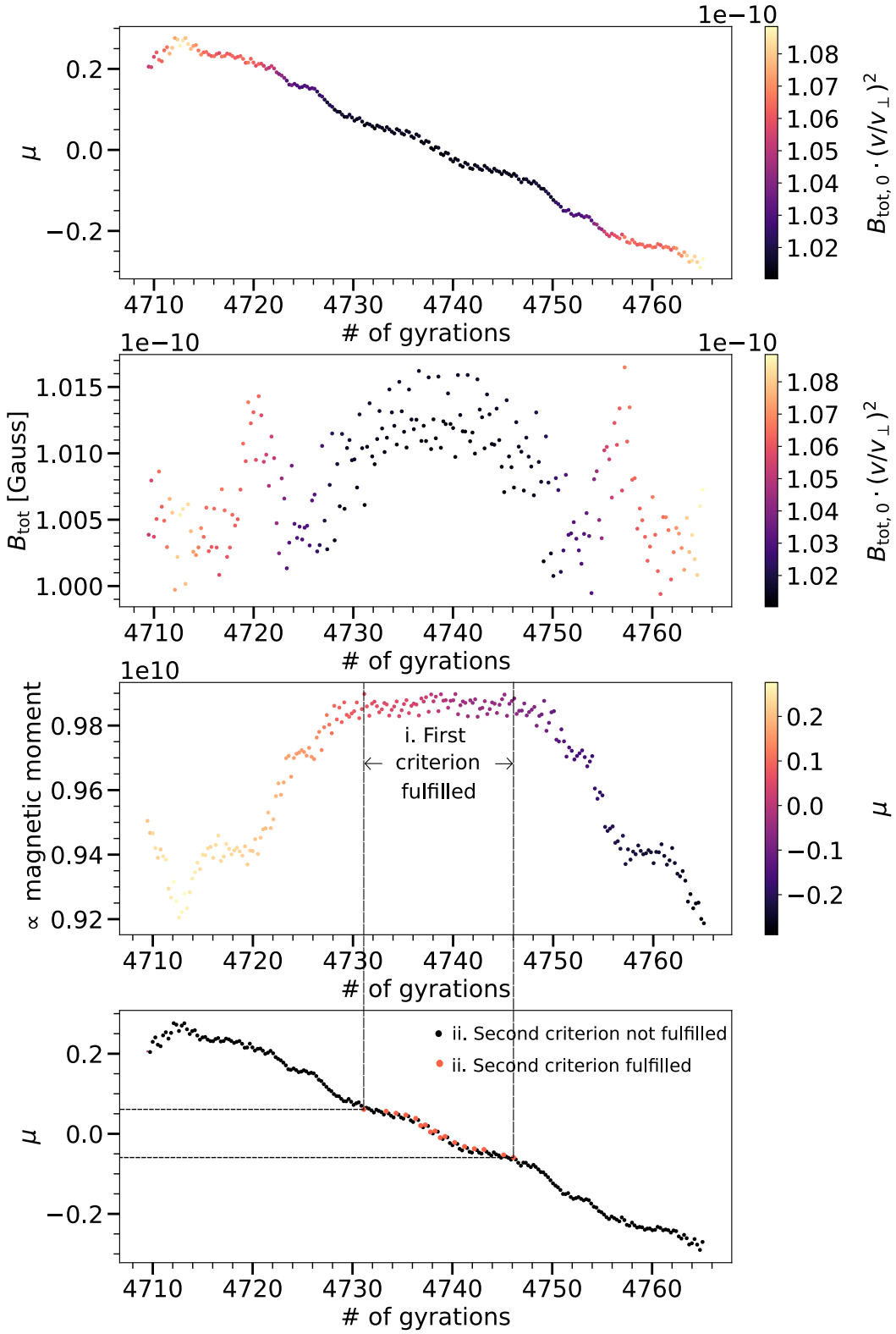

Figure 3.15: The value of the right side term of the inequality (3.15) is depicted in the upper two subplots. The third subplot presents the magnetic moment as a function of the number of gyrations. The last subplot summarizes the first two subplots. It indicates if the inequality (3.15) is fulfilled. Criterion (3.15) is fulfilled as long as the magnetic moment is constant. Simulated with $R_g = 0.109$ pc, $b/B = 0.01$ and $l_{low} = 0.04$ pc.

indicates the particles with a ratio of R_g/l_{corr} and a certain $|\mu|$, which can scatter up to $|\mu| = 1$. The area with the wave pattern indicates all particles that can scatter down to $\mu \approx 0.06$ based on the discussion above, which resulted in the condition (3.16). This condition is presented with the green horizontal line. Simulation results for the parallel diffusion coefficients are presented in the upper panel as functions of the ratio R_g/l_{corr}. The findings are significant in at least two major respects: First, at a ratio of R_g/l_{corr} slightly lower or approximately to $5/(2\pi)$, the gyroresonance condition is satisfied for the largest range of the pitch angle cosine, which corresponds to the least missing resonant interactions of the particles. Second, decreasing the ratio R_g/l_{corr} increases missing resonant scatterings, which artificially pollutes the diffusion coefficients such that γ artificially decreases from the dependency $\kappa_{\parallel} \propto E^{\gamma}$. Consequently, fitting to diffusion coefficients at ratios of R_g/l_{corr} slightly smaller or equal than $5/(2\pi)$ is crucial for determining the correct energy dependency of the diffusion coefficients. This discussion is applied to data from [15] in Fig. 3.16. The border between the mirror and the diffusive-energy regime cannot be determined because of missing information. As discussed above, the simulation results around $R_g/l_{corr} \approx 5/(2\pi)$ are polluted the least and therefore have to be considered for determining the slopes as presented in the right panel of Fig. 3.16. Consequently, each fit starts with the ratio shown on the x-axis in the right panel and ends at the value closest to the upper border, while taking all values in between into account. A slope of 1/3, which is claimed in their publications, can only be concluded by accounting for data points that are calculated for particles, that cannot scatter resonantly anymore around $\mu \approx 0$. Further examples are presented in Appendix M with similar results.

4. **Ballistic-Energy Regime** ($|\mu_{high}| < 1$): Particles still scatter which satisfy $|\mu| < |\mu_{high}| < 1$. Particles with $|\mu_{high}| < |\mu| < 1$, cannot interact anymore with the fluctuations and thus cannot change their direction in scattering interactions. The result is an increased diffusion coefficient. This behavior is visible in Fig. 3.14 and Fig. 3.17.

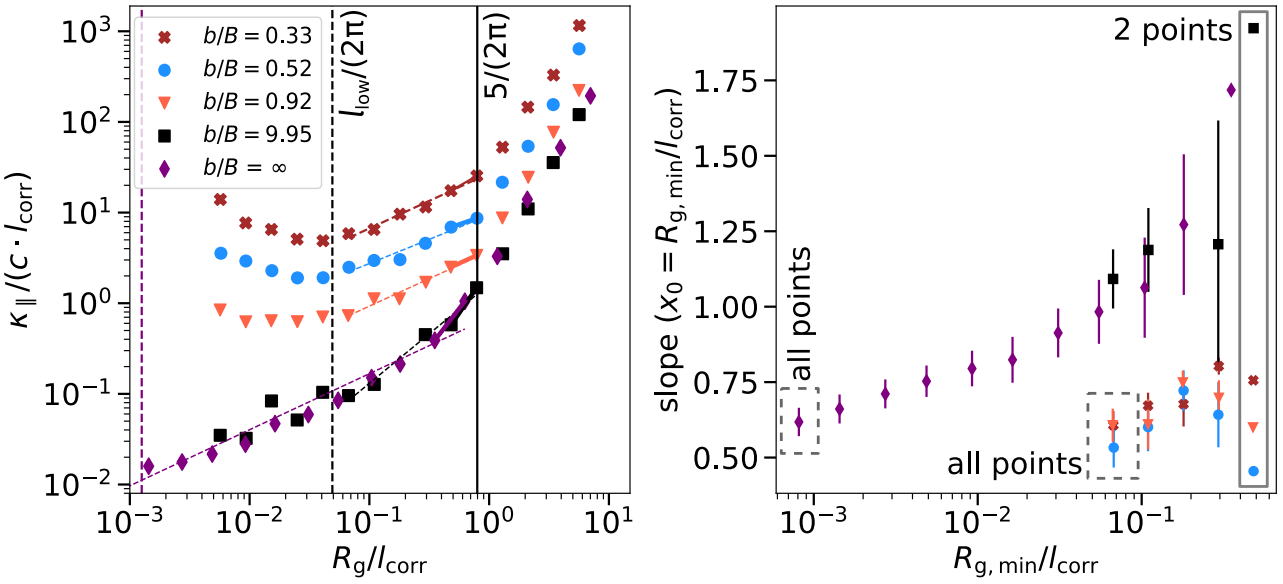

Figure 3.16: *Left panel*: Analysis of resonant scattering regime based on the analysis resulting in Equ. (3.13) applied on data taken from [15]. The black line represents the upper border according to Equ. (3.18). The lower boundaries are indicated by the dashed lines according to Equ. (3.14). *Right panel*: The slopes of the fits within the diffusion-energy regime are presented. Each fit starts with the ratio shown on the x-axis and ends at the value closest to the upper border at $2/(5\pi)$, while taking all values in between into account.

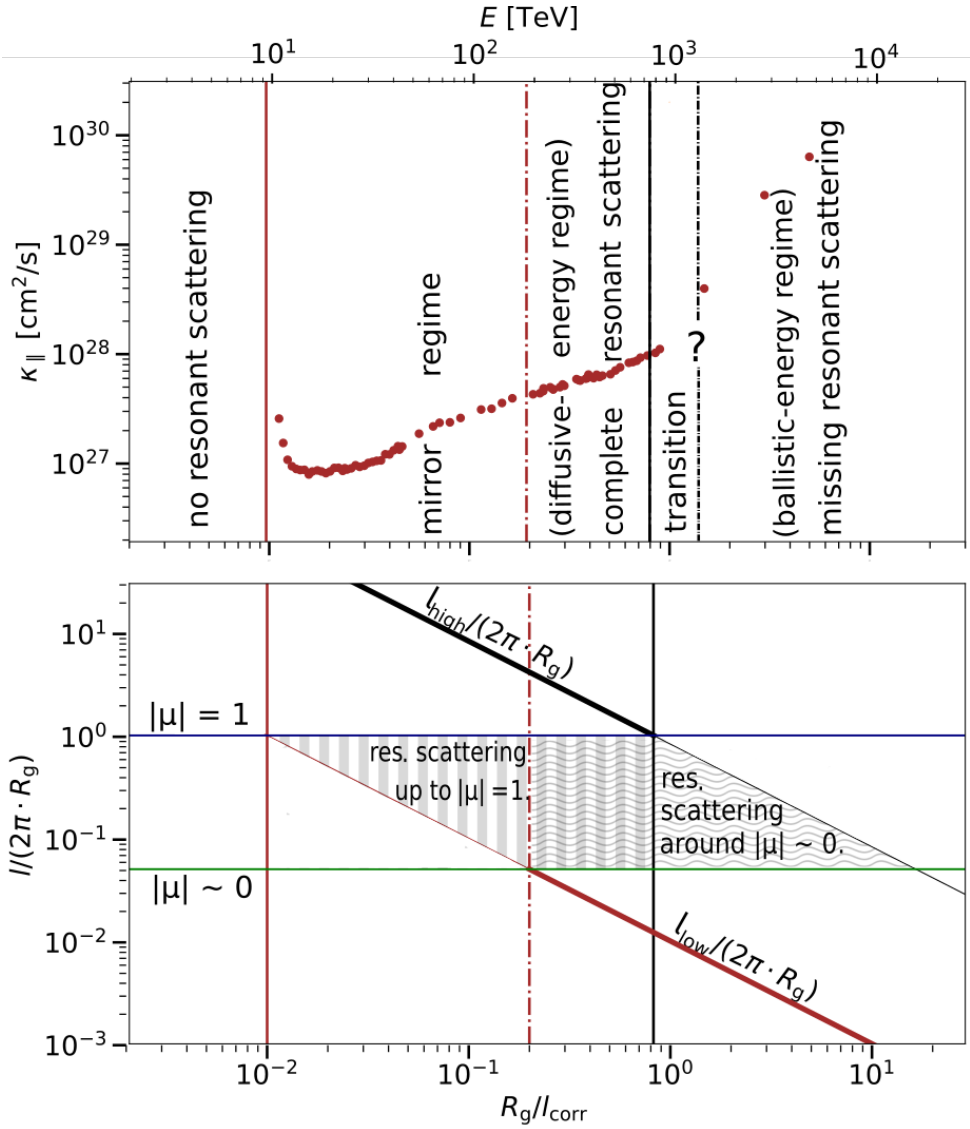

Figure 3.17: *Upper panel*: Parallel diffusion coefficients as functions of the ratio R_g/l_{corr} for $l_{low} = 1$ pc, $l_{high} = 82.45$ pc. The different regimes are calculated with the equations provided in the text as shown in the lower panel. *Lower panel*: Illustration of Equ. (3.13). In order to scatter resonantly around $|\mu| \approx 0$, the right hand side of the gyroresonance condition (3.12) has to be smaller than 0.06 according to Equ. (3.16) (approximated for $b \ll B = 1$).

Table 3.3: Summary of the definitions and ranges of the discussed regimes in this Section and Section 2.3. Figure 3.17 illustrates these definitions. χ is not yet precisely defined, but is $\gg 1$, because of $R_g \gg l_{corr}$.

Regime	$l_{low}/(2\pi R_g)$	$l_{high}/(2\pi R_g)$	R_g/l_{corr}	Equ.
Missing res. scattering	> 1	≥ 1	$0 - l_{low}/(2\pi l_{corr})$	(3.14)
Mirror regime	> 0 & ≤ 1	≥ 1	$l_{low}/(2\pi l_{corr}) - l_{low}/(2\pi l_{corr}\xi)$	(3.14) & (3.17)
Resonant scattering	≈ 0	≥ 1	$l_{low}/(2\pi l_{corr}\xi) - 5/(2\pi)$	(3.17) & (3.18)
Intermediate-energy	≈ 0	< 1	$5/(2\pi) - \chi$	(3.18)
High-energy	≈ 0	$\ll 1$	$\chi - \infty$	–

The simulation parameters that determine the range of μ are listed below.

- **Smallest Plasma Wavelength**: The smallest plasma wavelength directly influences the lower boundary of $|\mu|$ only. It does, however, indirectly influence the upper limit since l_{high} is related to l_{low} according to Equ. (3.2): $l_{\text{high}} \leq N_{\text{grid}} l_{\text{low}}/4$. Figure 3.14 illustrates the influence of l_{low}.
- **Largest Plasma Wavelength**: The smallest plasma wavelength l_{high} directly influences the upper boundary of $|\mu|$, given that the upper boundary is defined as $R_{\text{g}}/(l_{\text{corr}}) = 5/(2\pi)$ and therefore results in $R_{\text{g}} = l_{\text{high}}/(2\pi)$ of the upper border.
- **Number of Grid Points**: According to Equ. (3.2), the number of grid points determines the possible range of $|\mu|$ for which particles interact resonantly with the magnetic fluctuations.
- **Energy of Particle**: The energy of the particle just shifts the range of $|\mu|$. This can be seen by the definition of the energy in Equ. (3.5) $E \propto R_{\text{g}} \cdot (\sqrt{b^2 + B^2} cq)$ and the gyroresonance condition in Equ. (3.12) $\mu = l/(2\pi R_{\text{g}})$. It has no influence on the extend of the range.
- **Magnitude of Magnetic Field**: The effect of the magnetic field magnitude is similar to the effect of the particle energy. As for the particle energy, this parameter is only able to shift the range of $|\mu|$. This can be also seen by the definition of the gyroradius in Equ. (3.5) and the gyroresonance condition in Equ. (3.12).

3.3.3 Power Spectrum of Turbulence

After defining the diffusion regime based on the possible range of resonant interactions in Section 3.3.2, the effect of the power spectrum of the turbulence will be presented. According to the previous analysis of the scatter processes, the missing interactions dominate in the intermediate- and high-energy regime, such that the influence of the spectral index of the turbulence vanishes in those two regimes. This is also in agreement with the energy dependence of the diffusion coefficient in the intermediate-energy and high-energy regime as presented in Equ. (2.49) and Equ. (2.54) respectively, which are both independent of the spectral index, while Equ. (2.32) for the diffusive regime depends on the spectral index. Consequently, the following first four parameters determine the energy regime and thus lead to either an effect or no effect at all, while the last parameter quantifies the possible influence. The following four parameters determine the regime as already discussed in Section 3.3.2, and are therefore just listed for completeness without further discussion: **Energy of particle**, **magnitude of background field**, **largest plasma wavelength** and **smallest plasma wavelength**. In addition, the following parameter influences the power spectrum of turbulence:

- **Turbulent Spectral Index**: The exact dependency is stated in Equ. (2.32). This dependency can, however, be understood intuitively. For the case of physically reasonable negative spectral indexes $\alpha < 0$, there is more energy in the long turbulence wavelengths than in the short turbulence wavelengths as presented in Fig. 3.2. The key argument is, that by increasing the particle energy, the range of plasma wavelengths, with which the particle could resonantly scatter, shifts to higher values, as described in Equ. (3.12) and illustrated in the lower panel of Fig. 3.9. As a result, the particle interacts with higher energetic plasma waves, which decreases the growth of the diffusion in comparison to an index of $\alpha = 0$.

3.3.4 Magnetic Field Magnitude

The previous Chapters reveal that the ratio of b/B influences the diffusion coefficient, most notably the theory derived in Chapter 2 is based on small b with respect to B. The key argument of studying this limit is the fact that it best fulfills the approximation of gyromotion of the particles. In this limit, the dependencies are either $(b/B)^2$ for the parallel diffusion coefficient or $(b/B)^{-2}$ for the perpendicular diffusion coefficient. Even though, the same influence of this ratio is predicted from the theory in all regimes, the coincidence from those predictions with the simulation results may vary due to the

different assumptions used for their derivation, such that this physical influence, can best be treated in those three different regimes: the diffusion regime, the intermediate-energy regime and the high-energy regime. Intuitive arguments for the influence of those two simulation parameters are given below, even though an individual treatment of those two parameters is difficult – they can be best understood in relation to each other:

- **Magnitude of Turbulent Field**: In the limit of a strong turbulent magnetic field magnitude, the parallel and the perpendicular diffusion coefficient coincide. Consequently, the turbulent magnetic field obfuscates the effect of the background magnetic field.
- **Magnitude of Background Field**: The classification between the perpendicular and the parallel component is based on the background magnetic field. The simple reasoning, that a weak background magnetic field (in comparison with the turbulent magnetic field) results in coincident components of the diffusion coefficient together with a differentiation of the components as soon as the background magnetic field dominates, is in agreement with the derived $(b/B)^2$ and $(b/B)^{-2}$ dependencies for the parallel and the perpendicular diffusion coefficient respectively.

The isolated treatment of those two simulation parameters is limited since they depend on each other and can therefore just be analyzed relatively to each other. Consequently, only the ratio b/B is relevant.

3.3.5 Influence of the Ratio of Gyroradius and Correlation Length

Similarly to the influence of magnetic field magnitudes, the diffusion coefficient dependencies on the ratio of $R_\mathrm{g}/l_\mathrm{corr}$ can best be studied in the three aforementioned regimes. There are two types of effect which result in a change of the diffusion coefficient when the ratio of $R_\mathrm{g}/l_\mathrm{corr}$ is varied: on one hand, this ratio determines the regime – either, the diffusive regime, the intermediate-energy regime or the high-energy regime – and thus the exact dependency from the diffusion coefficient from $R_\mathrm{g}/l_\mathrm{corr}$; on the other hand, theoretical derivations in Chapter 2, however, predict in each regime an increase of the diffusion coefficient with an increase of the ratio $R_\mathrm{g}/l_\mathrm{corr}$. Before discussing the coincidence of theoretical predictions with simulation results in Chapters 4 and 5, the key simulation parameters involved in the ratio of $R_\mathrm{g}/l_\mathrm{corr}$ are listed as follows:

- **Energy of Particle**: Increasing the energy results in an increased gyroradius and thus may prevent resonant scattering processes with the turbulence (see Section 3.3.2 for details). Consequently, the particles can diffuse more efficiently. In addition, a higher energy of the particle is related to a higher speed, which also suggests a faster diffusion. Those two effects result in an increased diffusion coefficient.
- **Magnitude of Background Field**: The main influence of the background magnetic field in this context is its relation to the gyroradius as described in Equ. (2.46).
- **Largest Plasma Wavelength**: This influence is described in Equ. (3.7). Varying l_high is therefore inversely proportional to the ratio of $R_\mathrm{g}/l_\mathrm{corr}$. Increasing l_high results in decreasing the diffusion coefficient.

3.4 Chapter Summary

Returning to the concern posed at the beginning of this Chapter regarding the multilayered and highly entangled dependencies of the simulation parameters on the diffusion coefficient, it is now possible to state that the numerical artifacts can be resolved such that the physical dependencies are revealed. A summary of the main findings and of the principal issues and suggestions which have arisen in

the study of minimizing numerical influence during the calculation of the diffusion coefficients can be listed as follows:

- **Reaching the Plateau – Convergence of the Running Diffusion Coefficient**:
  1. **Number of Particles**: Increasing the number of particles decreases the uncertainties as presented in Section 3.2.1.
  2. **Chaotic Character**: Section 3.2.3 discusses the requirements for a chaotic vector field and concludes that they are fulfilled for the partially ordered magnetic field used in this thesis.
- **Convergence of the Diffusion Coefficient**
  1. **Box Size**: Instead of investigating the number of grid points and their spacing in between independently, the results in Section 3.5 conclude, that the box size presents a parameter combination from which the diffusion coefficient has a real functional dependence and the influence can thus be minimized by using convergence tests.
  2. **Stepsize**: A comparison of the two integration routines presented in Section 3.2.4, concludes, that the Boris push provides a faster method for advancing charged particles within a magnetic field for a sufficient precision. Another important finding was the relation between the stepsize and the gyroradius, stating that the stepsize should be not larger than the gyroradius.
  3. **Interpolation**: The effective spectral index of the turbulent power spectrum decreases for decreasing plasma wavelengths as shown in Fig. 3.8.

After solving those challenges, the underlying physical properties of the diffusion coefficient were exploited and summarized below.

- **Regimes in Time Domain**: The investigation of the running diffusion coefficient has justified the classification of two different regimes in the time domain – namely, the weakly perturbed propagation regime and the diffusive propagation regime. The requirements for reaching the latter regime were also discussed in Section 3.3.1.
- **Regimes in Energy Domain**: One of the most significant findings of this thesis, which emerged from analyzing the scatter processes and their restrictions presented in Equ. (3.13). In addition to calculating the upper border of the diffusive regime to be at $R_\mathrm{g}/l_\mathrm{corr}$, unexpected mirror effects were observed and studied. The idea arose to repair the diffusion coefficient so as to account for both gyroresonant scattering and mirroring. As a further consequence, this study delivered a lower boundary for the diffusive regime stated in Equ. (3.14) and Equ. (3.17).
- **Power Spectrum of Turbulence**: In the diffusion regime, the exact dependency is stated in Equ. (2.32). The spectral index of the turbulence energy spectrum, however, has no influence due to the dominant effect of missing interactions.
- **Magnetic Field Magnitude**: The parallel and perpendicular diffusion coefficients are proportional to $(b/B)^2$ and $(b/B)^{-2}$ respectively, the detailed discussion is, however, provided in the next Chapters for the different energy regimes. The background field influences the classification into the different energy regimes. The magnitude of the turbulence with respect to the background field is, on the other hand, important for the comparison with theoretical predictions, because they are just valid in the limit $b/B \ll 1$.
- **Influence of the Ratio of Gyroradius and Correlation Length**: Increasing the particle energy leads to an increased gyroradius, which may prevent resonant scatter processes of particles with $|\mu| \approx 1$. In addition, a higher energy is related to a higher velocity. Both effects result in an increased diffusion coefficient. The coincidence of the simulation results will be discussed in detail for each energy regime in the following Chapters.

4 | Calculation of Diffusion Coefficients in the Different Energy Regimes

After having summarized the physical influences of the diffusion coefficient in the previous Chapter, the present Chapter provides a comparison of the simulation data with the theoretical predictions for the diffusion coefficient dependencies from Chapter 2. Proving the theoretically predicted dependencies of the diffusion coefficient, especially the spectral index γ of the energy dependency $\kappa \propto E^{\gamma}$, opens up vast physical implications. This Chapter aims at testing theoretical predictions against simulated data. As an example, the results are applied to cosmic ray propagation in radio galaxies in Appendix A. First, the relevant predictions from Chapter 2 are summarized briefly in table 4.1.

Table 4.1: Summary of the theoretically predicted parallel diffusion coefficient dependencies as derived in Chapter 2. The diffusive regime, the intermediate-energy regime and the high-energy regime are presented in Sections 2.2, 2.3.1 and 2.3.2, respectively. In addition, the definitions and ranges of the regimes according to the Sections 2.3 and 3.3.2. Figure 3.17 illustrates these definitions. χ is not yet precisely defined, but yields approximately $\gg 1$, because of $R_{\mathrm{g}} \gg l_{\mathrm{corr}}$ (see the more extensive discussion in Chapter 2).

Regime	Range in R_{g}	Theoretical prediction: $\kappa_{\parallel} \propto$	Equ.
Missing res. scatt.	$0 - \frac{l_{\mathrm{low}}}{2\pi l_{\mathrm{corr}}}$	–	–
Mirror regime	$\frac{l_{\mathrm{low}}}{2\pi l_{\mathrm{corr}}} - \frac{l_{\mathrm{low}}}{2\pi l_{\mathrm{corr}}\xi}$	–	–
Diffusive-energy	$\frac{l_{\mathrm{low}}}{2\pi l_{\mathrm{corr}}\xi} - 5/(2\pi)$	$\left(\frac{B}{b}\right)^2 \left(\frac{E(cl_{\mathrm{corr}})^2}{qB}\right)^{1/3} \propto \left(\frac{B}{b}\right)^2 \left(\frac{R_{\mathrm{g}}}{l_{\mathrm{corr}}}\right)^{1/3} c\, l_{\mathrm{corr}}$ [65, 70]	(2.32)
Intermediate-energy	$5/(2\pi) - \chi$	$\propto \frac{1}{b^2}\frac{E^2}{q^2 c l_{\mathrm{corr}}} \propto \left(\frac{B}{b}\right)^2 \left(\frac{R_{\mathrm{g}}}{l_{\mathrm{corr}}}\right)^2 c\, l_{\mathrm{corr}}$	(2.49)
High-energy	$\chi - \infty$	$\propto \frac{B}{b^2}\frac{E}{q} \propto \left(\frac{B}{b}\right)^2 c\, R_{\mathrm{g}}$	(2.54)

One of the limitations of the theoretical predictions for the diffusion coefficient dependencies is that they were derived for the limit $b \ll B$. In addition to investigating the agreement of the predictions stated in table 4.1 with simulated data for $b \ll B$, this Chapter addresses the question for which ratios of b/B the theoretical predictions are still applicable within sufficient accuracy. To investigate this question, it is necessary to discuss the definition of the gyroradius first. Table 3.1 indicates the two different definitions: either

$$R_{\mathrm{g}} = E/(Bqc) \tag{4.1}$$

or $R_{\mathrm{g}} = E/(\sqrt{b^2 + B^2}qc)$. The former definition is used for the following simulation results because it coincides for ratios of $b/B \lesssim 1$ with the definition presented in Section 2.3 in Equ. (2.46) $R_{\mathrm{g}} = E/(B_{\mathrm{tot}}qc)$, with $B_{\mathrm{tot}} = \frac{1}{2\pi}\int_0^{2\pi} \mathrm{d}\phi\ \frac{1}{\pi}\int_0^{\pi} \mathrm{d}\theta\ |B + b \cdot \cos(\phi) \cdot \cos(\theta)|$. In Appendix F it is presented

that $B_{\mathrm{tot}} \approx B$ and the parallel magnetic field magnitude $B_{\mathrm{tot},3}$ dominates the perpendicular field magnitude $B_{\mathrm{tot},1}$ for $b/B \lesssim 2$. Consequently, the definition of the gyroradius presented in Equ. (2.46) can be approximated with the definition in Equ. (4.1) for $b/B \lesssim 2$. In the following, fits are only applied up to ratios of $b/B \lesssim 2$ so that the theory is approximately based on the same definition of the gyroradius as which is used for displaying the simulation results.
Before proceeding to examine the simulation results for the different energy regimes, it is useful to briefly discuss the complete energy range and the whole range of b/B.

4.1 Overview

In order to investigate the diffusion coefficient dependencies within each regime, a large number of particles was injected in each simulation (between 30,000 for the resonant-scattering regime and 50,000 for the other regimes). This large statistical base is necessary because the intermediate-energy regime covers less than a magnitude of the ratio $R_{\mathrm{g}}/l_{\mathrm{corr}}$, and thus small uncertainties for the individual diffusion coefficients are essential for determining the dependencies. The findings from Chapter 3 were used to minimize the numerical artifacts. An overview of the perpendicular and parallel diffusion coefficients is presented in Fig. 4.2 and 4.1, respectively.

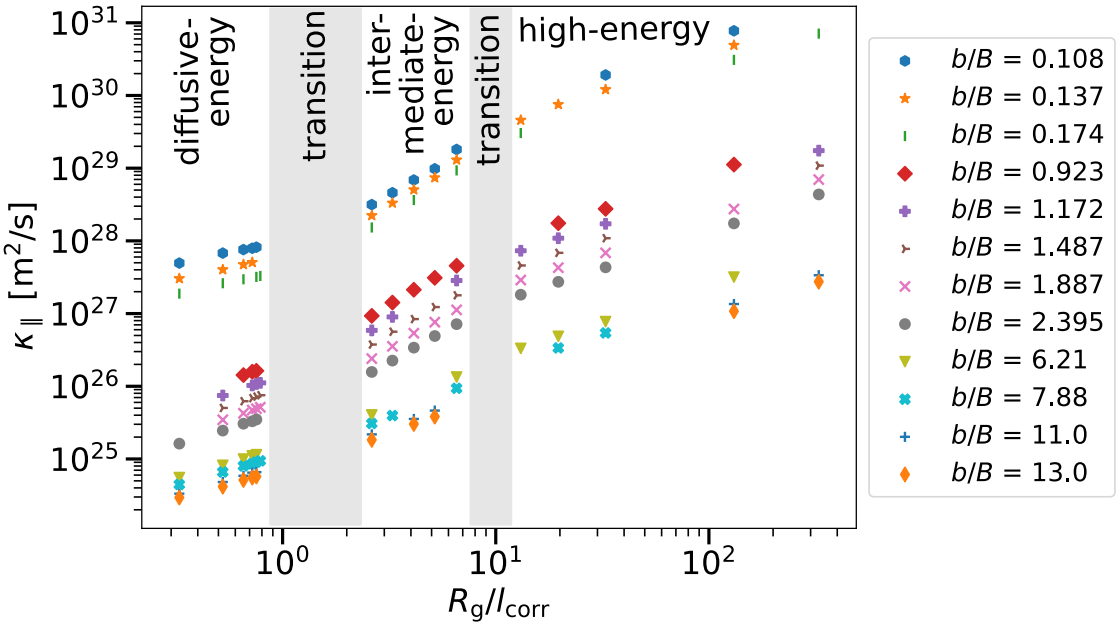

Figure 4.1: Parallel diffusion coefficients as functions of the ratio $R_{\mathrm{g}}/l_{\mathrm{corr}}$. Three different regimes are indicated and discussed in Sections 4.2, 4.3 and 4.4 and listed in table 4.1.

Overall, 170 diffusion coefficient were calculated, where each simulation took more than 1000 CPU hours for $b/B > 1$ and more than 2000 CPU hours for small ratios of $b/B < 1$ to guarantee a statistically converged diffusion coefficient with a sufficient accuracy. In the following plots, the statistical uncertainties are shown but are not visible due to their small values. For each of the 16 simulated energies, 30 different ratios of b/B were used. There are two reasons for the fact that only 170 diffusion coefficients were calculated in those 480 simulations: either the plateau was not reached or the simulation was canceled. The latter case was either caused by the hot weather leading to several shutdowns of the server or by the cancellation due to a higher ranked job on the server. Simulation results are only considered if the simulations finish without problems or cancellations. Further simulation parameters are: $l_{\mathrm{low}} = 1.7$ pc, $l_{\mathrm{high}} = 82.45$ pc, $s_{\mathrm{spacing}} = 0.17$ pc, $N_{\mathrm{grid}} = 1024$. There were chosen after convergence testing each parameter as discussed in Chapter 3. The mean-displacement method

was used for all diffusion coefficients. The TKG-method is not applicable for the perpendicular component as the gyrations in the perpendicular plane (with respect to the background field) pollute the time-averaging in the TGK-method.

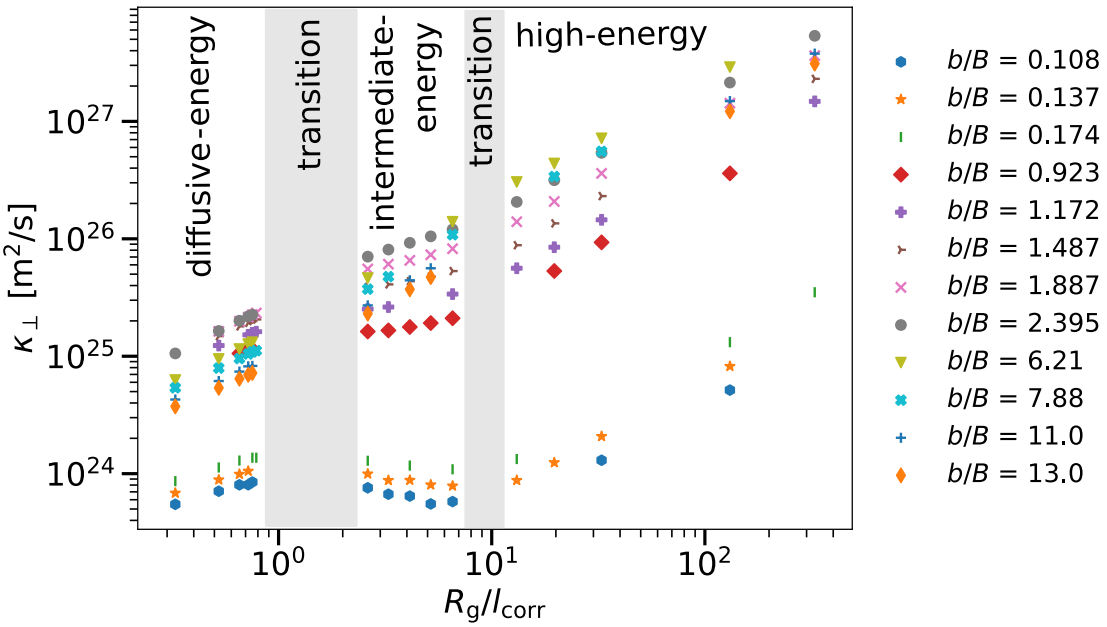

Figure 4.2: Perpendicular diffusion coefficients as functions of the ratio R_g/l_{corr}. Three different regimes are indicated and discussed in Sections 4.2, 4.3 and 4.4 and listed in table 4.1.

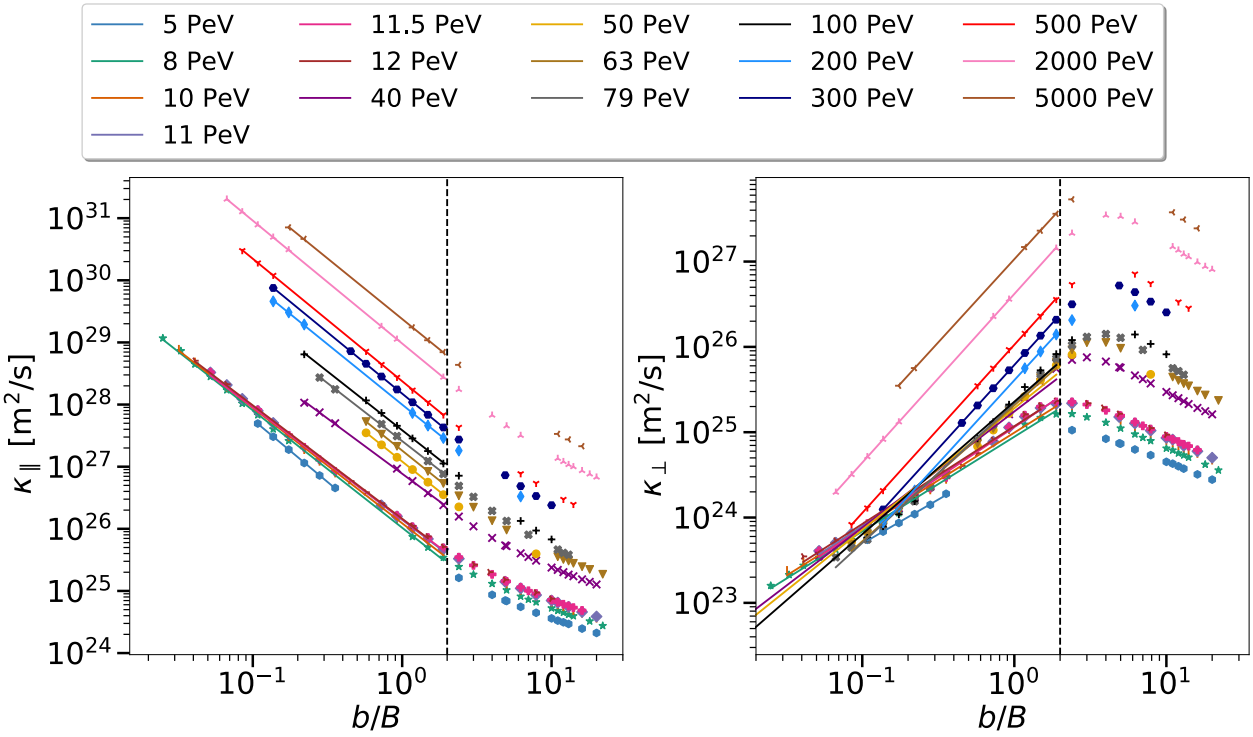

Figure 4.3: Parallel diffusion coefficients (*left panel*) as well as perpendicular diffusion coefficients (*right panel*) as functions of the ratio b/B. The theoretical predictions for the influence of the ratio b/B on the parallel diffusion coefficient is derived in Chapter 2 and summarized in table 4.1. A linear regression is presented in the linear domain of b/B which yields approximately $0 < b/B < 2$.

Turning now to the influence of the magnetic field configuration, the data can also be used to show the influence of the ratio b/B on the diffusion coefficients. The parallel (*left panel*) and perpendicular (*right panel*) components are presented as functions of b/B in Fig. 4.3. According to the theoretical predictions for $b \ll B$ presented in table 4.1, a power-law dependency between the parallel diffusion coefficient and the ratio b/B is expected. This motivates linear fits in the log-log plots shown in Fig. 4.3. The calculated slopes together with their standard derivations are presented in table L.1 and plotted as a function of the ratio b/B in Fig. 4.4. Those two figures indicate that the predicted b/B dependency of the parallel diffusion coefficient is applicable even for ratios of b/B up to 2 as expected based on the discussion in Appendix F. The perpendicular diffusion coefficient displays a scaling with b/B opposite to the parallel component for the ballistic regime. For the diffusive regime, the dependency is not captured by a linear scaling, a more complex behavior is revealed instead. This Chapter focuses on the parallel diffusion coefficient, which subsequently is connected to the perpendicular diffusion coefficient in Chapter 5. In addition to the extended range of validity of the power-law description, the simulation data reveal agreement between the theoretically predicted power-law index of -2 for $\kappa_{\parallel}(b/B)$ with that of the simulation results, which is summarized in Fig. 4.4. This finding is in agreement with the discussion presented in the Section 2.3 as well as in Appendix F in which it was already concluded, that the derivations may be applicable up to ratios of $b/B \approx 2$ at least for the intermediate-energy and the high-energy regimes. For higher ratios of b/B, the function of $\kappa_{\parallel}$ is flatter. The ratio of $\kappa_{\perp}/\kappa_{\parallel}$ in dependence of b/B is presented in Fig. 4.5. The linear behavior in the log-log scale holds from the lowest values up to approximately $b/B \approx 2$. The slopes of the presented fits converge toward the value 4 for increasing energies as presented in the left panel of Fig. 4.5. For higher ranges b/B, the ratio of $\kappa_{\perp}/\kappa_{\parallel}$ remains constant. The reason for this constant ratio is the fact that the difference between the parallel and the perpendicular component vanishes as described in Appendix F. This was already indicated in Fig. 4.4.

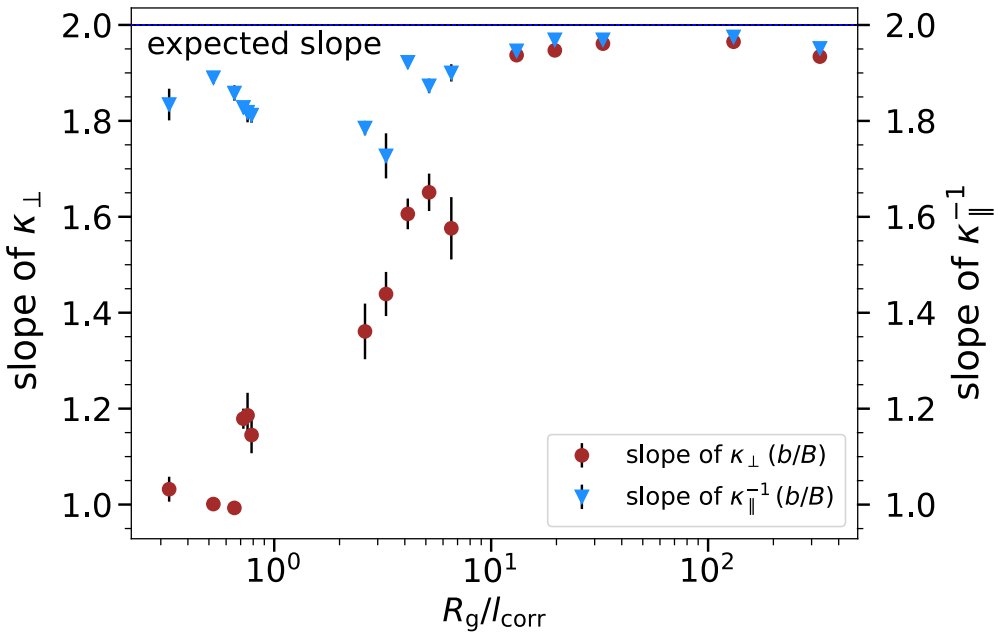

Figure 4.4: Summary of the slopes fitted to the simulated perpendicular and inverse parallel diffusion coefficient in the linear regime of b/B in Fig. 4.3. Table L.1 presents the slopes of the fits. The theoretical prediction for the parallel component is 2.

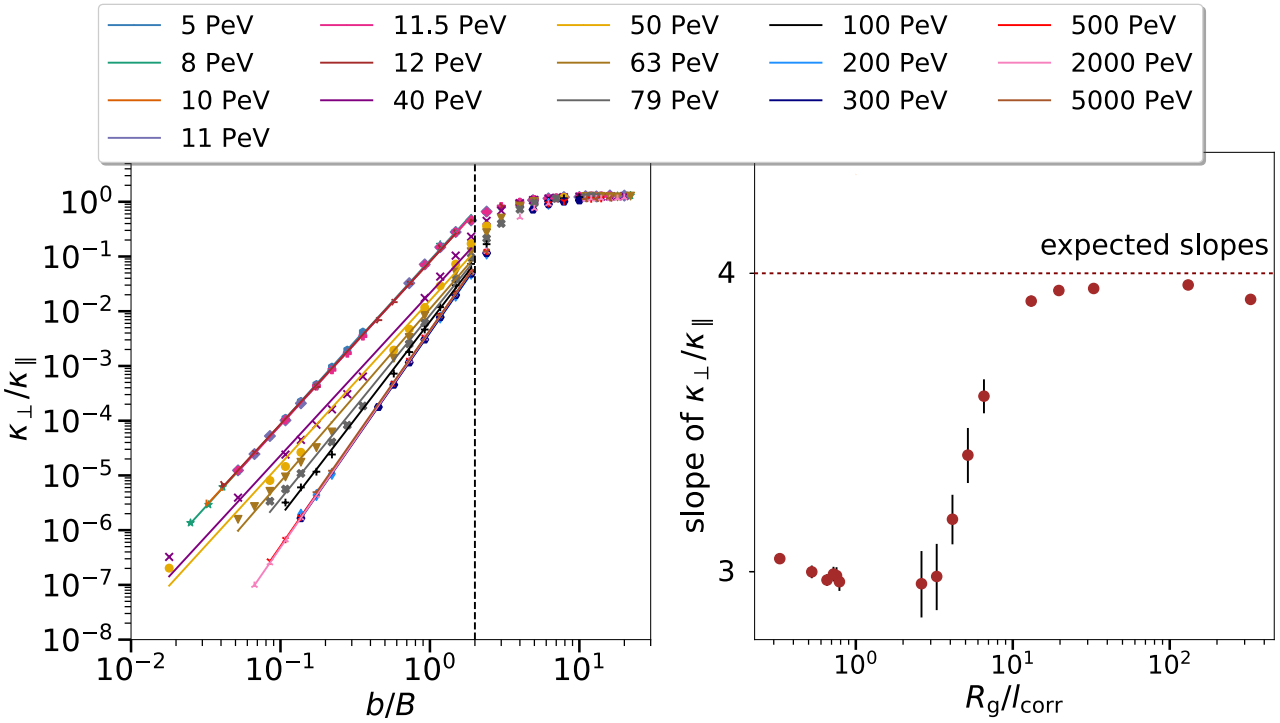

Figure 4.5: Ratio $\kappa_\perp/\kappa_\parallel$ as functions of the ratio b/B. A fit is presented in the linear regime of b/B. The data is shown in both plots in a log-log representation. Table L.1 presents the ranges of b/B for which the data are fitted together with their slopes. The slopes fitted to the ratio $\kappa_\perp/\kappa_\parallel$ in the linear domain of b/B on the left side are presented in the right plot as a function of the ratio R_g/l_{corr}.

4.2 Diffusive-Energy Regime

The simulated diffusion coefficients in the diffusive-energy regime are presented in Fig. 4.6 as functions of the ratio R_g/l_{corr}. Different ratios of b/B are presented as long as at least three simulation results are available in this energy regime. Figure 4.6 investigates if the simulations are consistent with the predictions from QLT. For the range $0.052 \leq b/B \leq 20$, the energy range 8 PeV $\leq E \leq$ 11.5 PeV, corresponding to $0.33 \leq R_g/l_{corr} \leq 0.76$, is investigated (see table L.2 for details). The considered range is within the theoretically predicted diffusive-energy range $l_{low}/(2\pi l_{corr}\xi) \leq R_g/l_{corr} \leq 5/(2\pi)$, which is based on the discussion in Section 3.3.2 and summarized in table 4.1. Data points are fitted with a linear fit in the log-log representation. With increasing ratio R_g/l_{corr}, the diffusion coefficients increase. The fits are presented in table L.2 and shown as a function of the ratio b/B in Fig. 4.11 for $\kappa_\parallel$ (left side) and for $\kappa_\perp$ (right side). In the limit $b \ll B$, the theoretical prediction for $\kappa_\parallel$ (see table 4.1) predicts a slope of 1/3 for the energy behavior in the diffusive-energy regime. In order to further resolve the energy dependency of $\kappa_\parallel$, Fig. 4.7 presents more simulated data in the diffusive-energy regime. Due to the large computation time of each $\kappa_\parallel$, only the ratio of $b/B = 0.1$ is investigated. The difference between the fitted slope 0.513 ± 0.030 in Fig. 4.6 and the slope 0.438 ± 0.021 in Fig. 4.7 is caused by the effect of the interpolation routine of the magnetic field as discussed in detail in Section 3.2.5. The relevant conclusion can be summarized as follows: The interpolation routine artificially pollutes the magnetic energy spectrum such that the slopes decrease for small fluctuation wavelengths. This fact was considered in generating Fig. 4.7, because only the highest possible energy range of particles was taken into account. The upper energy bound is given by Equ. (3.18). Figure 4.6, on the other hand, takes a larger range of particle energies into account and thus demonstrates the power-law behavior over a larger range. According to Equ. (2.32), the diffusion coefficient dependence on the ratio R_g/l_{corr}

is based on the spectral index α of the turbulence spectrum. Consequently, the polluted spectral index α for the wider low-energy range in Fig. 4.6 results in a further deviation from theoretical predictions that are based on an index $\alpha = 1/3$.

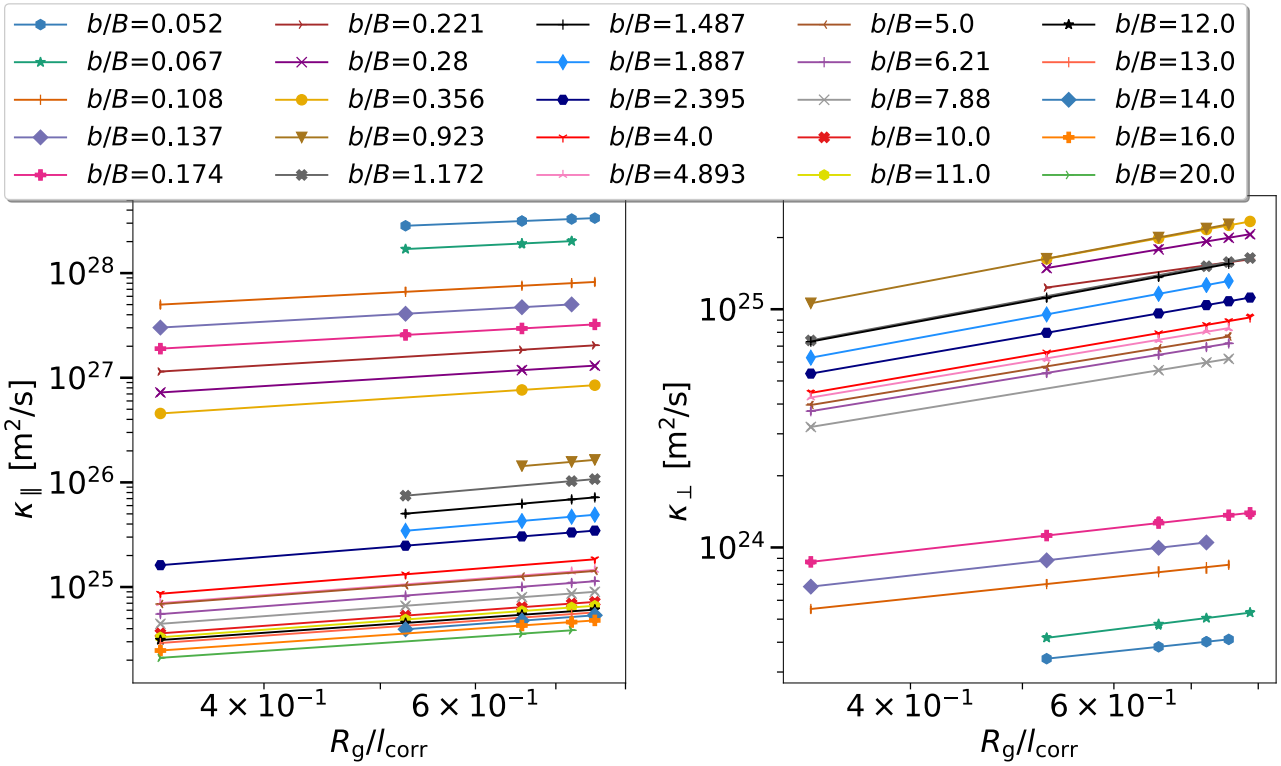

Figure 4.6: Parallel (left) and perpendicular (right) diffusion coefficient as functions of the ratio R_g/l_{corr} in the diffusive regime. Different ratios of b/B are investigated as presented in table L.2. The fitted slopes are also listed in table L.2 and plotted against b/B in Fig 4.11 for $\kappa_\parallel$ and for $\kappa_\perp$.

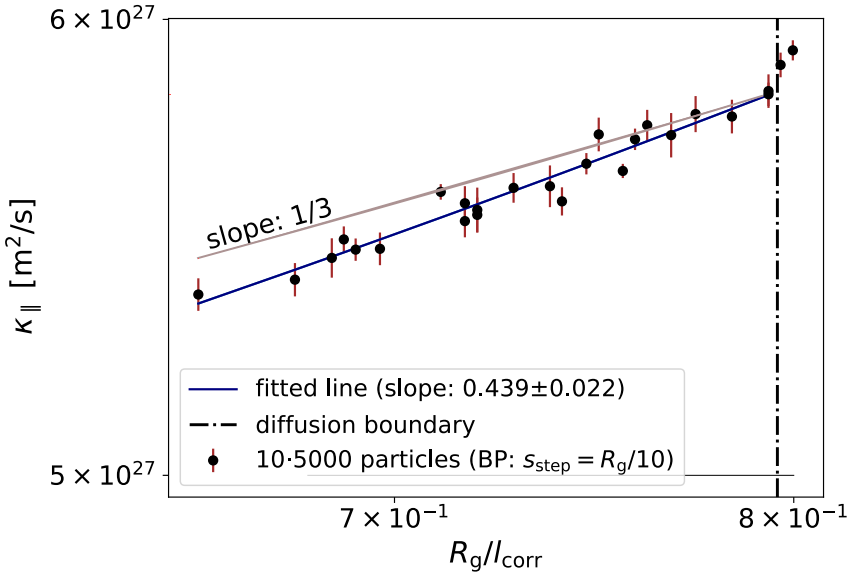

Figure 4.7: Parallel diffusion coefficient as functions of the ratio R_g/l_{corr} in the diffusive regime for $b/B = 0.1$. $\kappa_\parallel \propto (R_g/l_{corr})^{1/3}$ is theoretically predicted for $b \ll B$. The interpolation effect is minimized because it is simulated for the highest range of energies that is possible for protons within the diffusive regime (see Section 3.2.5 for details). Each data point is based on ten simulations with 5000 particles.

At this point, the findings of this thesis motivates for comparison with the literature (see table 3.1). Even though the presented ratios of b/B are still not small enough, a clear trend is visible: decreasing b/B decreases the slope, which may be consistent with a value of 1/3 for infinitesimal b/B. The same trend is also visible in table 3.1 for the corrected energy behavior of $\kappa_\parallel$ in the diffusive-energy regime. The corrected slopes are consistently above 1/3 for all studies. The slope is between 0.49 and 0.78 for $b/B = 0.1$. This is in great agreement with the calculated slope within the present thesis of 0.598 ± 0.025 for $b/B = 0.1$ presented in Fig. 4.11 and table L.2. The slopes increase with increasing ratio b/B. At $b/B \approx 1$, the slopes are around 1 in this thesis. This is steeper than what is calculated for the other studies. The reason for this may be the different definition of the gyroradius for calculating the values in table 3.1 and table L.2. It can be concluded that considering all results, the slopes are much steeper for ratios of b/B between 0.1 and 1 than what is stated in previous studies (see table 3.1), which is in most cases 1/3, regardless of the definition of R_g.
For high ratios of b/B above 2, nothing can be concluded for $\kappa_\parallel$ and $\kappa_\perp$ individually, because the results may be polluted due to the chosen definition of the gyroradius according to Equ. (4.1). Only conclusions are possible where this effect cancels out, e.g. when considering the ratio $\kappa_\perp/\kappa_\parallel$. It is worth noting that the fitted slopes approximately approach equal values for $\kappa_\perp$ and $\kappa_\parallel$ at large ratios b/B, which can be understood intuitively: For the case of a dominating b, the influence of the background field can be neglected, i.e., the magnetic field becomes nearly isotropic. As a consequence, the perpendicular and parallel components coincide.

4.3 Intermediate-Energy Regime

This Section investigates the intermediate-energy regime as indicated in Fig. 4.2 and 4.1 as well as discussed in Section 2.3.1.

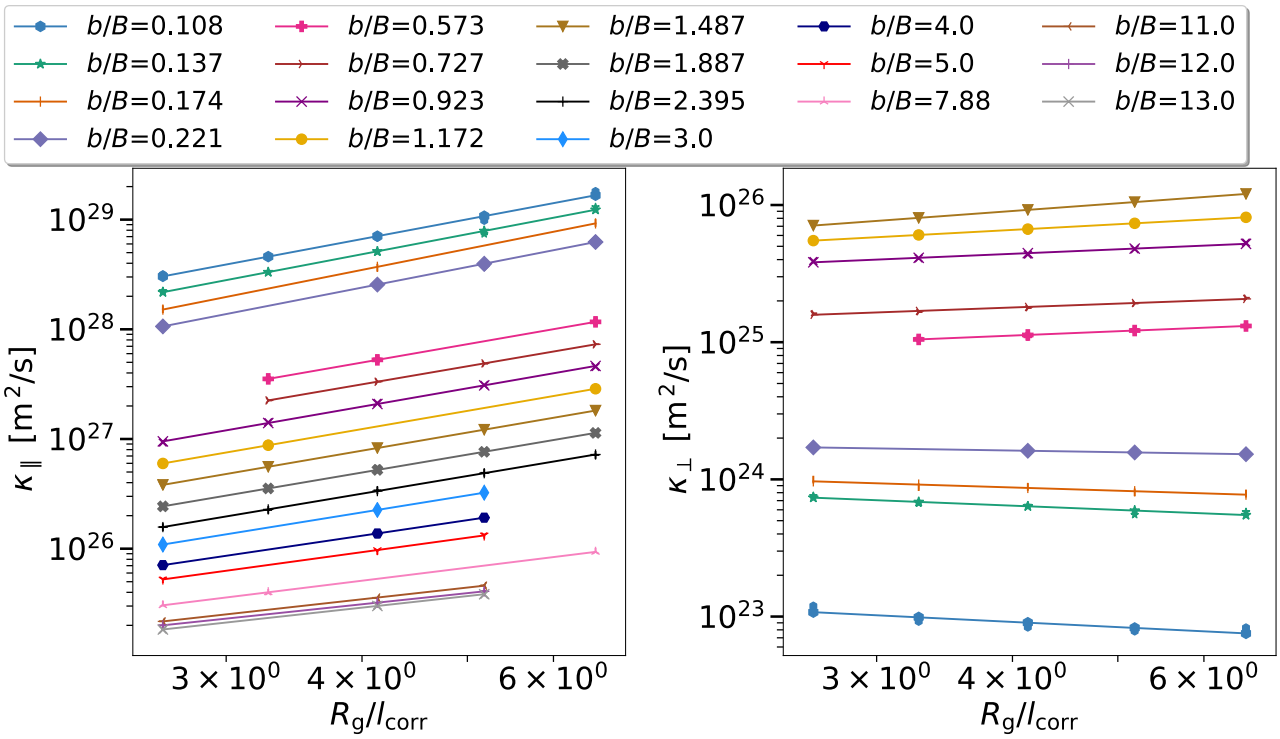

Figure 4.8: Parallel (left) and perpendicular (right) diffusion coefficient as functions of the ratio R_g/l_{corr} in the diffusive regime. Different ratios of b/B are investigated as presented in table L.2. The fitted slopes are listed in table L.2 and plotted against b/B in Fig 4.11 for $\kappa_\parallel$ and for $\kappa_\perp$.

The simulated diffusion coefficients in the intermediate-energy regime are presented in Fig. 4.8 as functions of the ratio R_g/l_{corr}. For the range $0.108 \leq b/B \leq 13$, the energy range 40 PeV $\leq E \leq$ 100 PeV, corresponding to $2.62 \leq R_g/l_{corr} \leq 6.55$, is investigated (see table L.2 for details). Data points are fitted with a linear fit in the log-log representation. With increasing ratio R_g/l_{corr}, all parallel diffusion coefficients increase while the perpendicular components increase for $b/B \gtrsim 0.5$ and decrease otherwise. The fits are presented in table L.2 and are shown as a function of the ratio b/B in Fig. 4.11 for $\kappa_\parallel$ (left side) and for $\kappa_\perp$ (right side). For $b/B \lesssim 2$, the slopes of the linear fits for the parallel diffusion coefficients converge toward 2. The slope of 2 for the parallel diffusion coefficient in the case of $b \ll B$ and energies above the diffusive-energy regime is in agreement with recently published studies [11, 14, 15, 17, 52]. The decrease of the slopes for ratios of b/B larger than 2 can be explained with the discussion presented in the beginning of this Chapter (and in Appendix F) about the definition of the gyroradius. The importance is that the assumption of $B_{tot} \approx B$ is only valid for $b/B \lesssim 2$. There are not enough simulation results in other studies in this energy regime to compare their results for $b > 2$.

4.4 High-Energy Regime

The simulated diffusion coefficients in the high-energy regime are presented in Fig. 4.9 as functions of the ratio R_g/l_{corr}. For the range $0.137 \leq b/B \leq 6.21$, the energy range 200 PeV $\leq E \leq$ 5000 PeV, corresponding to $13.10 \leq R_g/l_{corr} \leq 327.58$, is investigated (see table L.2 for details). Data points are fitted with a linear fit in the log-log representation. With increasing ratio R_g/l_{corr}, all diffusion coefficients increase. The fits are presented in table L.2 and are shown as a function of the ratio b/B in Fig. 4.11 for $\kappa_\parallel$ (left) and for $\kappa_\perp$ (right). For $b/B \lesssim 2$, the slopes of the linear fits are around 1. It is worth mentioning that the presented simulation results in figure 4.9 are not contradictory to previous published data [11, 14–17, 20, 21, 52, 71, 77, 78, 88]. The energy range presented in this thesis simply extends that of previous studies.

Figure 4.10 tests the parallel diffusion coefficient dependency on the energy and magnetic field configuration simultaneously. This approach increases the statistics dramatically, given that the presented 60 simulated diffusion coefficients are considered at the same time. The presented fit demonstrates remarkable agreement of the simulated data with the prediction $\kappa_\parallel \propto EB/b^2$. Even though the energy dependence of the diffusion coefficient has been widely investigated [11, 13–17, 20, 21, 52, 71, 75, 77–79, 88], little attention has been paid to the validity range of the previously mentioned intermediate-energy regime. In fact it is widely assumed, that the discussed $\kappa_\parallel \propto E^2$ holds for all energies above the diffusive regime [20, 21, 71, 77, 78, 88].

Returning to the theoretical predictions, this thesis predicts either another energy regime or another numerical issue. The key argument for the transition into another regime was based on the increased gyroradius such that the gyromotion is at larger scales than that of the turbulence expressed through its correlation length. The derivation in Chapter 2 concluded a different dependency of the diffusion coefficient than what is expected for the intermediate-energy regime. However, with the applied simulation setup, especially with the stepsize $s_{step} = R_g/10$, the assumed decorrelation of the turbulent magnetic field vectors could originate from two different effects:

1. **Numerical Effect:** Above a certain energy, the applied stepsize $s_{step} = R_g/10$ results in steps that are larger than the correlation length of the turbulent magnetic field. Consequently, the magnetic field vector after each step is not correlated with the previous magnetic field vector. Consequently, it is expected, that the transition takes place at $s_{step} = R_g/10 \approx l_{corr}$. Rearranging yields $R_g/l_{corr} \approx 10$, which coincides with the presented transition in Fig. 4.1.

2. **Physical Effect:** As soon as the particle's gyroradius exceeds the scales of the turbulence expressed through its correlation length, the decorrelation of the magnetic field vectors is assumed. During one gyromotion, the particle interacts with magnetic field vectors that are not correlated with each other for a large gyroradius with respect to the correlation length of the turbulence.

The high-energy regime may be a consequence of the numerical effect explained above. A further study with more focus on testing the underlying effect is therefore suggested.

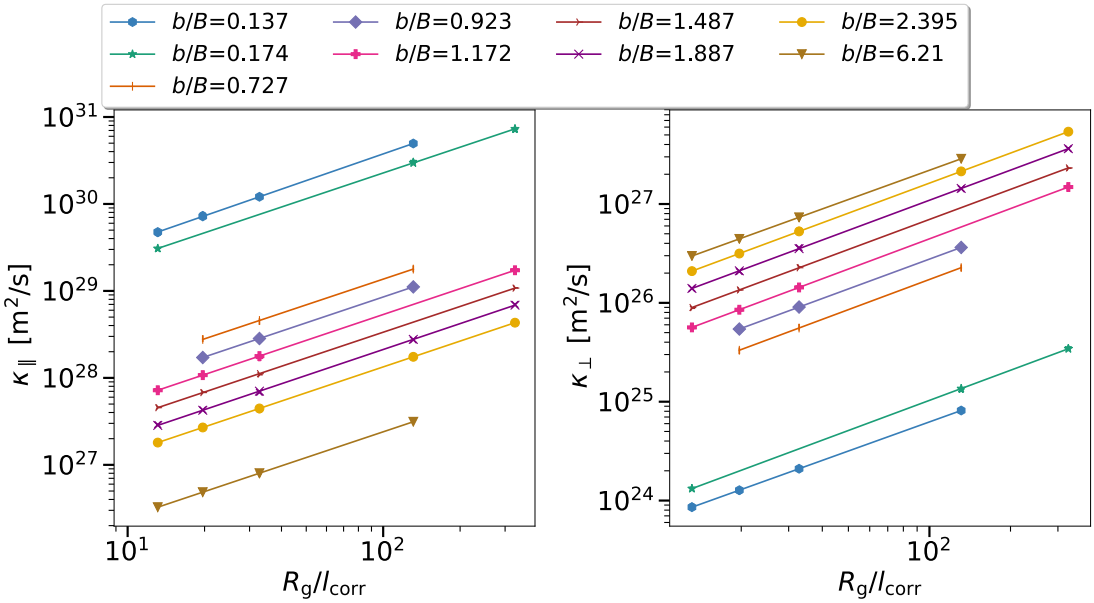

Figure 4.9: Parallel (left) and perpendicular (right) diffusion coefficient as functions of the ratio R_g/l_{corr} in the diffusive regime. Different ratios of b/B are investigated as presented in table L.2. The fitted slopes are listed in table L.2 and plotted against b/B in Fig 4.11 for $\kappa_{\parallel}$ and for $\kappa_{\perp}$.

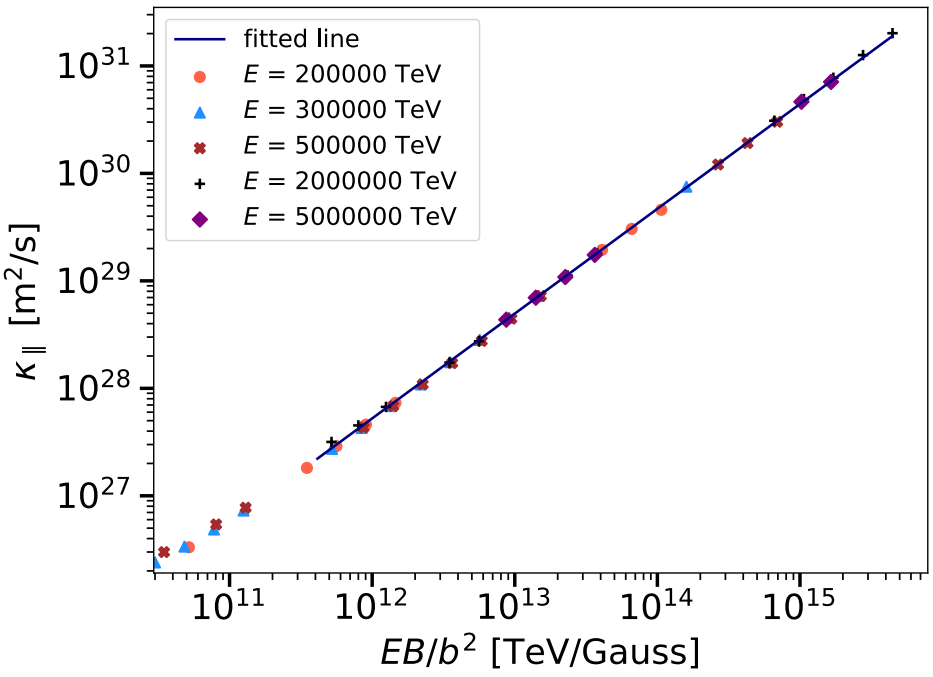

Figure 4.10: Parallel diffusion coefficient as functions of the ratio EB/b^2. The presented fit confirms the predicted dependency of the parallel diffusion coefficient $\kappa_{\parallel} \propto EB/b^2$ for the high-energy regime. Slope of the presented fit reads 0.975 ± 0.004.

4.5 Summary of Chapter

Magnetic Field Dependency: The predicted magnetic field dependency of the parallel diffusion coefficient $\kappa_{\parallel}$ is in agreement with the simulation results as summarized in Fig. 4.4, especially for high energetic particles.

Energy Dependency: The summary of the energy dependency of the perpendicular and parallel diffusion coefficient for all regimes is presented in Fig. 4.11. In the limit of $b \ll B$, the simulated parallel diffusion coefficients agree with the theoretically predicted dependencies from table 4.1.

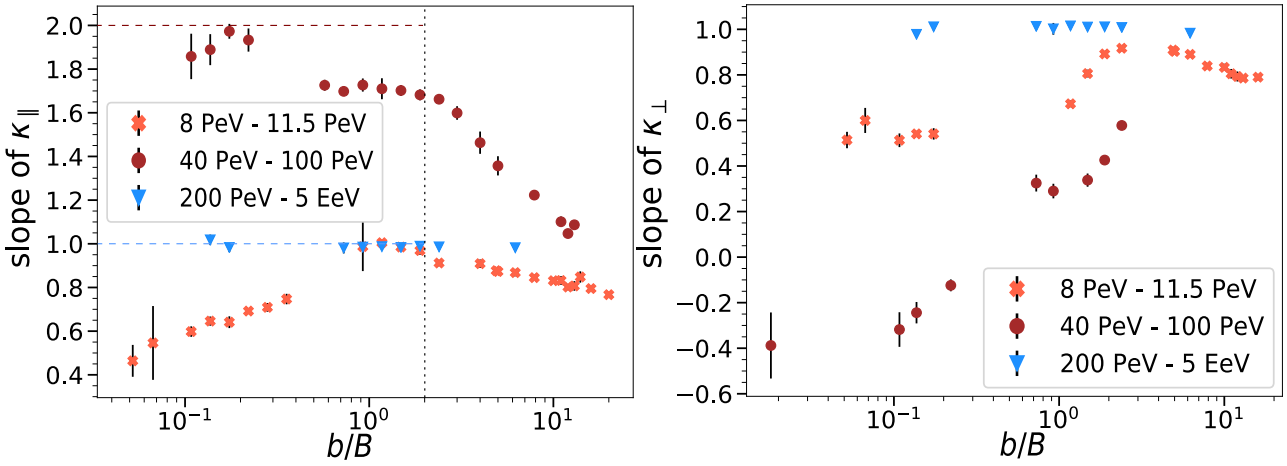

Figure 4.11: *Left panel:* Summary of the slopes fitted to the simulated perpendicular diffusion coefficient in the linear range of R_g/l_{corr} for the diffusive-energy, intermediate-energy and high-energy regime in Fig. 4.6, 4.8 and 4.9, respectively. The black dashed line shows the upper ratio b/B to which the theoretical predictions apply for the intermediate-energy and high-energy regime (see Appendix F). The colored dashed lines indicate the expected slopes for each energy regime. The theory for the diffusive-energy regime applies for the limit $b \ll B$ only.
Right panel: Summary of the slopes fitted to the simulated perpendicular diffusion coefficient in the linear range of R_g/l_{corr} for the diffusive-energy, intermediate-energy and high-energy regime in Fig. 4.6, 4.8 and 4.9, respectively.

Combined Dependencies: Besides investigating the magnetic field and energy dependencies independently, the present Chapter demonstrated the agreement of the parallel diffusion coefficient from both, the ratio b/B and the ratio R_g/l_{corr}, simultaneously. The agreement is illustrated for the high-energy regime in Fig. 4.10.

Range of b/B for which Theoretical Predictions are Applicable: In addition to the presented agreement of theoretical predictions and simulation results in the limit $b \ll B$, this Chapter indicated an extension of the b/B-range for which the theoretical predictions are applicable. The parallel diffusion coefficient dependencies on the ratio b/B presented in Fig. 4.3 demonstrate an agreement up to values of $b/B = 2$. The parallel diffusion coefficient dependency on the ratio R_g/l_{corr}, however, indicates different ranges of b/B for which the theoretically predicted dependencies agree with the simulated data. The range of ratios b/B for which the agreement is fulfilled increases for high energetic particles.

5 | Relation Between Perpendicular and Parallel Components

It is known from previous work [14, 89, 90] and also indicated by the results of Chapter 4 that a ratio of $b/B \gtrsim 10$ results in equal perpendicular and parallel components of the diffusion coefficient. At present, however, no encompassing theory exists capturing the relation between the parallel and perpendicular components over the whole range of b/B [15]. Thanks to the agreement of the parallel diffusion coefficient with the theoretical predictions derived in Chapter 2, such a relation between the diffusion coefficient components enhances the knowledge of the perpendicular diffusion coefficient. This is important, given that the transverse space diffusion is not well known yet [15]. However, it plays a crucial role in the confinement of cosmic rays in galaxies or other extragalactic objects. Furthermore, its magnitude is also of direct relevance to the performance of Fermi acceleration at perpendicular shocks discussed in Section 1.1.1.

The first in-depth discussions and analyses of this relation over a large range of ratios $\kappa_\perp/\kappa_\parallel$ emerged during the late 1990s [14]. This study demonstrated agreement of the simulation data for $R_\mathrm{g} \gg l_\mathrm{corr}$ with classical theory [14, 15], instead of agreement with QLT [89] and the related analysis [90]. The difference between the classical theory and the QLT is that the presented derivation neglects the diffusion of the gyrocenter carrying field line which is considered in the QLT [15, 89]. The underlying assumptions of the classical theory that are relevant to the following investigation are presented below (see [15] for details). It is assumed that the scattering time τ_s is defined as the coherence time of μ [15],

$$\tau_\mathrm{s} = \int_0^\infty \mathrm{d}\tau \ \left\langle \frac{\mu(\tau)\mu(0)}{\mu^2(0)} \right\rangle = \int_0^\infty \mathrm{d}\tau \exp\left(-\frac{\tau}{T}\right), \tag{5.1}$$

so that $T = \tau_\mathrm{s}$. With this assumption of the exponential decay on the characteristic time, the parallel diffusion coefficient yields [15]

$$\kappa_\parallel = c^2 \lim_{t\to\infty} \int_0^t \mathrm{d}\tau_1 \ \int_0^t \mathrm{d}\tau_2 \ \langle \mu(\tau_1)\mu(\tau_2)\rangle = \frac{c^2}{3}\tau_\mathrm{s}. \tag{5.2}$$

The parallel mean free path $\lambda_\parallel = 3\kappa_\parallel/c$ is the average distance a particle covers before being scattered by turbulence. With the additional assumption of $b \ll B$, the particle motion can be separated into the motion of the gyrocenter and the circular motion around it (see Section 2.3 for details). Furthermore, it is assumed that μ varies on the timescale τ_s, which is much longer than R_g. The perpendicular diffusion coefficient reads [15]

$$\kappa_\perp = \frac{c^2}{3} \frac{\tau_\mathrm{s}}{1 + (\lambda_\parallel/R_\mathrm{g})^2}. \tag{5.3}$$

Based on Equ. (5.2) and Equ. (5.3), the classical theory predicts

$$\frac{\kappa_\perp}{\kappa_\parallel} = \frac{1}{1 + (\lambda_\parallel / R_\mathrm{g})^2}. \tag{5.4}$$

The aim of this Section is to provide an extended study of the relation between the perpendicular and parallel diffusion coefficients presented in [14]. For this investigation, each set of simulations uses a constant correlation length and particle energy while varying b, given that Fig. 3.10 indicates different ratios of $\kappa_\perp/\kappa_\parallel$ for varying ratios b/B.

5.1 Classical Theory

The different ratios of $\kappa_\perp/\kappa_\parallel$ were fitted using a generalized form of Equ. (5.4)

$$\frac{\kappa_\perp}{\kappa_\parallel} = \frac{a_3}{1 + (\lambda_\parallel / a_2)^{a_1}}. \tag{5.5}$$

Different sets were simulated using different particle energies as indicated in Fig. 5.1, where the ratios of $\kappa_\perp/\kappa_\parallel$ are presented as functions of $\lambda_\parallel$. Fits are applied based on Equ. (5.5) for different energies. The log-log representation highlights the agreement of the fits in the area of large $\lambda_\parallel$. Figure 5.2 presents the same data as Fig. 5.1, however, in a different representation. In this log-lin representation, the ratios $\kappa_\perp/\kappa_\parallel$ are around 0 for large values of $\lambda_\parallel$ as indicated with the horizontal line at $\kappa_\perp/\kappa_\parallel = 0$. It is therefore possible to visually highlight the agreement of the simulated data with each fit of Equ. (5.5) either for short $\lambda_\parallel$ as shown in a log-log representation in Fig. 5.2 or for large values in a log-lin representation in Fig. 5.1.

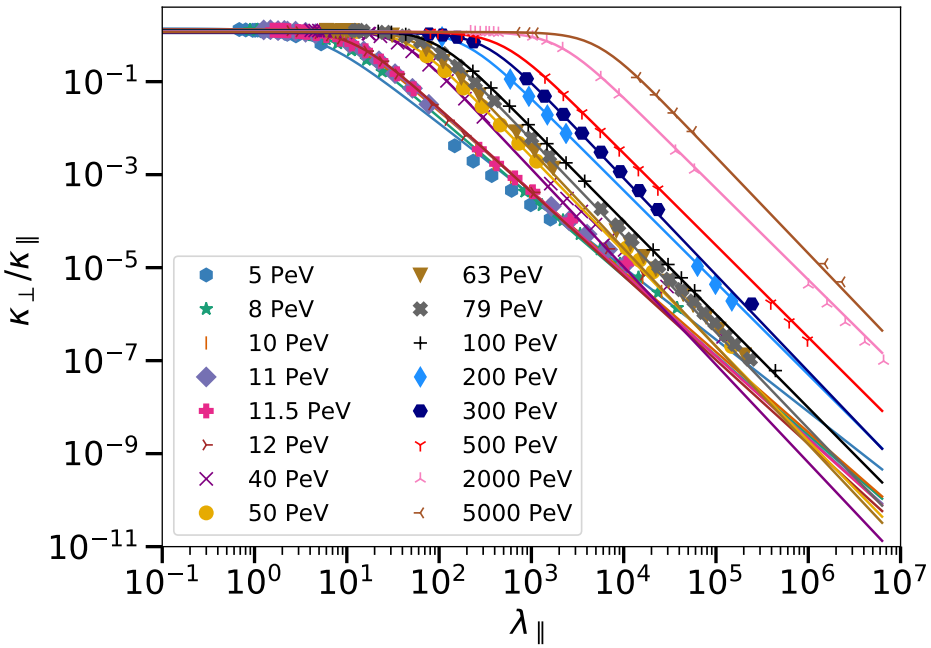

Figure 5.1: Ratio of the perpendicular to the parallel diffusion coefficient as a function of the parallel mean free path of the particles. Different energies are evaluated as indicated in the legend. The representation of the data in this log-log plot highlights the agreement with the fit presented in Equ. (5.5) for large values of the parallel mean free path.

The fit parameters a_1, a_2 and a_3 are shown in Fig. 5.3 and 5.4 as functions of the ratios $R_\mathrm{g}/l_\mathrm{corr}$ (R_g in Fig. A), respectively.

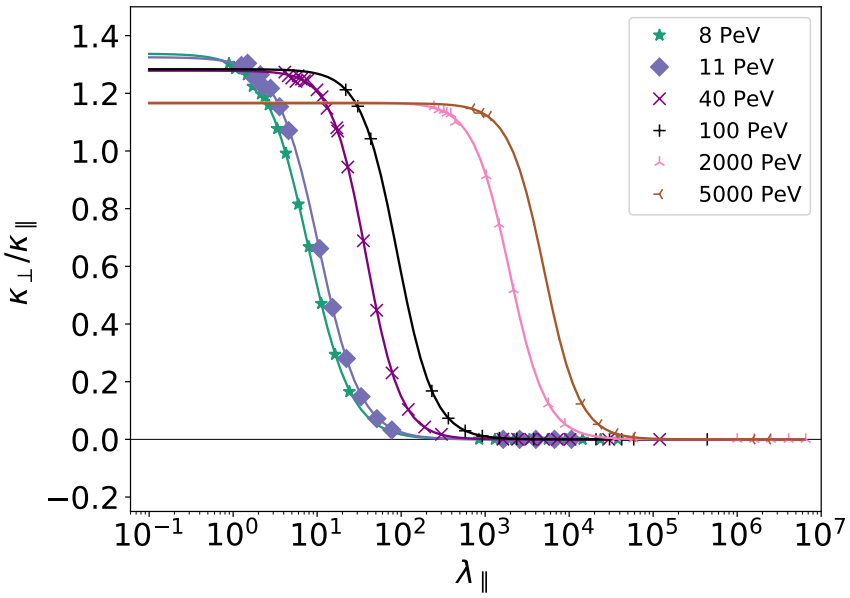

Figure 5.2: Ratio of the perpendicular to the parallel diffusion coefficient as a function of the parallel mean free path of the particles. Different energies are evaluated as indicated in the legend. The representation of the data in this log-lin plot highlights the agreement with the fit presented in Equ. (5.5) for small values of the parallel mean free path.

Figure 5.3 is revealing in several ways: First, unlike the other fit parameters, the functional dependence of a_1 on the ratio R_g/l_{corr} can be divided into two regimes. Second, the value of the fit parameter for the intermediate-energy and high-energy regimes is around 2 and therefore consistent with the study [14]. This result suggests that the dependence on the ratio of R_g/l_{corr} is best described using the classical theory.
The fit in the left panel of Fig. 5.4 reveals the relation between the parameter a_2 and the gyroradius $R_g \propto a_2$. This is in agreement with Equ. (5.4) and not only applicable for highly energetic particles.

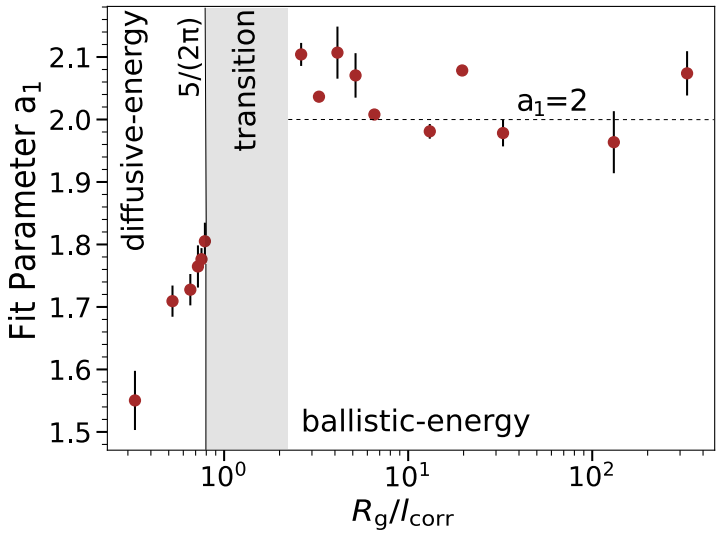

Figure 5.3: Fit parameter a_1 of Equ. (5.5) as a function of the ratio R_g/l_{corr}.

In the right panel of Fig. 5.4, the parameter a_3 is shown as a function of the ratio R_g/l_{corr}. This relation, however, indicates a dominance of the perpendicular diffusion coefficient over the parallel component, especially for small ratios R_g/l_{corr}, given that all values of a_3 are larger than 1. Small ratios of R_g/l_{corr} correspond to small parallel diffusion coefficients and consequently to small $\lambda_\parallel$. This

effect is observable in Fig 5.2 as the ratios of $\kappa_\perp/\kappa_\parallel$ increase with a decreasing particle energy for small $\lambda_\parallel$. Inserting the inferred dependencies of the fit parameters into Equ. (5.5) yields

$$\frac{\kappa_\perp}{\kappa_\parallel} = \frac{(R_\mathrm{g}/l_\mathrm{corr})^{-0.026\pm0.003}}{1+(\lambda_\parallel/R_\mathrm{g})^{a_1}} \quad \text{with} \quad \begin{cases} a_1 = \left(\frac{R_\mathrm{g}}{l_\mathrm{corr}}\right)^{\xi_1} & \text{if in the diffusive-energy regime} \\ a_1 = \xi_2 & \text{if in the ballistic-energy regime} \end{cases}, \tag{5.6}$$

where ξ_1 and ξ_2 (approximately around 2) need to be determined by fitting the data point in the left panel of Fig. 5.3 in the diffusive-energy regime. The denominator in Equ. (5.6) is in agreement with the denominator of the predicted form of $\kappa_\perp/\kappa_\parallel$ based on the classical theory (see Equ. (5.4)) for the ballistic-energy regime within the statistical uncertainties. The form of the denominator is based on the assumptions used for deriving the perpendicular component of the diffusion coefficient in Equ. (5.3). Consequently, the assumption of weak turbulence, so that the particle motion can be separated into the motion of the gyrocenter and the circular motion around it (see Section 2.3 for details) is appropriate. The assumption of μ varying on a longer timescale than τ_s is also important for the agreement of the denominator of the theoretical prediction and the fitted simulation result. As expected, this assumption breaks down for the diffusive-energy regime resulting in a different for of the denominator in Equ. (5.6). The $R_\mathrm{g}/l_\mathrm{corr}$ dependency of the numerator is not completely understood yet, but indicates that the assumption of the exponential decay on the characteristic time may be improper.

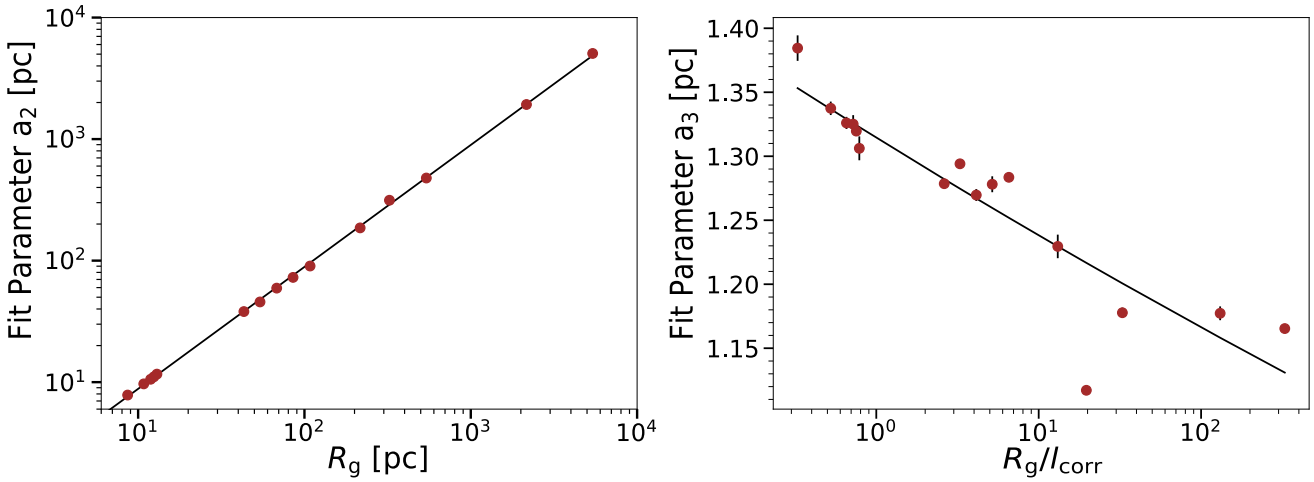

Figure 5.4: *Left panel*: Fit parameter a_2 of Equ. (5.5) as a function of the ratio R_g. It can be concluded that $a_2 \propto R_\mathrm{g}^{1.003\pm0.005}$. *Right panel*: Fit parameter a_3 of Equ. (5.5) as a function of the ratio $R_\mathrm{g}/l_\mathrm{corr}$. It can be concluded that $a_3 \propto R_\mathrm{g}^{-0.026\pm0.003}$.

5.2 Generalized Relation between Perpendicular and Parallel Components

In order to summarize the relation between the perpendicular and parallel components of the diffusion coefficient, the simulation results for all individual energies in the ballistic-energy regime (a_1 yields 2.0 according to Fig. 5.3), are taken into account. The ratio of $\kappa_\perp/\kappa_\parallel$ yields for energies above the diffusive-energy regime

$$\frac{\kappa_\perp}{\kappa_\parallel} = \frac{(R_\mathrm{g}/l_\mathrm{corr})^{-0.026}}{1+(\lambda_\parallel/R_\mathrm{g})^2}. \tag{5.7}$$

This particular form emerged from the previous discussion of the individual fit parameters. As already concluded during the discussion of the fit parameter a_1, the relation between the perpendicular and the parallel diffusion coefficient components is divided into two different regimes. In Fig. 5.8, all ratios of $\kappa_\perp/\kappa_\parallel$ are presented as functions of the right-hand term of Equ. (5.7).

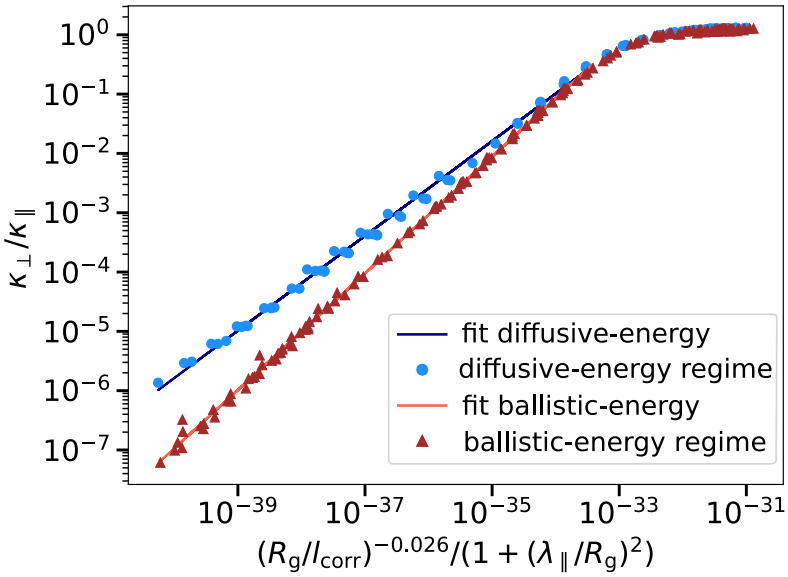

Figure 5.5: Ratio of components of the diffusion coefficient as a function of the right hand side of Equ. (5.5). A linear fit produces good agreement for the ballistic-energy regime. The diffusive-energy regime can best be described by a fit of a different slope, as it is already indicated in Fig. 5.3.

Fig. 5.5 reveals, however, that the relation of Equ. (5.7) can easily be extended such that it also describes the diffusive-energy regime. The right-hand term of Equ. (5.7) has to be generalized

$$\frac{\kappa_\perp}{\kappa_\parallel} = \left(\frac{(R_g/l_{corr})^{-0.026\pm0.003}}{1+(\lambda_\parallel/R_g)^2} \right)^\gamma \quad \text{with} \quad \begin{cases} \gamma = 0.799 \pm 0.005 & \text{if in the diffusive-}E\text{ regime} \\ \gamma = 0.983 \pm 0.002 & \text{if in the ballistic-}E\text{ regime} \end{cases} . \tag{5.8}$$

Again, the assumption that the particle motion can be separated into the motion of the gyrocenter and the circular motion around it as well as the assumption of μ varying on a longer timescale than τ_s are appropriate.

5.3 Chapter Summary

The presented results are significant in at least two major respects:

- The relation between the perpendicular and the parallel components of the diffusion coefficient can be classified in two different regimes – the diffusive-energy regime and the ballistic-energy (the transition agrees with that presented in Fig. 4.1 and starts at around R_g/l_{corr}).
- The advantage of the relation of the perpendicular and the parallel diffusion coefficient components is that it is sufficient to calculate the parallel component with the TGK-method and then apply Equ. (5.7) to deduce the perpendicular diffusion coefficient. This is more accurate and faster than the calculation of the perpendicular component by using the second moment method.

6 | Conclusions

Cosmic rays undergo diffusive transport when traveling through partially ionized plasma along continuous magnetic field lines B subject to turbulent perturbations b. The main challenge in the numerical evaluation of the diffusion coefficients arises from the necessity for a large range of particle energies to investigate the diffusion coefficient's energy dependency in different regimes. It is necessary to preserve the accuracy of the simulated diffusion coefficients over the whole range of particle energies, given that the particle energy determines the range of plasma wavelengths with which the particles can resonantly interact.

The present thesis provides an important step toward investigating physical diffusion coefficient dependencies by resolving these numerical issues, most notably by introducing parameter combinations on which the diffusion coefficient has a real functional dependence, in addition to presenting relevant convergence tests for those combinations that depict a numerical influence. This thesis demonstrates the reduction of numerical artifacts for the calculation of the diffusion coefficient by providing important conditions.

The present thesis highlights that an especially challenging problem arises in the low-energy domain due to missing resonant interaction possibilities of the particles with the turbulence. The question of how far the energy range can be extended toward lower energies without introducing numerical artifacts due to missing resonant interactions is addressed. The physical motivation for the case where scattering processes may be prevented around $\mu \approx 0$, however, is given by the idea to modify the diffusion coefficient so as to account for both gyroresonant scattering and mirroring [86, 87]. Further research is required in order to understand all implications for the simulated diffusion coefficients for energies below the diffusive-energy regime.

Overall, this effort has revealed the exact upper and lower boundary of the diffusive-energy regime in which particles can scatter independently of their trajectory's alignment with regard to the background magnetic field. These findings are significant in at least two respects: First, at a ratio of $R_{\mathrm{g}}/l_{\mathrm{corr}}$ slightly lower than or near $5/(2\pi)$, the gyroresonance condition is satisfied for the largest range of the pitch angle cosine, which corresponds to the fewest missing resonant interactions of the particles. Second, decreasing the ratio $R_{\mathrm{g}}/l_{\mathrm{corr}}$ increases the number of missing scatterings, which artificially pollute the diffusion coefficients such that γ artificially decreases in the expression $\kappa_{\parallel} \propto E^{\gamma}$. Consequently, fitting to diffusion coefficients at ratios of $R_{\mathrm{g}}/l_{\mathrm{corr}}$ slightly smaller than or equal to $5/(2\pi)$ is crucial for determining the correct energy dependency of the diffusion coefficients.

These findings form the basis for both the interpretation of the present simulation results as well as a correction of the diffusion coefficient's energy dependency for data presented in previous studies. It is worth mentioning that the findings within this thesis are not contradictory to previously published data, even though the interpretation of the diffusion coefficient's energy dependency deviates significantly. The key result of this thesis identifies the aforementioned deviation relative to previous studies

and can be summarized as follows: Decreasing b/B decreases γ, which is qualitatively consistent with a value of $1/3$ for infinitesimal b/B. Further studies are planned to investigate if further decreasing the ratio of b/B results in slopes of $1/3$ consistent with the prediction of the quasi-linear theory (QLT). This trend is also visible for the corrected energy behavior of the parallel diffusion coefficients in the diffusive-energy regime of previous studies, which consistently yield $\gamma > 1/3$, even though many other studies have reported $\gamma = 1/3$ independently of b/B.
Furthermore, theoretical predictions for the diffusion coefficient's energy dependencies are developed for energies above the diffusive-energy and confirmed by simulation results. For these energies, this study confirms agreement of the simulation data for $R_\mathrm{g} \gg l_\mathrm{corr}$ with classical theory, instead of agreement with QLT.

Further research with more focus on determining the transition between the intermediate and the high-energy regime is suggested as it may also reveal the origin – either physical or numerical – of the high-energy regime.
The diffusion coefficient dependencies found within this thesis determine the trajectory length at which the transition from a ballistic to a diffusive-propagation regime takes place. This finding serves as a condition for dynamically switching between the numerical propagation based on solving the Lorentz force and based on solving the transport equation since the latter method is only feasible in the diffusive-propagation regime. This is an important step toward the development of a self-consistent transport software which is capable of propagating both Galactic and extragalactic cosmic rays. The next goal is to implement this functionality in CPRopa.

A | Simplified Model of a Radio Galaxy

A simple model of protons propagating within radio galaxies as presented in [20, 21, 23] will be discussed. In particular, protons will be considered, which were accelerated in the radio galaxy jets. A fraction of those accelerated protons will leave the jets and afterwards diffuse through their parent galaxy as illustrated in figure A.1. This discussion will remain agnostic as to the detailed form of the magnetic field, only assuming that it consists of a regular component which is ordered on kpc scales [17] and of a turbulent magnetic field component. Consequently, the regular part can be approximated as a uniform field on sufficiently small scales.

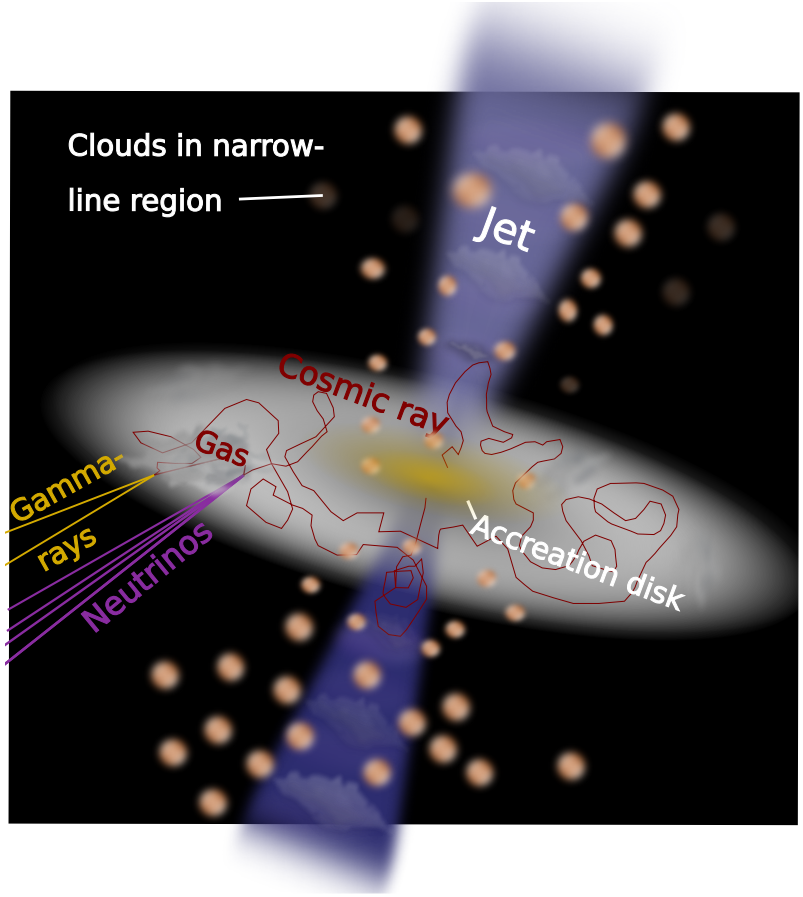

Figure A.1: Illustration of an accelerated proton diffusing within a radio galaxy. Interaction of the accelerated proton with a proton from the ambient gas within the galaxy, creates either four neutrinos or two gamma-rays.

The propagation of the protons can therefore be characterized through the spatial diffusion coefficient

$$\kappa_{\parallel} \propto \left(\frac{R_{\mathrm{g}}}{l_{\mathrm{corr}}}\right)^{\gamma} \left(\frac{b}{B}\right)^{-2}. \tag{A.1}$$

The time t_{diff} can be calculated, for which the protons will be confined within the radio galaxy and diffuse through its volume [20]

$$t_{\mathrm{diff}} \propto \frac{s_{\mathrm{diff}}^2}{2\kappa_{\parallel}} c\, l_{\mathrm{corr}}, \tag{A.2}$$

$$\propto \frac{s_{\mathrm{diff}}^2}{2\, c\, l_{\mathrm{corr}}} \left(\frac{l_{\mathrm{corr}}\, Bcq}{E_{\mathrm{p}}}\right)^{\gamma} \left(\frac{b}{B}\right)^2, \tag{A.3}$$

where s_{diff} is the displacement of the particle. During this time, the particle can interact with the prevailing gas of the galaxy. The probability P_{pp} of a hadronic interaction between a target proton from the ambient gas and the accelerated proton yields [20, 21, 23]

$$P_{\mathrm{pp}} = 1 - e^{-\tau_{pp}}, \tag{A.4}$$

given that the optical depth τ_{pp} is defined as

$$\tau_{\mathrm{pp}} = c\, \sigma_{\mathrm{pp}}\, t_{\mathrm{diff}}\, n_{\mathrm{gas}}. \tag{A.5}$$

Here, σ_{pp} represents the cross section of the hadronic interaction of two protons and n_{gas} is the average number density of the prevailing protons within the radio galaxy. For small optical depth, Equ. (A.4) can be approximated using the Taylor expansion which afterwards states

$$P_{\mathrm{pp}} \approx \tau_{\mathrm{pp}}. \tag{A.6}$$

Under the assumption of the pion production efficiency [23] of protons with an energy E_{p} greater than the threshold energy E_{th}

$$\xi_{\pi^{\pm}} = 2 \cdot \left(\frac{E_{\mathrm{p}} - E_{\mathrm{th}}}{\mathrm{GeV}}\right)^{1/4}, \tag{A.7}$$

together with the assumption of a power-law spectrum with the spectral index Γ_{p} of the protons, which is in agreement with possible acceleration mechanisms (see section 1.1.1)

$$\frac{\mathrm{d}N_{\mathrm{p}}}{\mathrm{d}E_{\mathrm{p}}} \propto E_{\mathrm{p}}^{-\Gamma_{\mathrm{p}}}, \tag{A.8}$$

the pion energy spectrum yields [23]

$$\frac{\mathrm{d}N_{\pi^{\pm}}}{\mathrm{d}E_{\pi^{\pm}}} \propto \int_{E_{\mathrm{th}}}^{\infty} \mathrm{d}E_{\mathrm{p}}\, \xi_{\pi^{\pm}}\, \delta(E_{\pi^{\pm}} - \langle E_{\pi^{\pm}} \rangle)\, P_{\mathrm{pp}}\, \frac{\mathrm{d}N_{\mathrm{p}}}{\mathrm{d}E_{\mathrm{p}}}, \tag{A.9}$$

$$\propto \left(\frac{Bcq}{\mathrm{GeV}}\right)^{\gamma} c\sigma_{\mathrm{pp}} \frac{s_{\mathrm{diff}}^2}{l_{\mathrm{corr}}^{1-\gamma}} \left(\frac{b}{B}\right)^2 n_{\mathrm{gas}} \int_{E_{\mathrm{th}}}^{\infty} \mathrm{d}E_{\mathrm{p}}\, \delta(E_{\pi^{\pm}} - \langle E_{\pi^{\pm}} \rangle) \left(\frac{E_{\mathrm{p}}}{\mathrm{GeV}}\right)^{-\Gamma_{\mathrm{p}}-\gamma+1/4}. \tag{A.10}$$

Here, $\langle E_{\pi^{\pm}} \rangle$ denotes the average fraction of energy carried by a pion and is given as [23]

$$\frac{\langle E_{\pi^{\pm}} \rangle}{\mathrm{GeV}} \propto \left(\frac{E_{\mathrm{p}}}{\mathrm{GeV}}\right)^{3/4}. \tag{A.11}$$

Applying the substitution $\chi := \langle E_{\pi^\pm} \rangle \propto \left(\frac{E_\mathrm{p}}{\mathrm{GeV}}\right)^{3/4} \mathrm{GeV}$ and consequently $\mathrm{d}E_\mathrm{p} \propto \mathrm{d}\chi \left(\frac{\chi}{\mathrm{GeV}}\right)^{1/3}$ in Equ. (A.10) results in

$$\frac{\mathrm{d}N_{\pi^\pm}}{\mathrm{d}E_{\pi^\pm}} \propto \left(\frac{Bcq}{\mathrm{GeV}}\right)^\gamma c\sigma_\mathrm{pp} \frac{s_\mathrm{diff}^2}{l_\mathrm{corr}^{1-\gamma}} \left(\frac{b}{B}\right)^2 n_\mathrm{gas} \int_{\chi_\mathrm{th}}^\infty \mathrm{d}\chi\, \delta(E_{\pi^\pm} - \chi) \left(\frac{\chi}{\mathrm{GeV}}\right)^{-\frac{4}{3}(\Gamma_\mathrm{p}+\gamma-1/2)}, \tag{A.12}$$

$$\propto \left(\frac{Bcq}{\mathrm{GeV}}\right)^\gamma c\sigma_\mathrm{pp} \frac{s_\mathrm{diff}^2}{l_\mathrm{corr}^{1-\gamma}} \left(\frac{b}{B}\right)^2 n_\mathrm{gas} \left(\frac{E_{\pi^\pm}}{\mathrm{GeV}}\right)^{-\frac{4}{3}(\Gamma_\mathrm{p}+\gamma-1/2)}. \tag{A.13}$$

The resulting neutrino and gamma-ray spectra are given by

$$\frac{\mathrm{d}N_{\nu,\gamma}}{\mathrm{d}E_{\nu,\gamma}} \propto \left(\frac{Bcq}{\mathrm{GeV}}\right)^\gamma c\sigma_\mathrm{pp} \frac{s_\mathrm{diff}^2}{l_\mathrm{corr}^{1-\gamma}} \left(\frac{b}{B}\right)^2 n_\mathrm{gas} \left(\frac{E_{\nu,\gamma}}{\mathrm{GeV}}\right)^{-\frac{4}{3}(\Gamma_\mathrm{p}+\gamma-1/2)}. \tag{A.14}$$

by assuming that each produced secondary has the same fraction of the total energy of the original pion [20, 21, 23]. For a Kolmogorov spectrum, with $\gamma = 1/3$ in the limit $b \ll B$, the energy dependency yields

$$\frac{\mathrm{d}N_{\nu,\gamma}}{\mathrm{d}E_{\nu,\gamma}} \propto \left(\frac{E_{\nu,\gamma}}{\mathrm{GeV}}\right)^{-\frac{4}{3}\Gamma_\mathrm{p}+2/9}, \tag{A.15}$$

which is slightly different to the presented result in [20, 21]

$$\frac{\mathrm{d}N_{\nu,\gamma}}{\mathrm{d}E_{\nu,\gamma}} \propto \left(\frac{E_{\nu,\gamma}}{\mathrm{GeV}}\right)^{-\frac{4}{3}\Gamma_\mathrm{p}+1/3}. \tag{A.16}$$

The difference is, however, small in comparison to the uncertainties of $\frac{\mathrm{d}N_{\nu,\gamma}}{\mathrm{d}E_{\nu,\gamma}}$ and Γ_p.

Returning, for example, to the production of secondaries in radio galaxies, these dependencies constrain the intensity and spectral shape of the cosmic rays accelerated and injected from their sources. This is possible due to recently observed multi-messenger data and deduced values for the spectral slopes Γ_ν and Γ_γ [20, 23, 91–96], together with the relations derived in the appendix

$$\frac{\mathrm{d}N_\nu}{\mathrm{d}E_\nu} \propto \left(\frac{E_\nu}{\mathrm{GeV}}\right)^{-\frac{4}{3}(\Gamma_\mathrm{p}+\gamma-1/2)}, \tag{A.17}$$

$$\frac{\mathrm{d}N_\gamma}{\mathrm{d}E_\gamma} \propto \left(\frac{E_\gamma}{\mathrm{GeV}}\right)^{-\frac{4}{3}(\Gamma_\mathrm{p}+\gamma-1/2)}. \tag{A.18}$$

At this point, the agreement of the theoretical predictions with the simulated data in the diffusive regime, motivates for physical implications: Equ. (A.17) can be used to constrain the spectral index of the injected protons

$$\Gamma_\mathrm{p} = \frac{3}{4}\Gamma_\gamma - \gamma + 1/2, \tag{A.19}$$

given that the gamma-ray spectral indexes are between 2.0 and 2.4 [21].

Diffusive-Energy Regime In the limit of $b \ll B$, theory (see Section 2.2) predicts γ yields 1/3 as demonstrated in this Section. The range of the restricted spectral index of the injected protons yields therefore $\Gamma_\mathrm{p} \approx 1.67 - 1.97$ and is in agreement with the predicted spectral index range [49, 97] based on the Fermi acceleration (see Section 1.1.1) under consideration of relativistic effects. In addition, the observed ultra-high-energy cosmic ray spectrum can be explained based on the calculated range of Γ_p

[21, 98–100]. This thesis demonstrates however an increase value for γ in the range of $0.1 \lesssim b/B \lesssim 1$. The details are presented in Chapter 4.

Intermediate-Energy Regime Section 4.3 confirms the theoretical prediction of $\gamma \approx 2$ in the intermediate-energy regime. Consequently, this changes the expected spectral indices of Γ_γ and Γ_ν. According to Equ. (A.17), a cut-off in the energy spectrum of neutrinos and gamma-rays form radio galaxies is expected. The neutrino and gamma-ray energies at which the cut-off takes place, depends on the correlation length and proton energy. The correlated proton energy, for which the cut-off takes place in the energy spectrum of the created secondary particles is defined by Equ. (3.18) and yields $R_\mathrm{g}/l_\mathrm{corr} = 5/(2\pi)$. Consequently, information on the magnetic field composition may be deduced based on the cut-off energies of the secondary particle spectra. With the Cherenkov Telescope Array (CTA) [36], the expected cut-off energy and energy spectrum of gamma-rays can be refined and tested. Furthermore, future high-energy neutrinos telescopes with increased sensitivity to TeV-PeV neutrinos [101–103] could test the predicted cut-off energy spectrum.

High-Energy Regime Section 4.4 confirms the theoretical prediction within the present thesis of $\gamma \approx 1$ in the limit $l_\mathrm{corr} \ll R_\mathrm{g}$. If further studies suggest the physical reason for the deccorelation of the turbulent magnetic field, this finding has important implications for many astro-physical environments as, for example, for the case of high-energy protons diffusing in a radio galaxy. In accordance to Equ. (A.19) and assuming the same injected proton spectrum range $\Gamma_\mathrm{p} \approx 1.67 - 1.97$ as concluded above for the diffusive-energy regime, the spectral indexes of the gamma-ray and neutrino energy spectrum is constraint to the range $\Gamma_{\gamma,\nu} \approx 1 - 1.3$. This expected range is distinct to that assuming $\kappa \propto E^2$, which yields $\Gamma_{\gamma,\nu} \approx 0 - 0.3$.

These findings constrain the intensity and spectral shape of proton energy spectrum from the diffusive regime which were accelerated and injected from radio galaxy jets according to Equ. (A.17). Assuming that the spectral index of protons from the intermediate and high-energy regime is comparable to that of the diffusive regime, a cut-off in the neutrino and gamma-ray spectrum is expected because of the cut-off in the energy dependency of the diffusion coefficient. For this conclusion it is necessary to assume that these neutrinos and gamma-rays were created during hadronic interactions of gas with the protons diffusing from the jets into the galaxy as shown in Fig. A.1. With future observations of CTA and newer IceCube generations of high energetic gamma-rays and neutrinos, respectively, those predictions can be tested and verified. It is assumed that the secondary particles were created during hadronic interactions of the prevailing gas with accelerated cosmic rays that left the jet and diffuse through their parent galaxy [20, 21]. Consequently, knowledge of the diffusion coefficient dependencies constrains the intensity and spectral shape of the accelerated cosmic rays from AGNs, given that recent Fermi [20, 91, 92], Hess [93, 94] and IceCube data [23, 95, 96] restrict Γ_ν and Γ_γ.

B | Acceleration of Particles

Fermi [25] suggested that cosmic rays gain their energy from large-scale fluid motion during the accumulation of individual acceleration and escape events in turbulent magnetic fields. In each cycle of the acceleration process, the initial particle energy E_0 is incremented by the gain $\Delta E = E \cdot \xi$, yielding

$$E_1 = E_0 + \Delta E = E_0(1 + \xi), \tag{B.1}$$

where ξ denotes the energy gain factor and E_1 the new energy. After n acceleration cycles, the energy E_n of the particle reads

$$E_n = E_0(1 + \xi)^n. \tag{B.2}$$

To compute the energy spectrum, the number of particles N which are still confined in the system has to be determined. Under the basic assumption of $N_{\text{esc}} = N \cdot P_{\text{esc}}$ particles leaving the system in each cycle, where P_{esc} denotes the escape probability of the acceleration region in each encounter, the number N_1 of particles after the first iteration is given by

$$N_1 = N_0 - N_0 \cdot P_{\text{esc}}. \tag{B.3}$$

The number of particles with an energy greater than that after n steps is

$$N(E > E_n) = \sum_{m=n}^{\infty} N_0(1 - P_{\text{esc}})^m = \frac{N_0(1 - P_{\text{esc}})^n}{P_{\text{esc}}}, \tag{B.4}$$

where an index transformation together with the definition of a geometric series is used in the last step. Equ. (B.2) is used to derive an expression for the number of acceleration iterations

$$n = \frac{\log(E_n/E_0)}{\log(1 + \xi)}, \tag{B.5}$$

which can then be inserted in Equ. (B.4), leading to the energy spectrum

$$N \propto E^{-q} \Rightarrow \frac{dN}{dE} \propto E^{-q-1}, \tag{B.6}$$

where q is defined as $q \approx P_{\text{esc}}/\xi$. The repeated processes of small accelerations thus inevitably lead to a power-law energy spectrum.

C | 1D Solution of the Diffusion Equation for a Point Source

A point-like source as the initial condition of the problem is represented by a *Dirac Delta* distribution at $t = 0$

$$M(x_i', 0) = \delta(x_i'). \tag{C.1}$$

In order to solve the differential Equ. (2.19), the time component and the spatial component can be separated with the ansatz

$$M(x_i, t) = \rho(t)P(x_i). \tag{C.2}$$

Rearranging the terms leads to

$$\frac{1}{\kappa_{ii}\rho(t)}\frac{\partial\rho(t)}{\partial t} = \frac{1}{P(x_i)}\frac{\partial^2 P(x_i)}{\partial^2 x_i} = -k^2. \tag{C.3}$$

The time component can be written as

$$\frac{\partial\rho(t)}{\partial t} = -k^2\kappa_{ii}\rho(t) \tag{C.4}$$

with the following solution

$$\rho(t) = \rho_0 \cdot \exp(-k^2\kappa_{ii}t). \tag{C.5}$$

The spatial component can be written as

$$\frac{\partial^2 P(x_i)}{\partial^2 x_i} = -k^2 P(x_i), \tag{C.6}$$

which yields

$$P(x_i) = P_0 \cdot \exp(ik(x_i - x_i')). \tag{C.7}$$

The next step is combining the solutions of $\rho(t)$ and $P(x_i)$ to evaluate the averaged particle density

$$M(x_i, t) = \rho_0 P_0 \cdot \exp(ik(x - x')) \cdot \exp(-k^2\kappa_{ii}t), \tag{C.8}$$

which can be generalized, because Equ. (C.8) applies for every parameter k and every initial position of each particle. The general solution is the superposition of all special solutions, which can be expressed

in integral notation

$$M(x_i,t) = \int \mathrm{d}k \int \mathrm{d}x_i' \; M(x_i',0) \exp\left(-k^2\kappa_{ii}t + ik(x_i - x_i')\right). \tag{C.9}$$

In this form, the initial condition $M(x_i',0)$ (Equ. (C.1)) can be inserted. First, solving the integral over x_i with the application of $\int \mathrm{d}\, x' f(x-x')\delta(x') = f(x)$ yields

$$M(x_i,t) = \int \mathrm{d}k \exp\left(-k^2\kappa_{ii}t + ikx_i\right). \tag{C.10}$$

Until now, the spatial component is still separate from the time component. Completing the square leads to

$$M(x_i,t) = \int \mathrm{d}k \exp\left(-k^2\kappa_{ii}t + ikx_i + \frac{1}{4}\frac{x_i^2}{\kappa_{ii}t} - \frac{1}{4}\frac{x_i^2}{\kappa_{ii}t}\right) \tag{C.11}$$

$$= \int \mathrm{d}k \exp\left(\left(ik\sqrt{\kappa_{ii}t} + \frac{1}{2}\frac{x_i}{\sqrt{\kappa_{ii}t}}\right)^2 - \frac{1}{4}\frac{x_i^2}{\kappa_{ii}t}\right) \tag{C.12}$$

$$= \exp\left(-\frac{1}{4}\frac{x_i^2}{\kappa_{ii}t}\right) \int \mathrm{d}k \;\; \exp\left(\left(ik\sqrt{\kappa_{ii}t} + \frac{1}{2}\frac{x_i}{\sqrt{\kappa_{ii}t}}\right)^2\right) \tag{C.13}$$

and solving the integral over k using the *Gaussian integral* leads to the form

$$M(x_i,t) = \frac{1}{2\sqrt{\pi\kappa_{ii}t}} \exp\left(-\frac{x_i^2}{4\kappa_{ii}t}\right). \tag{C.14}$$

D | 3D Solution of the Diffusion Equation for a Point Source

The three-dimensional diffusion equation is solved in this Chapter

$$\frac{\partial M(x_1,x_2,x_3,t)}{\partial t} = \kappa_{x_1x_1}\frac{\partial^2 M(x_1,x_2,x_3,t)}{\partial x_1^2} + \kappa_{x_2x_2}\frac{\partial^2 M(x_1,x_2,x_3,t)}{\partial x_2^2} + \kappa_{x_3x_3}\frac{\partial^2 M(x_1,x_2,x_3,t)}{\partial x_3^2}. \tag{D.1}$$

Inserting the product *ansatz*

$$M(x_1,x_2,x_3,t) = \rho(t)P(x_1)P(x_2)P(x_3) \tag{D.2}$$

into equation D.1 and separating the four different variables leads to

$$\frac{1}{\rho(t)}\frac{\partial\rho(t)}{\partial t} = \frac{\kappa_{x_1x_1}}{P(x_1)}\frac{\partial^2 P(x_1)}{\partial^2 x_1} + \frac{\kappa_{x_2x_2}}{P(x_2)}\frac{\partial^2 P(x_2)}{\partial^2 x_2} + \frac{\kappa_{x_3x_3}}{P(x_3)}\frac{\partial^2 P(x_3)}{\partial^2 x_3} = -3\,k^2. \tag{D.3}$$

Due to symmetry reasons, following expression can be motivated

$$\frac{\kappa_{x_1x_1}}{P(x_1)}\frac{\partial^2 P(x_1)}{\partial^2 x_1} = \frac{\kappa_{x_2x_2}}{P(x_2)}\frac{\partial^2 P(x_2)}{\partial^2 x_2} = \frac{\kappa_{x_3x_3}}{P(x_3)}\frac{\partial^2 P(x_3)}{\partial^2 x_3} = -k^2. \tag{D.4}$$

Each differential equation can be solved individually and independently, as already presented for the 1-D solution. Inserting those solutions into equation D.2 yields

$$M(x_1,x_2,x_3,t) = \int \mathrm{d}k \int \mathrm{d}x_1' \int \mathrm{d}x_2' \int \mathrm{d}x_3' M(x_1',0)M(x_2',0)M(x_3',0)\cdot \\ \exp\left(-3k^2t + i\frac{k}{\sqrt{\kappa_{x_1x_1}}}(x_1-x_1') + i\frac{k}{\sqrt{\kappa_{x_2x_2}}}(x_2-x_2') + i\frac{k}{\sqrt{\kappa_{x_3x_3}}}(x_3-x_3')\right). \tag{D.5}$$

With the *delta* function, the result is again simplified the result again and after rearranging terms, one can solve the remaining integral over k

$$\begin{aligned}
M(x_1,x_2,x_3,t) &= \int \mathrm{d}k\ \exp\left(-3k^2t + i\frac{k}{\sqrt{\kappa_{x_1x_1}}}x_1 + i\frac{k}{\sqrt{\kappa_{x_2x_2}}}x_2 + i\frac{k}{\sqrt{\kappa_{x_3x_3}}}x_3\right) \\
&= \int \mathrm{d}k\ \exp\left(\left(-k^2t + i\frac{k}{\sqrt{\kappa_{x_1x_1}}}x_1\right)\left(-k^2t + i\frac{k}{\sqrt{\kappa_{x_2x_2}}}y\right) + \left(-k^2t + i\frac{k}{\sqrt{\kappa_{x_3x_3}}}x_3\right)\right) \\
&= \int \mathrm{d}k\ \exp\left(\left(ik\sqrt{t} + \frac{x_1}{2\sqrt{t\kappa_{x_1x_1}}}\right)^2 - \frac{x_1^2}{4\kappa_{x_1x_1}t}\right)\cdot \\
&\quad \exp\left(\left(ik\sqrt{t} + \frac{x_2}{2\sqrt{t\kappa_{x_2x_2}}}\right)^2 - \frac{x_2^2}{4\kappa_{x_2x_2}t} + \left(ik\sqrt{t} + \frac{x_3}{2\sqrt{t\kappa_{x_3x_3}}}\right)^2 - \frac{x_3^2}{4\kappa_{x_3x_3}t}\right) \\
&= \exp\left(-\frac{x_1^2}{4\kappa_{x_1x_1}t} - \frac{x_2^2}{4\kappa_{x_2x_2}t} - \frac{x_3^2}{4\kappa_{x_3x_3}t}\right)\cdot \\
&\quad \int \mathrm{d}k\ \exp\left(\left(ik\sqrt{t} + \frac{x_1}{2\sqrt{t\kappa_{x_1x_1}}}\right)^2 + \left(ik\sqrt{t} + \frac{x_2}{2\sqrt{t\kappa_{x_2x_2}}}\right)^2 + \left(ik\sqrt{t} + \frac{x_3}{2\sqrt{t\kappa_{x_3x_3}}}\right)^2\right).
\end{aligned} \tag{D.6}$$

The last step consists of solving the integral over k using the *Gaussian* integral

$$M(x_1,x_2,x_3,t) \quad = \quad \frac{1}{8\sqrt{\pi^3\,\kappa_{x_1x_1}\,\kappa_{x_2x_2}\,\kappa_{x_3x_3}\,t^3}}\ \cdot\ \exp\left(-\frac{x_1^2}{4\,\kappa_{x_1\,x_1}\,t} - \frac{x_2^2}{4\,\kappa_{x_2\,x_2}\,t} - \frac{x_3^2}{4\,\kappa_{x_3\,x_3}\,t}\right) \tag{D.7}$$

E | Relation Between Momentum and Spatial Diffusion Coefficient

The momentum diffusion coefficient D_v is introduced and the relation with the spatial diffusion coefficient $\kappa_\parallel$ is derived. This relation is especially useful because the calculation of D_v simplifies significantly for high-energy particles, constituting an elegant way of deriving $\kappa_\parallel$ for $R_\mathrm{g} \gg l_\mathrm{corr}$. The Fokker-Planck Equ. (2.7) can be simplified for the special case of isotropic turbulence

$$\frac{\partial f}{\partial t} + v_\mu \frac{\partial f}{\partial x_\mu} = D_v \sum_{\mu\neq\nu} \frac{\partial^2 f}{\partial v_\mu \partial v_\nu}, \tag{E.1}$$

for which the definition from [104] is applied

$$D_{\mu\nu}(v) = \left(\delta_{\mu\nu} - \frac{v_\mu v_\nu}{v^2}\right) D_v. \tag{E.2}$$

Multi-scale Methods and Perturbation Theory In order to benefit from the perturbation theory when solving Equ. (E.1), it is helpful to define first the fast changing temporal and spatial variable τ and ξ, respectively. For microscopic transport, the following fast temporal and spatial variables are defined

$$\tau = t; \quad \xi = x. \tag{E.3}$$

In the following, macroscopic transport will be treated as a small perturbation (see e.g. [71])

$$T = \epsilon^2 t; \quad X = \epsilon x, \tag{E.4}$$

where ϵ is a small parameter. Consequently, T and X are slowly changing variables with respect to t and x, respectively. The order in ϵ is motivated in a dimensional analysis based on the diffusion equation. Therefore, Equ. (E.1) can be applied to the multi-scale picture using the following derivations based on equations E.3 and E.4

$$\frac{\partial}{\partial t} = \frac{\partial}{\partial \tau} + \epsilon^2 \frac{\partial}{\partial T} \tag{E.5}$$

$$\frac{\partial}{\partial x} = \frac{\partial}{\partial \xi} + \epsilon \frac{\partial}{\partial X}. \tag{E.6}$$

The perturbation ansatz $f = f^{(0)} + \epsilon f^{(1)} + \epsilon^2 f^{(2)} + \mathcal{O}(\epsilon^3)$ yields the following expressions for the different orders in ϵ

$$\mathcal{O}(\epsilon^0) \; : \quad D_v \sum_{\mu\neq\nu} \frac{\partial^2 F^{(0)}}{\partial v_\mu \partial v_\nu} = 0, \tag{E.7}$$

where the time-averaging operator is already applied and in addition $\langle f^{(0)} \rangle$ is renamed as $F^{(0)}$. This is used for the next order in ϵ

$$\mathcal{O}(\epsilon^1) \ : \quad v_\mu \frac{\partial F^{(0)}}{\partial X_\mu} - D_v \sum_{\mu \neq \nu} \frac{\partial^2 F^{(1)}}{\partial v_\mu \partial v_\nu} = 0. \tag{E.8}$$

To solve this equation for $F^{(1)}$, the distribution $F^{(n)}$ is expanded in spherical harmonics

$$f^{(n)} = \sum_{l,m} C_{lm}^{(n)}(\mathbf{x}, v, t) Y_{lm}(\Theta, \Phi). \tag{E.9}$$

In a next step, the well-known property of the spherical harmonics is used

$$v^2 \sum_{\mu \neq \nu} \frac{\partial^2}{\partial v_\mu \partial v_\nu} Y_{lm}(\Theta, \Phi) = \left[-l(l+1)\right] Y_{lm}(\Theta, \Phi). \tag{E.10}$$

Aligning the direction into the z-axis constrains the possible harmonics without loss of generality. The consequence of this step is that $m = 0$ has to be fulfilled. With this trick, one can solve Equ. E.8 for $F^{(1)}$

$$\mathcal{O}(\epsilon^1) \ : \quad F^{(1)} = \frac{-v^2}{2D_v} v_\mu \frac{\partial F^{(0)}}{\partial X_\mu}. \tag{E.11}$$

Calculating the next order is straightforward and results in following expression

$$\mathcal{O}(\epsilon^2) \ : \quad \frac{\partial F^{(0)}}{\partial T} + v_\mu \frac{\partial F^{(1)}}{\partial X_\mu} - D_v \sum_{\mu \neq \nu} \frac{\partial^2 F^{(2)}}{\partial v_\mu \partial v_\nu} = 0. \tag{E.12}$$

Using the result from Equ. E.11 as well as Equ. E.10 yields

$$\frac{\partial F^{(0)}}{\partial T} = \frac{v^4}{6D_v} \sum_{\mu \neq \nu} \frac{\partial^2 F^{(2)}}{\partial v_\mu \partial v_\nu}. \tag{E.13}$$

This has the form of a diffusion equation with

$$\kappa = \frac{v^4}{6D_\nu}. \tag{E.14}$$

F | Range of b/B in which Classification in $\parallel$ and $\perp$ Components is Applicable

There are different definitions of the gyroradius in the literature for the case of a particle moving within an isotropic turbulent magnetic field b plus a background magnetic field B aligned along one direction. Fist, the gyroradius can be defined as [51]

$$R_{\mathrm{g}} = \frac{E}{Bqc}, \tag{F.1}$$

taking only the background magnetic field into account. The disadvantage is obvious for the limit $b \ll B$ with a vanishing background field, in which the gyroradius vanishes also. This can be solved by using an alternative definition of the gyroradius [15]

$$R_{\mathrm{g}} = \frac{E}{\sqrt{b^2 + B^2}qc}. \tag{F.2}$$

In the limit of $b \ll B$, both expressions coincide but in the opposite limit $b \gg B$ only the latter expression is meaningful. Another definition of the gyroradius is introduce within this thesis

$$R_{\mathrm{g}} = \frac{E}{B_{\mathrm{tot}}qc}, \tag{F.3}$$

where $B_{\mathrm{tot,3}}$ is the magnitude of the magnetic field along the x_3-axis, which averages to

$$B_{\mathrm{tot}} = \frac{1}{2\pi}\int_0^{2\pi} \mathrm{d}\phi\ \frac{1}{\pi}\int_0^{\pi} \mathrm{d}\theta\ |B + b\cdot\cos(\phi)\cdot\cos(\theta)|. \tag{F.4}$$

For the 2D case, Equ. (F.4) yields

$$B_{\mathrm{tot}} = \frac{1}{2\pi}\int_0^{2\pi} \mathrm{d}\phi\ |B + b\cdot\cos(\phi)|. \tag{F.5}$$

2D case for $b \leq B$: For $b \leq B$, the expression $B + b\cdot\cos(\phi)$ is positive for all ϕ. Therefore, Equ. (F.5) yields

$$\begin{aligned} B_{\mathrm{tot,3}} &= \frac{1}{2\pi}\int_0^{2\pi} \mathrm{d}\phi\ [B + b\cdot\cos(\phi)], \\ &= B. \end{aligned} \tag{F.6}$$

2D case for $b \geq B$: For $b \geq B$ and $\phi_{1,2} = \pm\hat{\phi} = \pm\cos^{-1}(-B/b)$, the expression $B + b \cdot \cos(\phi)$ changes its sign. Consequently, Equ. (F.5) yields

$$B_{\mathrm{tot}} = \frac{1}{2\pi}\int_{-\hat{\phi}}^{\hat{\phi}} \mathrm{d}\phi\ [B + b\cdot\cos(\phi)] - \frac{1}{2\pi}\int_{\hat{\phi}}^{2\pi-\hat{\phi}} \mathrm{d}\phi\ [B + b\cdot\cos(\phi)], \tag{F.7}$$

$$= \frac{1}{2\pi}[B(4\hat{\phi} - 2\pi) + 4b\cdot\sin(\hat{\phi})], \tag{F.8}$$

$$= \frac{1}{2\pi}\left(B(4\cos^{-1}(-B/b) - 2\pi) + 4b\cdot\sqrt{1-(B/b)^2}\right). \tag{F.9}$$

The analytical solution for the 2D case presented in Equ. (F.5) yields

$$B_{\mathrm{tot}} = \begin{cases} B & \text{if } b \leq B \\ \frac{1}{2\pi}\left(B(4\cos^{-1}(-B/b) - 2\pi) + 4b\cdot\sqrt{1-(B/b)^2}\right) & \text{if } b \geq B \end{cases}. \tag{F.10}$$

3D case for $b \leq B$: For $b \leq B$, the expression $B + b\cdot\cos(\phi)\cdot\cos(\theta)$ is positive for all ϕ and θ. Therefore, Equ. (F.4) yields

$$B_{\mathrm{tot}} = \frac{1}{2\pi}\int_0^{2\pi} \mathrm{d}\phi\ \frac{1}{\pi}\int_0^{\pi} \mathrm{d}\theta\ [B + b\cdot\cos(\phi)\cdot\cos(\theta)], \tag{F.11}$$

$$= B. \tag{F.12}$$

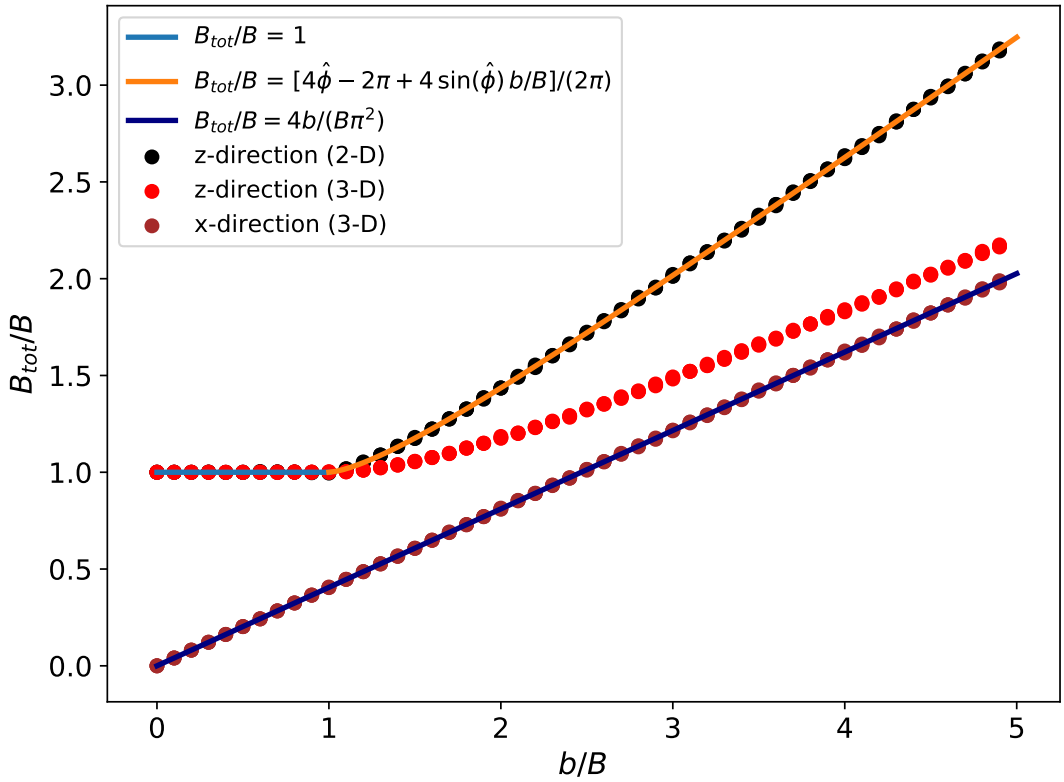

Figure F.1: Numerical and analytical solution to Equ. (F.4). $B_{\mathrm{tot}} = B$ for ratios of $b/B \leq 1$. Above $b/B = 1$, B_{tot} increases linearly slowly, so that at a ratio of $b/B = 4$ the fluctuations contribute to B_{tot} as much as B.

The findings of the integration in Equ. (F.4) are presented in Fig. F.1 for the 3D case numerically as well as for the 2D case both analytically and numerically. The calculations are presented as functions of the ratio b/B. Figure F.2 presents the same as Fig. but using an extended range in b/B, such that the case $b \gg B$ can be investigated. Using a fit to the numerically evaluated results for the 3D case in the limit $b \gg B$, see Fig. F.1, one may write the total magnetic field as $B_{\mathrm{tot}} \approx 4b/\pi^2$. This finding is in agreement with the analytically derived result presented below in Equ. (F.13).

3D case for $b \gg B$: In the limit $b \gg B$ Equ. (F.4) yields

$$\begin{aligned} B_{\mathrm{tot}} &= \frac{1}{2\pi}\int_0^{2\pi} \mathrm{d}\phi\, \frac{1}{\pi}\int_0^{\pi} \mathrm{d}\theta\, |B + b\cdot\cos(\phi)\cdot\cos(\theta)| \\ &\approx \frac{1}{2\pi^2}\int_0^{2\pi} \mathrm{d}\phi \int_0^{\pi} \mathrm{d}\theta\, |b\cdot\cos(\phi)\cdot\cos(\theta)|, \\ &= \frac{b}{2\pi^2}\int_0^{2\pi} \mathrm{d}\phi \left(\int_0^{\pi/2} \mathrm{d}\theta\, |\cos(\phi)|\cdot\cos(\theta) - \int_{\pi/2}^{\pi} \mathrm{d}\theta\, |\cos(\phi)|\cdot\cos(\theta)\right), \\ &= \frac{2b}{2\pi^2}\int_0^{2\pi} \mathrm{d}\phi\, |\cos(\phi)|, \\ &= \frac{4b}{\pi^2}. \end{aligned} \tag{F.13}$$

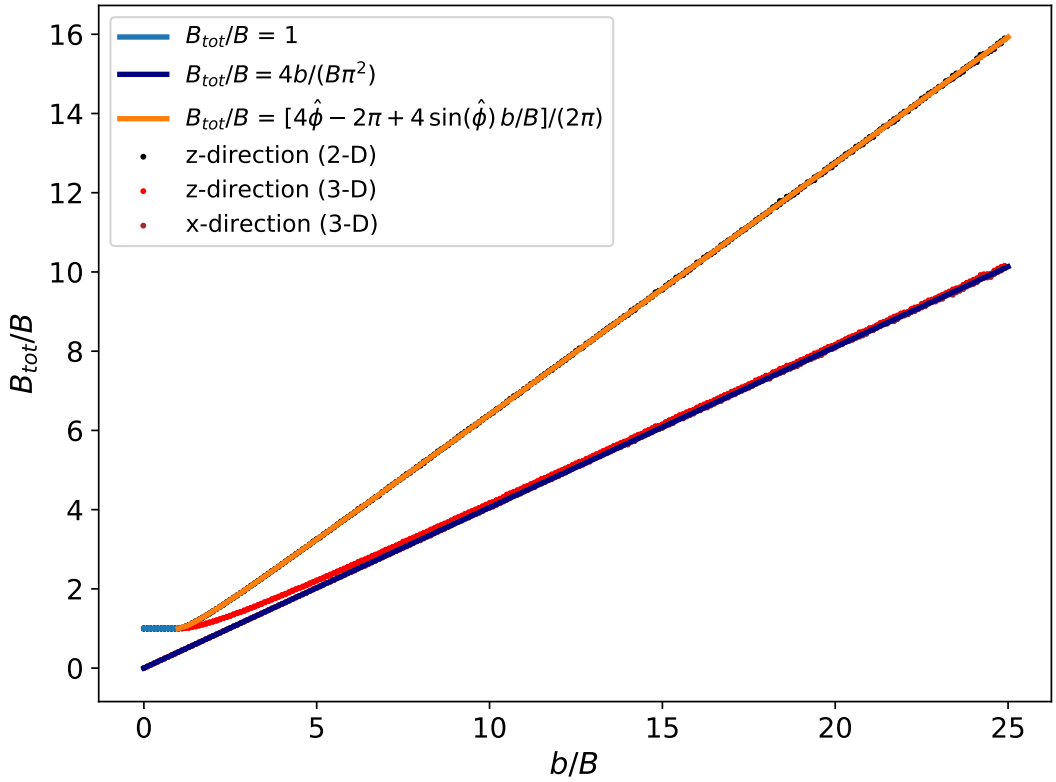

Figure F.2: Numerical and analytical solution to Equ. (F.4). $B_{\mathrm{tot}} = B$ for ratios of $b/B \leq 1$. Above $b/B = 1$, B_{tot} increases linearly slowly, so that at a ratio of $b/B = 4$ the fluctuations contribute to B_{tot} as much as B.

The findings for the 3D case can be summarized as

$$B_{\mathrm{tot}} = \begin{cases} B & \text{if } b \lesssim B \\ 4b/(\pi^2) & \text{if } b \gg B \end{cases} . \tag{F.14}$$

Figure F.3 in the Appendix F presents the ratio of the magnetic field components as functions of the ratio b/B, which is based on the numerically calculated projections of B_{tot} in the parallel and perpendicular directions. As long as $B_{\parallel}$ is dominant with respect to the perpendicular magnetic field, the classification into the parallel and perpendicular diffusion coefficient is reasonable. The findings suggest that the classification is reasonable for values up to ratios b/B close to 2.

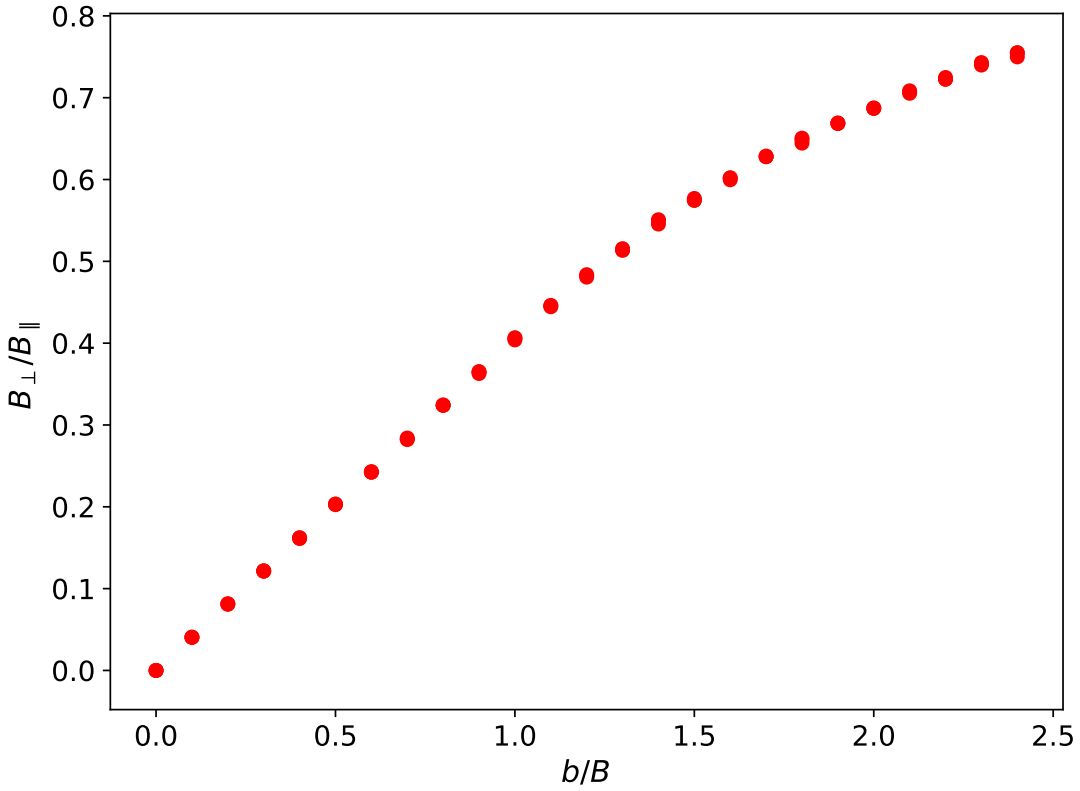

Figure F.3: Ratio of magnetic field components as functions of the ratio $\frac{b}{B}$ based on the numerical calculations in Fig. F.1. This plot indicates the range of b/B for which $B_{\parallel}$ is distinguishable from $B_{\perp}$.

In Fig. (F.1) and Fig. (F.3) it can be seen that $B_{\mathrm{tot}} \approx B$ and the parallel magnetic field magnitude $B_{\mathrm{tot},3}$ dominates the perpendicular field magnitude $B_{\mathrm{tot},1}$ for $b/B \lesssim 2$. This is obviously no strict cut off but seems to work well in he presented fits in Chapters 4 and 5. Consequently, the definition of the gyroradius presented in Equ. (F.1) coincide with the definition in Equ. (F.3).

G | Diffusion Coefficients as Functions of Energy and Magnetic Field Configuration

The following two figures present the diffusion coefficients as functions of the particle energy as well as the ratio b/B. Even though the uncertainties are high because of only considering few particles (1200), a clear trend is indicated. Increasing the the energy, increases both the parallel and the perpendicular components of the diffusion coefficient. However, increasing the ratio b/B increases the parallel component and decreases the perpendicular component. This is expected from theoretical predictions (see Chapter 2 and table 4.1 for more information). Chapter 4 aims at testing theoretical predictions against simulated data with high accuracy.

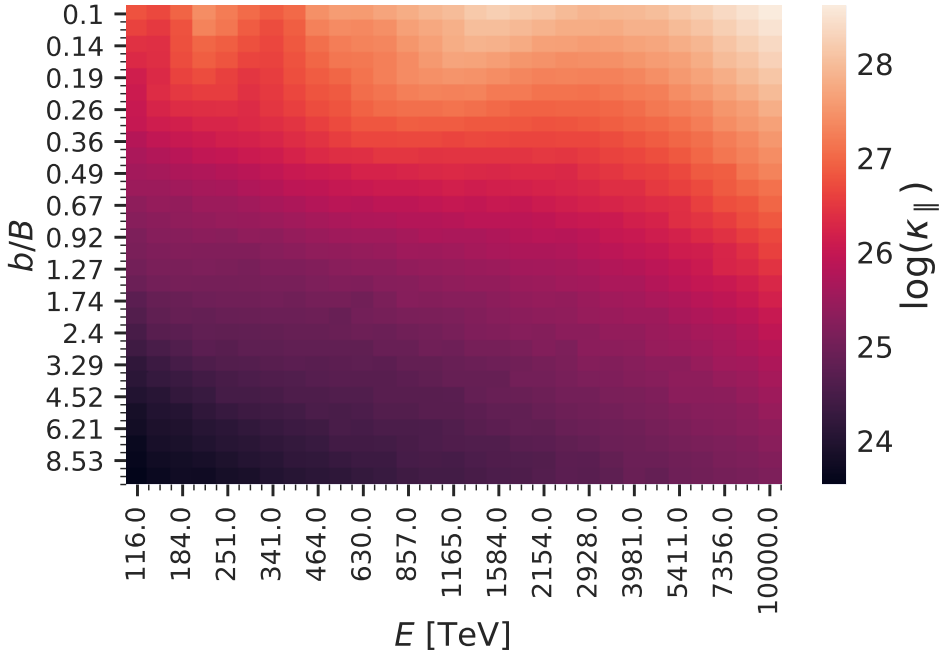

Figure G.1: Parallel diffusion coefficients as functions of the particle energy as well as the ratio b/B. The parallel diffusion coefficients are in units of $[\mathrm{cm}^2/\mathrm{s}]$.

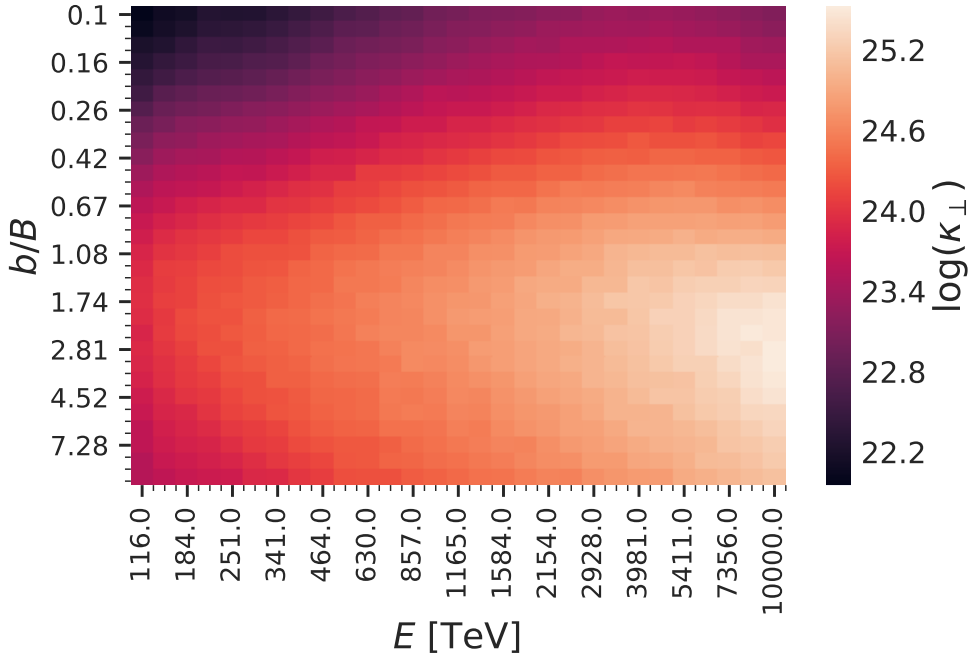

Figure G.2: Perpendicular diffusion coefficients as functions of the particle energy as well as the ratio b/B. The perpendicular diffusion coefficients are in units of [cm^2/s].

H | Simulated Particle Distributions

Diffusive transport from a point source leads to a Gaussian distribution of the pitch angle averaged particle density in all three dimensions (see Section 2.1.2 and Appendix C for more details).

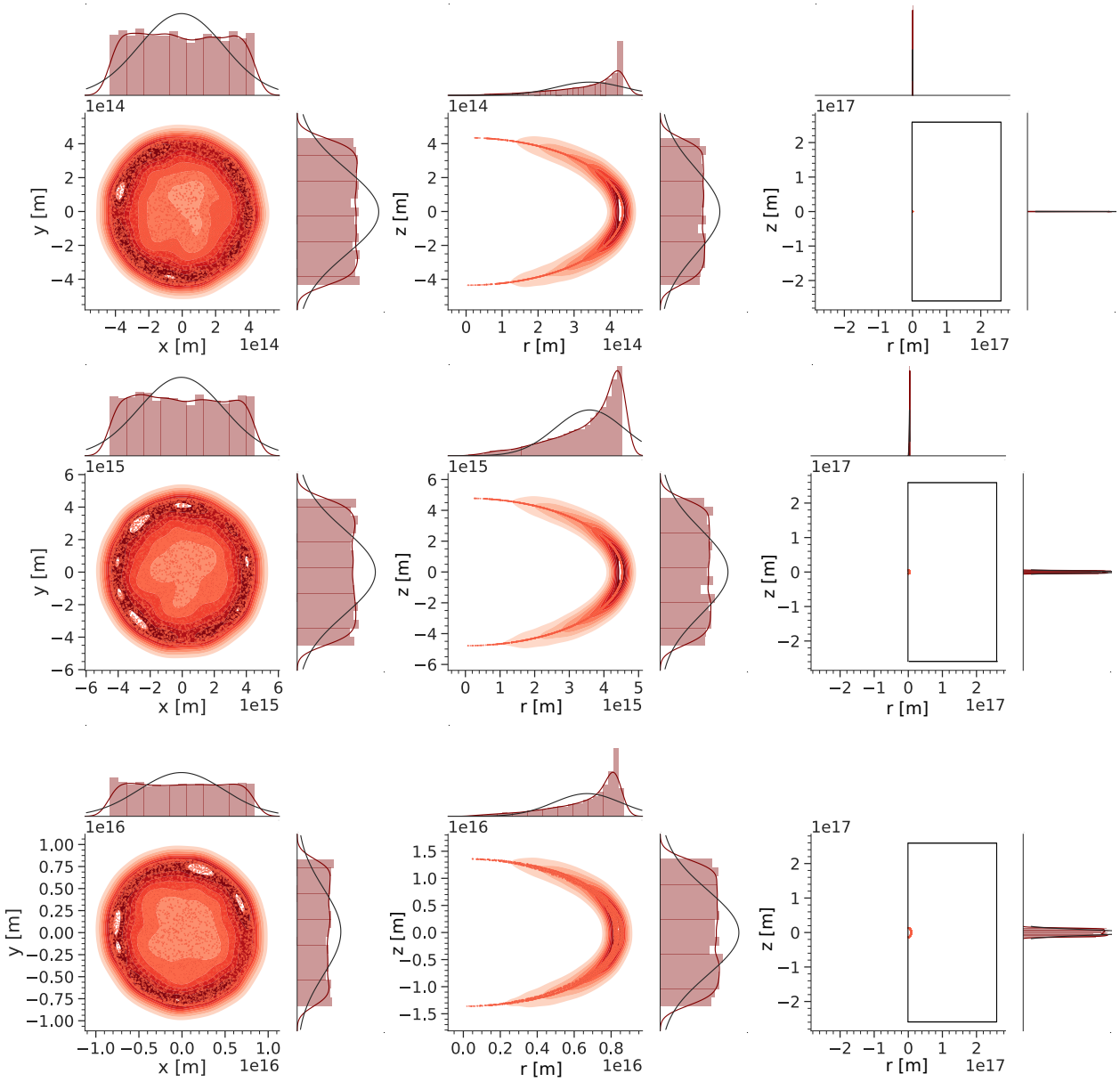

Figure H.1: Particle distributions after different number of gyrations. *Left panel*: Distributions are presented in the perpendicular components. *Middle* and *right panel*: The parallel component of the particle distribution against the radial distance to the center r in the perpendicular plane. The diffusion coefficients are calculated based on the different Gaussian fits according to Equ. (H.2) and presented in Fig H.4 and H.5.

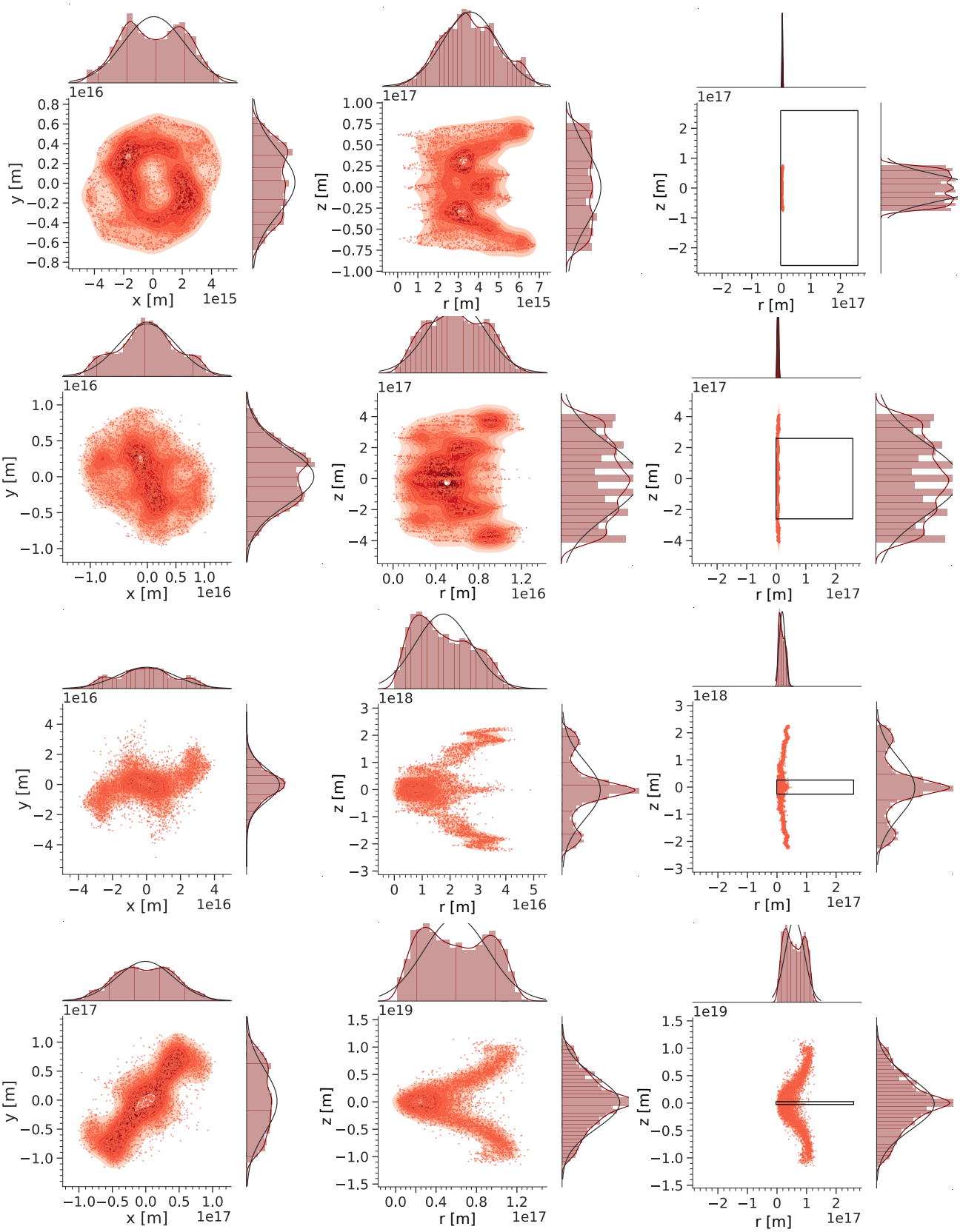

Figure H.2: Particle distributions after different number of gyrations. *Left panel*: Distributions are presented in the perpendicular components. *Middle* and *right panel*: The parallel component of the particle distribution against the radial distance to the center r in the perpendicular plane.

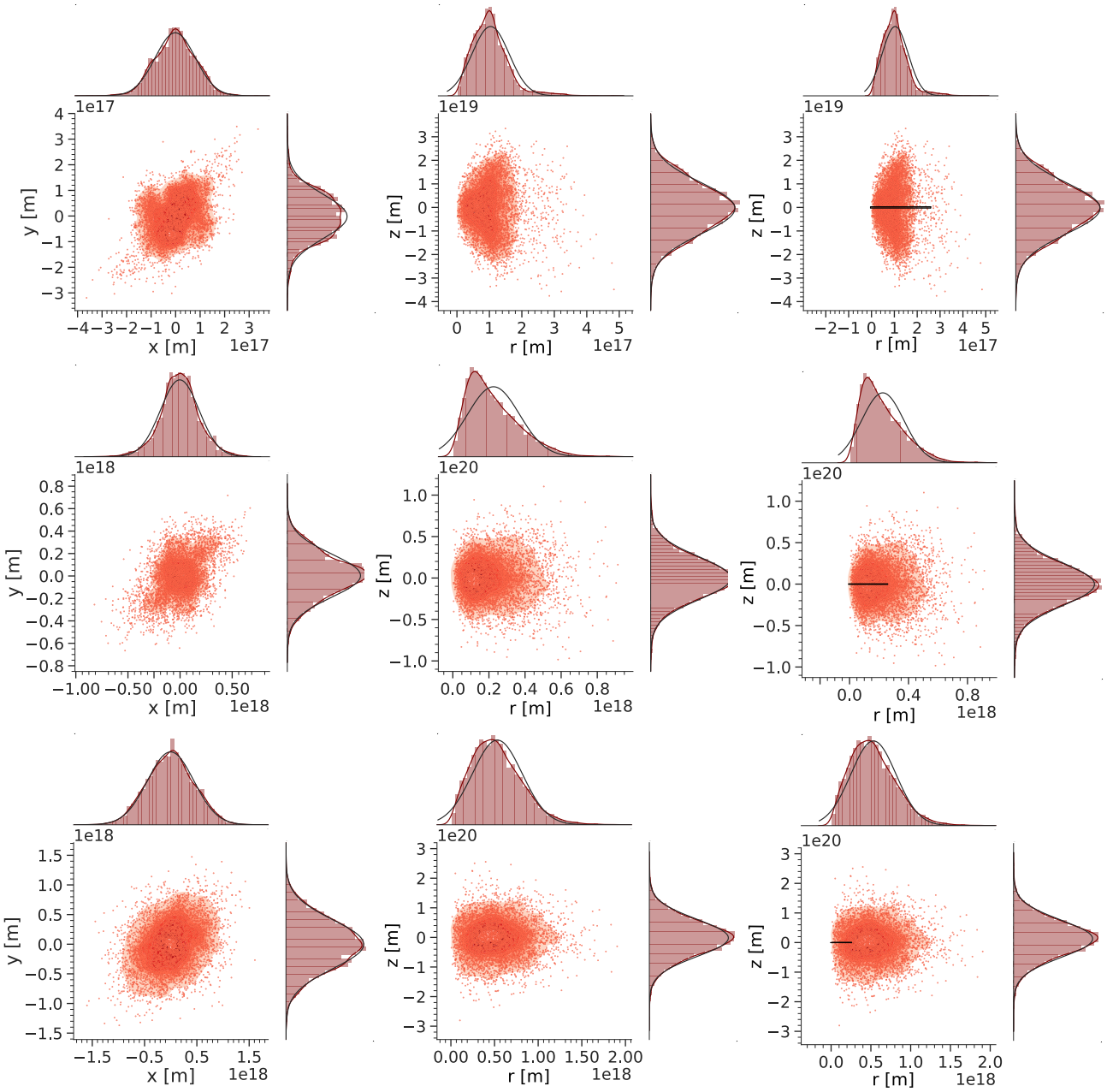

Figure H.3: Particle distributions after different number of gyrations. *Left panel*: Distributions are presented in the perpendicular components. *Middle* and *right panel*: The parallel component of the particle distribution against the radial distance to the center r in the perpendicular plane.

A point-like source as the initial condition of the problem is represented by a *Dirac Delta* distribution at $t = 0$

$$M(x_i', 0) = \delta(x_i'). \tag{H.1}$$

This condition simplifies the differential Equ. (2.19) and results in a distribution in the limit of $1 \ll t$ of the form

$$M(x_i, t) = \frac{1}{2\sqrt{\pi \kappa_{ii} t}} \exp\left(-\frac{x_i^2}{4\kappa_{ii} t}\right). \tag{H.2}$$

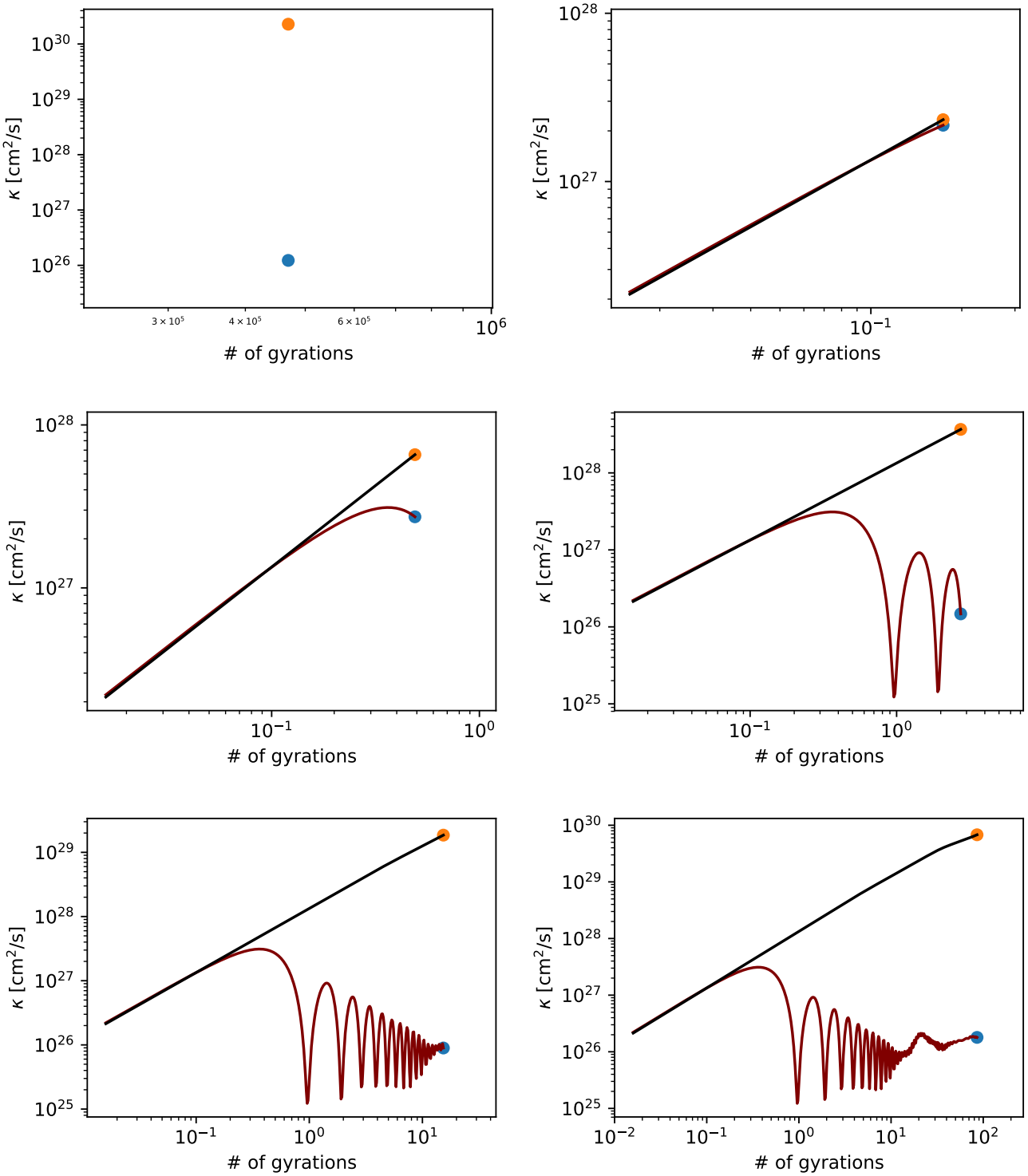

Figure H.4: Parallel (black) and perpendicular (red) diffusion coefficients as functions of the number of gyrations at different trajectory lengths (measured in number of gyrations) of the particles. These components are calculate according to Equ. (H.2) based on the distributions presented in Fig. H.1, H.2 and H.3.

This effect is illustrated in the Fig. H.1, H.2 and H.3 for 4800 particles with $E = 130$ TeV, $b/B = 0.1$ and $R_g = 0.141$ pc. The spatial particle distributions are presented together with Gaussian fits. The left panel presents the distributions in the perpendicular components. The middle and the right panel show the parallel component of the particle distribution against the radial distance to the center

$r = \sqrt{x^2 + y^2}$ in the perpendicular plane. In the right panel, the simulation volume is presented. The fit results are used for the calculation of the parallel and perpendicular diffusion coefficients according to Equ. (H.2) for the different numbers of gyrations. Each presented particle distribution in Fig. H.1, H.2 and H.3 corresponds to a parallel and a perpendicular diffusion coefficient presented within one subplot in the Fig. H.4 and Fig. H.5. The parallel and perpendicular running diffusion coefficients are presented in Fig. H.4 and Fig. H.5 as functions of the number of gyrations.

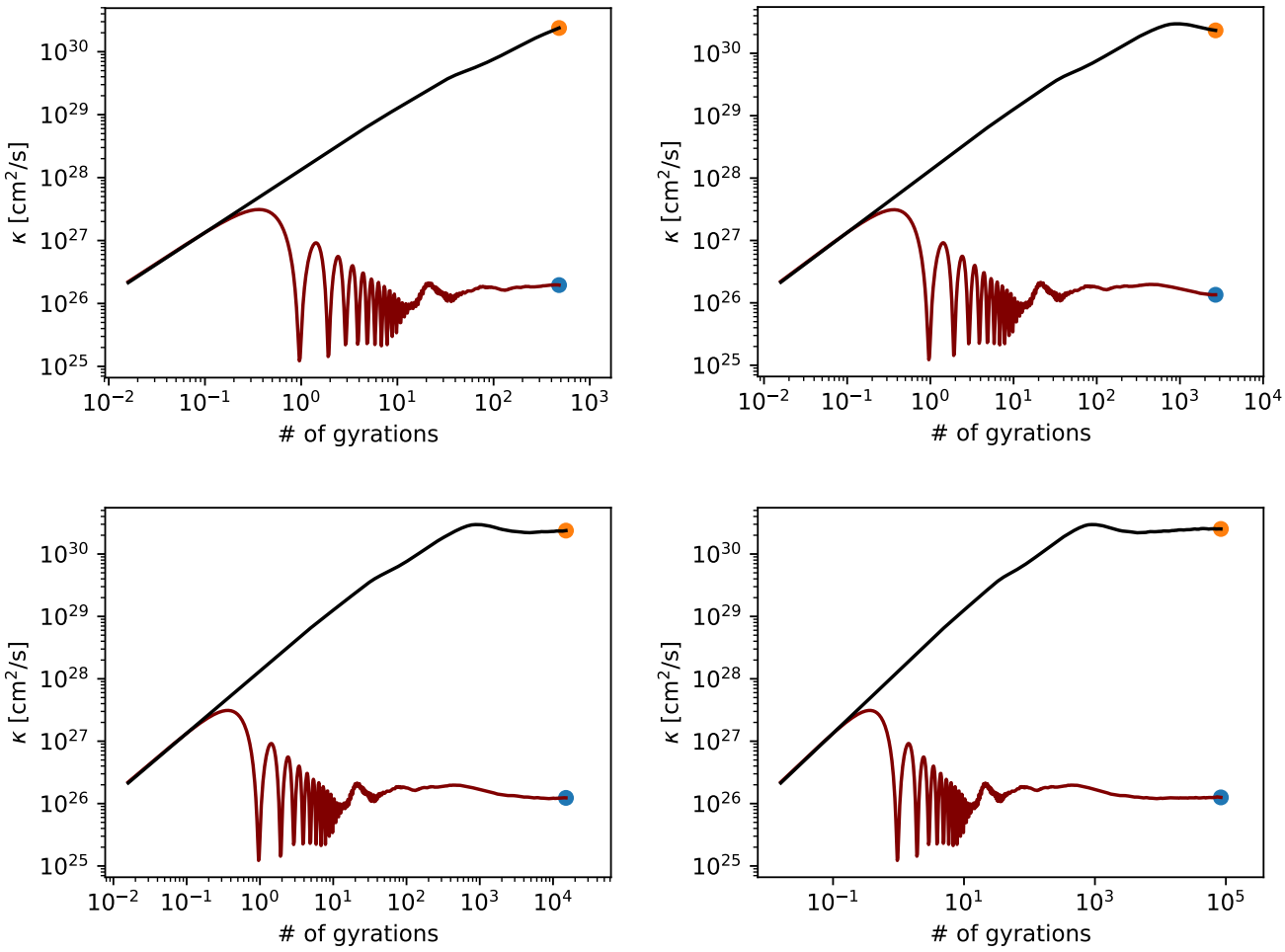

Figure H.5: Parallel (black) and perpendicular (red) diffusion coefficients as functions of the number of gyrations at different trajectory lengths (measured in number of gyrations) of the particles. These components are calculate according to Equ. (H.2) based on the distributions presented in Fig. H.1, H.2 and H.3.

I | Influence of Diffusion Coefficients on the Number of the Grid Points

In the following figures, the running parallel diffusion coefficients are presented as functions of the number of gyrations. Simulations with different numbers of particles are indicated with different colors. The wiggling of the running diffusion coefficient is due to an insufficient number of particles. An increased number of particles does not only stabilize the plateau, but also helps to find the exact transition between an increasing running diffusion coefficient and its plateau. The simulation parameters yield $l_{\text{low}} = 1.7\text{pc}$, $l_{\text{high}} = 82.45\text{pc}$, $s_{\text{spacing}} = 0.17\text{pc}$, $N_{\text{grid}} = 1024$, $N_{\text{time}} = 100000$, $b = 0.1\mu\text{G}$ and $B = 1\mu\text{G}$. The behavior for different energies is investigated.

Energy of Particles: 10000 TeV

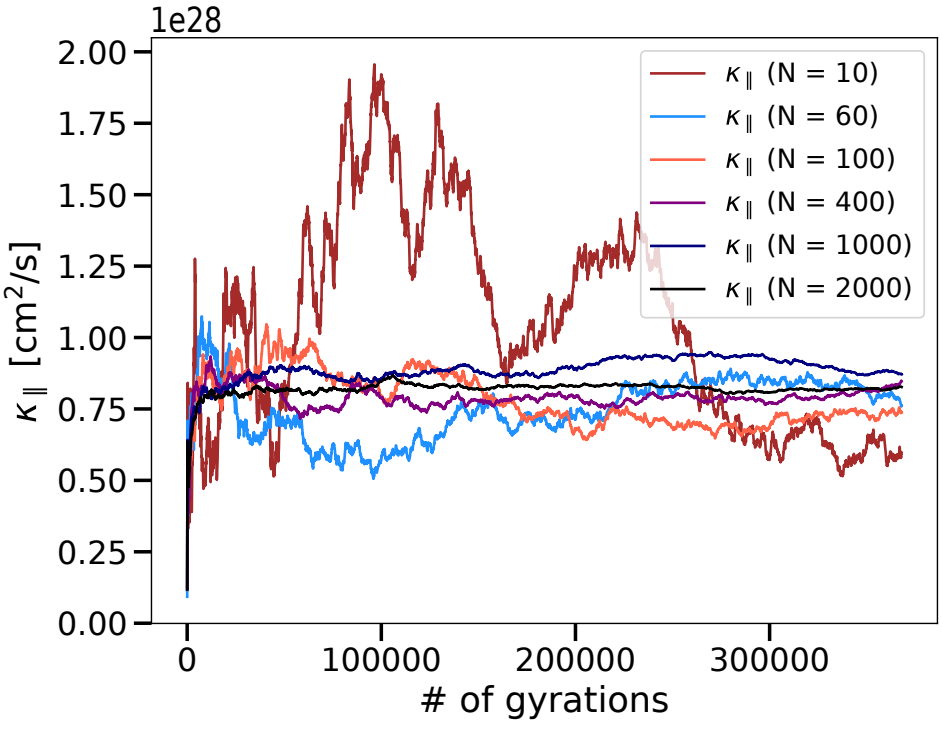

Figure I.1: Running diffusion coefficient for simulations with different number of grid points and particles with $E = 10000$ TeV in a lin-lin plot. Simulated with $l_{\text{low}} = 1.7\text{pc}$, $l_{\text{high}} = 82.45\text{pc}$, $s_{\text{spacing}} = 0.17\text{pc}$, $N_{\text{grid}} = 1024$, $N_{\text{time}} = 100000$, $b = 0.1\mu\text{G}$ and $B = 1\mu\text{G}$.

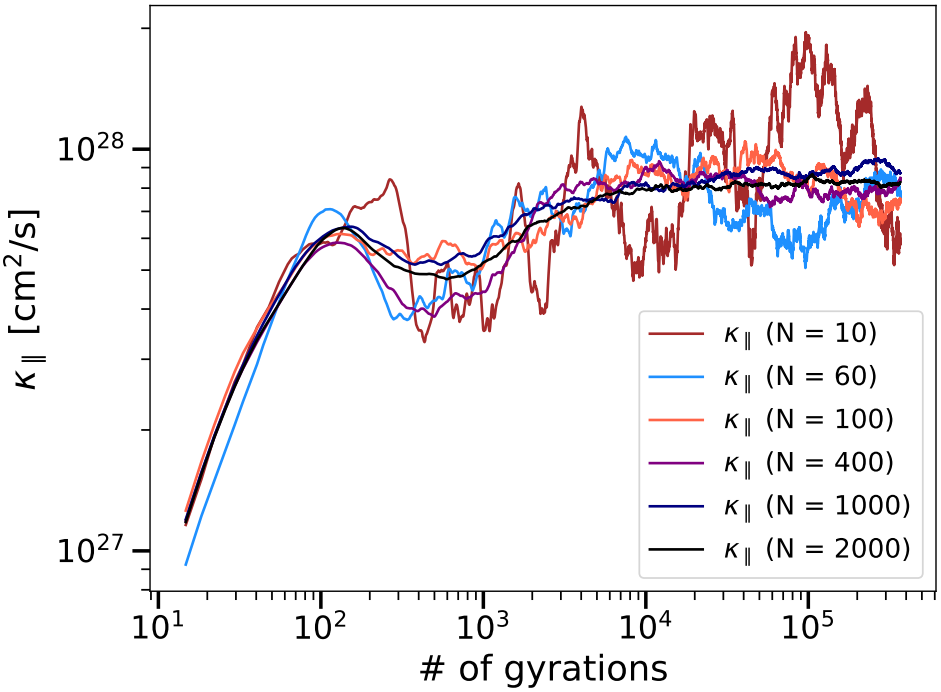

Figure I.2: Running diffusion coefficient for simulations with different number of grid points and particles with $E = 10000$ TeV in a log-log plot. Simulated with $l_{\text{low}} = 1.7$pc, $l_{\text{high}} = 82.45$pc, $s_{\text{spacing}} = 0.17$pc, $N_{\text{grid}} = 1024$, $N_{\text{time}} = 100000$, $b = 0.1\mu$G and $B = 1\mu$G.

Energy of Particles: 1000000 TeV

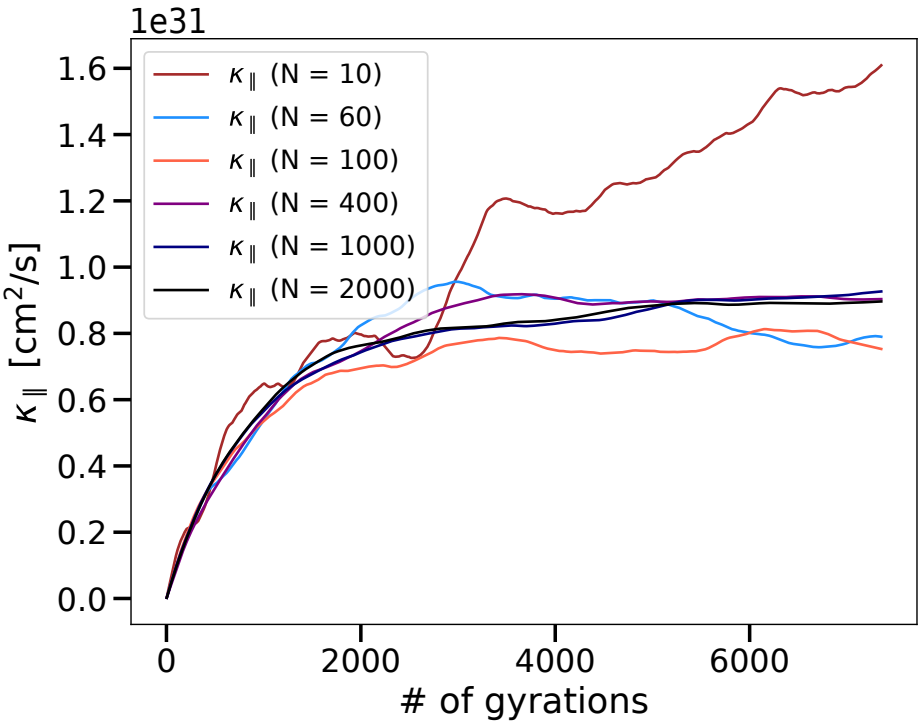

Figure I.3: Running diffusion coefficient for simulations with different number of grid points and particles with $E = 1000000$ TeV in a lin-lin plot. Simulated with $l_{\text{low}} = 1.7$pc, $l_{\text{high}} = 82.45$pc, $s_{\text{spacing}} = 0.17$pc, $N_{\text{grid}} = 1024$, $N_{\text{time}} = 100000$, $b = 0.1\mu$G and $B = 1\mu$G.

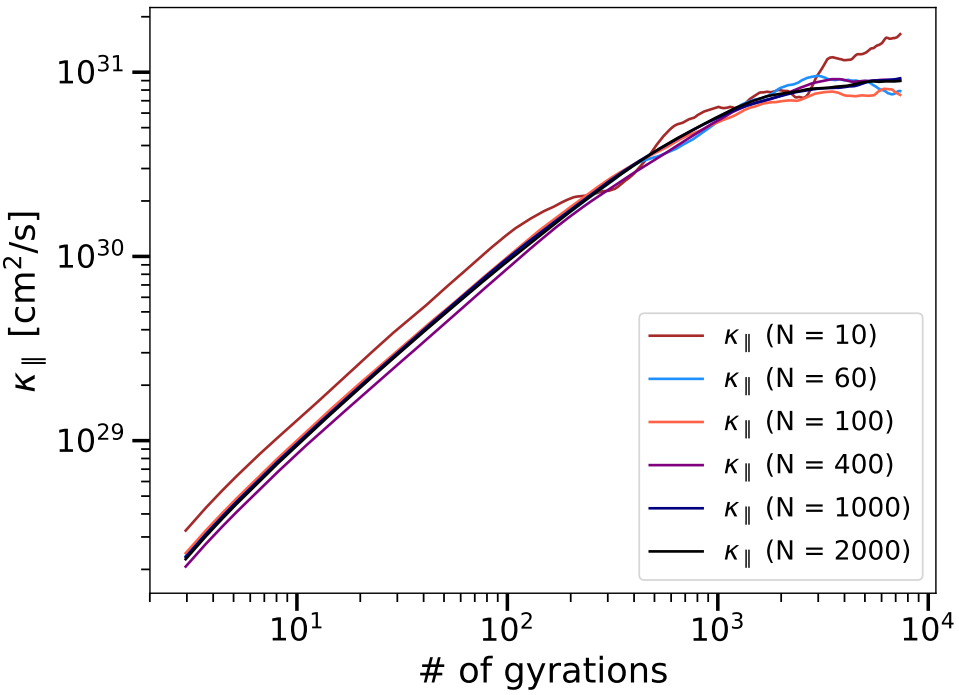

Figure I.4: Running diffusion coefficient for simulations with different number of grid points and particles with $E = 1000000$ TeV in a log-log plot. Simulated with $l_{\text{low}} = 1.7$pc, $l_{\text{high}} = 82.45$pc, $s_{\text{spacing}} = 0.17$pc, $N_{\text{grid}} = 1024$, $N_{\text{time}} = 100000$, $b = 0.1\mu$G and $B = 1\mu$G.

J | Scattering Regimes

Fig. J.1 presents in the lower panel an graphical illustration of the gyroresonance condition for the given range of plasma wavelengths in the simulations (see Section 3.3.2 for more details). The black line illustrates the upper boundary of the gyroresonance condition is fulfilled for ratios of $R_{\rm g}/l_{\rm corr} \lesssim 5/(2\pi)$. This range is indicated with the thick black line. In order to scatter resonantly around $|\mu| \approx 0$, the right hand side of the gyroresonance condition (3.12) has to be smaller than 0.06 according to Equ. (3.16) (approximated for $b \ll B = 1$). This condition is presented with the green horizontal line. This condition is satisfied for the different values of $l_{\rm low}$ for different ranges of the ratio $R_{\rm g}/l_{\rm corr}$ as presented with the thick colored lines.

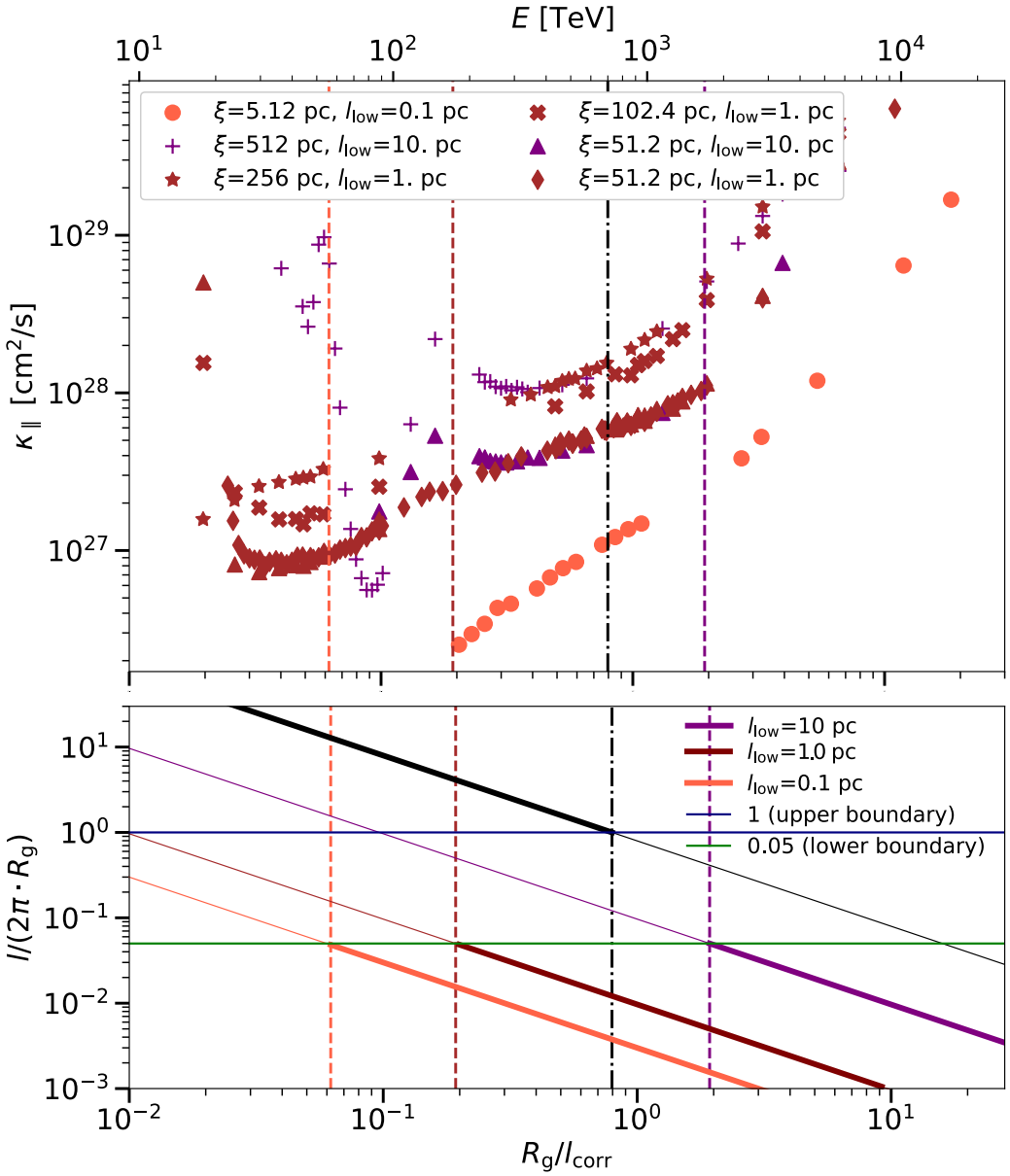

Figure J.1: Only for this plot it is used $\xi = N_{\mathrm{grid}} \cdot s_{\mathrm{spacing}}$. *Upper panel*: Parallel diffusion coefficients as functions of the ratio $R_{\mathrm{g}}/l_{\mathrm{corr}}$ for $l_{\mathrm{low}} = 1$ pc, $l_{\mathrm{high}} = 82.45$ pc. The different regimes are calculated with the equations provided in the text as shown in the lower panel. *Lower panel*: Illustration of Equ. (3.13). In order to scatter resonantly around $|\mu| \approx 0$, the right hand side of the gyroresonance condition (3.12) has to be smaller than 0.06 according to Equ. (3.16) (approximated for $b \ll B = 1$). Different colors indicate different values of l_{low}.

K | Mirror Effect

Section 3.3.2 introduces two criteria for mirroring effects. The second criterion yields

$$B_1 > B_0 \cdot \left(\frac{v}{v_\perp}\right)^2. \tag{K.1}$$

Figure K.1 presents a particle that was injected with the value $\mu = \cos(\phi_0) = 0.5$. Different relevant quantities related to mirror effects as functions of the number of gyrations are presented. The value of the right side term of the inequality (K.1) is depicted in Fig. K.1 to color the upper two subplots. The color in those subplots represents the minimum B_1 which is then needed for mirroring. Low values mean a higher probability of mirroring. The third subplot presents the magnetic moment as a function of the number of gyrations. The last subplot summarizes the first two subplots. It indicates if the inequality (3.15) is fulfilled.

In Section 3.3.2, a zoom into the transition from $\mu = \cos(\phi_0) \approx 0.5$ to $\mu \approx -0.5$ is presented in Fig. 3.15. It shows that the magnetic moment of the particle is conserved (last subplot) and that the criterion (3.15) is fulfilled (third subplot). Consequently, both criteria for mirroring are fulfilled. This behavior is only barely visible in Fig. K.1. However, the stable value of μ at around 0.5 for the first few thousand gyrations and around -0.5 afterwards is highlighted.

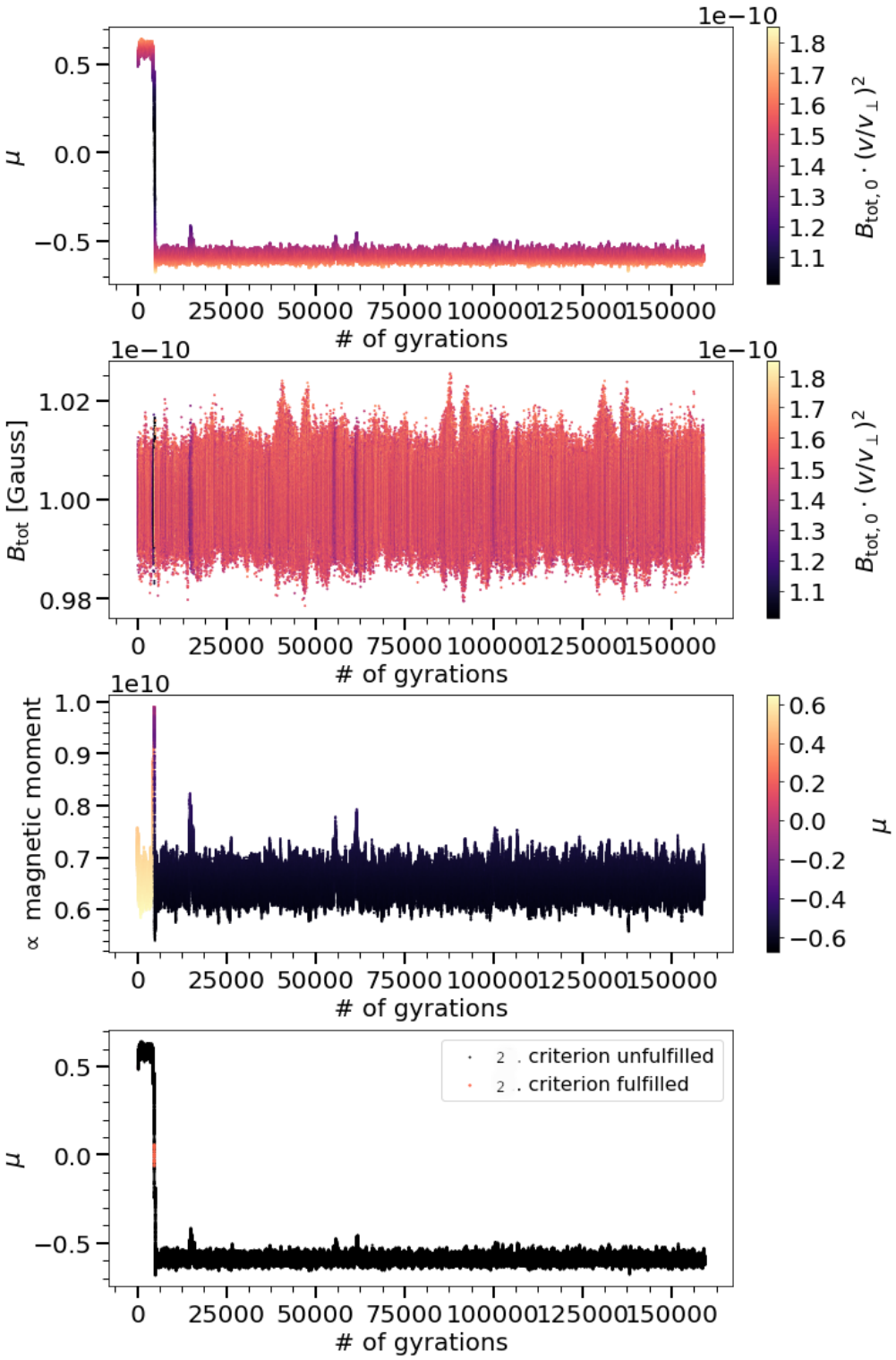

Figure K.1: The value of the right side term of the inequality (3.15) is depicted in the upper two subplots. The third subplot presents the magnetic moment as a function of the number of gyrations. The last subplot summarizes the first two subplots. It indicates if the inequality (K.1) is fulfilled which is the first criterion for mirroring. The second criterion (3.15) is fulfilled as long as the magnetic moment is constant. Simulated with $R_g = 0.109$ pc, $b/B = 0.01$ and $l_{low} = 0.04$ pc.

L | Fitting Simulated Diffusion Coefficients

The influence of the magnetic field configuration is investigated in Chapter 4. The parallel (*left panel*) and perpendicular (*right panel*) components are presented as functions of b/B in Fig. 4.3. According to the theoretical predictions for $b \ll B$ presented in table 4.1, a power-law dependency between the parallel diffusion coefficient and the ratio b/B is expected. This motivates linear fits in the log-log plots shown in Fig. 4.3. The calculated slopes together with their standard derivations are presented in table L.1 and plotted as a function of the ratio b/B in Fig. 4.4. Only fits are evaluated up to ratios of $R_{\mathrm{g}}/l_{\mathrm{corr}}$ at around 2 as expected based on the discussion in Appendix F.

Table L.1: This table presents the ranges of b/B which were used in Fig 4.3 and Fig. 4.5 to fit the data. As discussed in Appendix F, ratio up to $b/B \lesssim 2$ are taken into account. The fitted slopes are calculate with their uncertainties and presented in the table as well as in Fig. 4.4 and Fig. 4.5 as functions of $R_{\mathrm{g}}/l_{\mathrm{corr}}$.

E [PeV]	b_{min}	b_{max}	slope for $\kappa_{\parallel}$	slope for $\kappa_{\perp}$	slope for $\kappa_{\perp}/\kappa_{\parallel}$
5	0.108	2.395	-1.834 ± 0.033	0.958 ± 0.016	3.038 ± 0.015
8	0.025	2.395	-1.874 ± 0.014	1.081 ± 0.021	3.000 ± 0.018
10	0.032	2.395	-1.838 ± 0.017	1.119 ± 0.029	2.976 ± 0.016
11	0.052	2.395	-1.816 ± 0.013	1.132 ± 0.028	2.993 ± 0.021
11	0.052	2.395	-1.803 ± 0.020	1.147 ± 0.038	2.989 ± 0.024
12	0.041	1.887	-1.812 ± 0.016	1.145 ± 0.038	2.971 ± 0.026
40	0.018	2.395	-1.785 ± 0.015	1.361 ± 0.058	2.966 ± 0.095
50	0.018	2.395	-1.727 ± 0.047	1.439 ± 0.046	2.986 ± 0.095
63	0.052	2.395	-1.922 ± 0.004	1.606 ± 0.032	3.156 ± 0.075
79	0.085	2.395	-1.873 ± 0.015	1.651 ± 0.039	3.357 ± 0.089
100	0.108	2.395	-1.900 ± 0.018	1.576 ± 0.065	3.553 ± 0.058
200	0.137	2.395	-1.946 ± 0.008	1.937 ± 0.012	3.894 ± 0.020
300	0.137	2.395	-1.969 ± 0.003	1.947 ± 0.011	3.934 ± 0.008
500	0.085	2.395	-1.969 ± 0.003	1.961 ± 0.008	3.942 ± 0.008
2000	0.067	2.395	-1.975 ± 0.002	1.965 ± 0.007	3.955 ± 0.006
5000	0.174	2.395	-1.951 ± 0.006	1.934 ± 0.014	3.901 ± 0.010

The diffusion coefficients energy dependencies are investigated in Chapter 4 and summarized in table L.2. Data points are fitted with a linear fit in the log-log representation in each of the three different regimes. The fits are presented in table L.2 and shown as a function of the ratio b/B in Fig. 4.11 for

the parallel diffusion coefficients (left side) and for the perpendicular diffusion coefficients (right side).

Table L.2: For the diffusive-energy regime with the energy range 8 PeV $\leq E \leq$ 11.5 PeV, corresponding to $0.33 \leq R_g/l_{corr} \leq 0.76$, the range $0.052 \leq b/B \leq 20$ is investigated. The data points are fitted with a linear fit in the log-log representation in Fig. 4.6 with the slopes listed below for the parallel components. The simulation results for the intermediate-energy regime (see Fig 4.8) and the high-energy regime (see Fig. 4.9) are also shown below. The calculated slopes are presented in Fig 4.11.

b/B	E [PeV]*	slope	E [PeV]†	slope	E [PeV]‡	slope
0.025	$8-11.5$	–	$40-100$	–	$200-5,000$	–
0.033	$8-11.5$	–	$40-100$	–	$200-5,000$	–
0.041	$8-11.5$	–	$40-100$	–	$200-5,000$	–
0.052	$8-11.5$	0.465 ± 0.074	$40-100$	–	$200-5,000$	–
0.067	$8-11.5$	0.547 ± 0.170	$40-100$	–	$200-5,000$	–
0.108	$8-11.5$	0.598 ± 0.025	$40-100$	1.858 ± 0.105	$200-5,000$	–
0.137	$8-11.5$	0.647 ± 0.022	$40-100$	1.889 ± 0.071	$200-5,000$	1.018 ± 0.024
0.174	$8-11.5$	0.641 ± 0.028	$40-100$	1.974 ± 0.034	$200-5,000$	0.984 ± 0.022
0.221	$8-11.5$	0.693 ± 0.012	$40-100$	1.934 ± 0.053	$200-5,000$	–
0.280	$8-11.5$	0.709 ± 0.020	$40-100$	–	$200-5,000$	–
0.356	$8-11.5$	0.747 ± 0.024	$40-100$	–	$200-5,000$	–
0.573	$8-11.5$	–	$40-100$	1.727 ± 0.025	$200-5,000$	–
0.727	$8-11.5$	–	$40-100$	1.699 ± 0.011	$200-5,000$	0.982 ± 0.025
0.923	$8-11.5$	0.988 ± 0.112	$40-100$	1.728 ± 0.030	$200-5,000$	0.986 ± 0.025
1.172	$8-11.5$	1.006 ± 0.005	$40-100$	1.711 ± 0.048	$200-5,000$	0.987 ± 0.012
1.487	$8-11.5$	0.985 ± 0.015	$40-100$	1.703 ± 0.026	$200-5,000$	0.984 ± 0.009
1.887	$8-11.5$	0.970 ± 0.020	$40-100$	1.682 ± 0.025	$200-5,000$	0.989 ± 0.008
2.395	$8-11.5$	0.913 ± 0.014	$40-100$	1.662 ± 0.017	$200-5,000$	0.986 ± 0.008
3	$8-11.5$	–	$40-100$	1.599 ± 0.032	$200-5,000$	–
4	$8-11.5$	0.909 ± 0.020	$40-100$	1.463 ± 0.051	$200-5,000$	–
5	$8-11.5$	0.873 ± 0.006	$40-100$	1.357 ± 0.044	$200-5,000$	–
6.21	$8-11.5$	0.868 ± 0.017	$40-100$	–	$200-5,000$	0.983 ± 0.017
7.88	$8-11.5$	0.846 ± 0.010	$40-100$	1.244 ± 0.023	$200-5,000$	–
10	$8-11.5$	0.831 ± 0.011	$40-100$	–	$200-5,000$	–
11	$8-11.5$	0.832 ± 0.020	$40-100$	1.102 ± 0.024	$200-5,000$	–
12	$8-11.5$	0.803 ± 0.015	$40-100$	1.048 ± 0.012	$200-5,000$	–
13	$8-11.5$	0.808 ± 0.022	$40-100$	1.087 ± 0.018	$200-5,000$	–
14	$8-11.5$	0.849 ± 0.026	$40-100$	–	$200-5,000$	–
16	$8-11.5$	0.796 ± 0.015	$40-100$	–	$200-5,000$	–
20	$8-11.5$	0.768 ± 0.013	$40-100$	–	$200-5,000$	–

* The energy range corresponds to $0.33 \leq R_g/l_{corr} \leq 0.76$ (diffusive-energy regime).
† The energy range corresponds to $2.62 \leq R_g/l_{corr} \leq 6.55$ (intermediate-energy regime).
‡ The energy range corresponds to $13.10 \leq R_g/l_{corr} \leq 327.58$ (high-energy regime).

M | Analysis of Data from Other Papers

The following plots present in each left panel data from studies as indicated in the caption. The parallel diffusion coefficients are presented as functions of the ratio R_g/l_{corr}. The upper boundary of the diffusive-energy regime is presented with the black line according to Equ. (3.18). In the right panels, each fit starts with the ratio shown on the x-axis in the right panel and ends at the value closest to the upper boundary, while taking all values in between into account. The calculated slopes labeled with the text *2 points* result from the fits with the thick solid line in the left panel. The calculated slopes indicated with the text *all points* result from the fits using all data points within the diffusive regime (the dashed lines in the left panel). These two slopes are presented in table 3.1 for all investigated ratios b/B. In addition the table summarizes all relevant simulation parameters in each publication.

As discussed in Section 3.3.2, the simulation results around $R_g/l_{corr} \approx 5/(2\pi)$ are polluted the least and therefore have to be considered for determining the slopes. Consequently, each fit starts with the ratio shown on the x-axis in the right panel and ends at the value closest to the upper border, while taking all values in between into account. A slope of 1/3, which is claimed in their publications, can only be concluded by accounting for data points that are calculated for particles, that cannot scatter resonantly anymore around $\mu \approx 0$ and in the limit $b \ll B$.

As expected from the discussion in Section 3.3.2, decreasing the ratio R_g/l_{corr} increases the number of missing scatterings, which artificially pollute the diffusion coefficients such that γ artificially decreases in the expression $\kappa_{\parallel} \propto E^{\gamma}$. This effect is indicated in the following plots.

In addition, Fig. M.6 presents simulation data from different studies as indicated in the legend. The parallel diffusion coefficients are presented as functions of the ratio R_g/l_{corr}. The upper boundary of the diffusive regime is shown at $R_g/l_{corr} = 5/(2\pi)$. All data points taken from the indicated studies are converted into the presented units except for data from [11]. Data points from [11] are shifted in the y-axis so that the data point coincide with that of the others studies at $R_g/l_{corr} = 5/(2\pi)$ because the exact conversion into the presented unit was not possible with the given information in [11]. Fig. M.7 focuses on the diffusive-energy regime. The upper subplot shows the parallel diffusion coefficients as functions of the ratio R_g/l_{corr}. In the middle subplot, the slopes of the fits within the diffusion-energy regime are presented. Each fit starts with the ratio shown on the x-axis and ends at the value closest to the upper border at $2/(5\pi)$, while taking all values in between into account. The lower subplot presents the slopes of the fits that take only the value at the ratio shown on the x-axis and the next value into account.

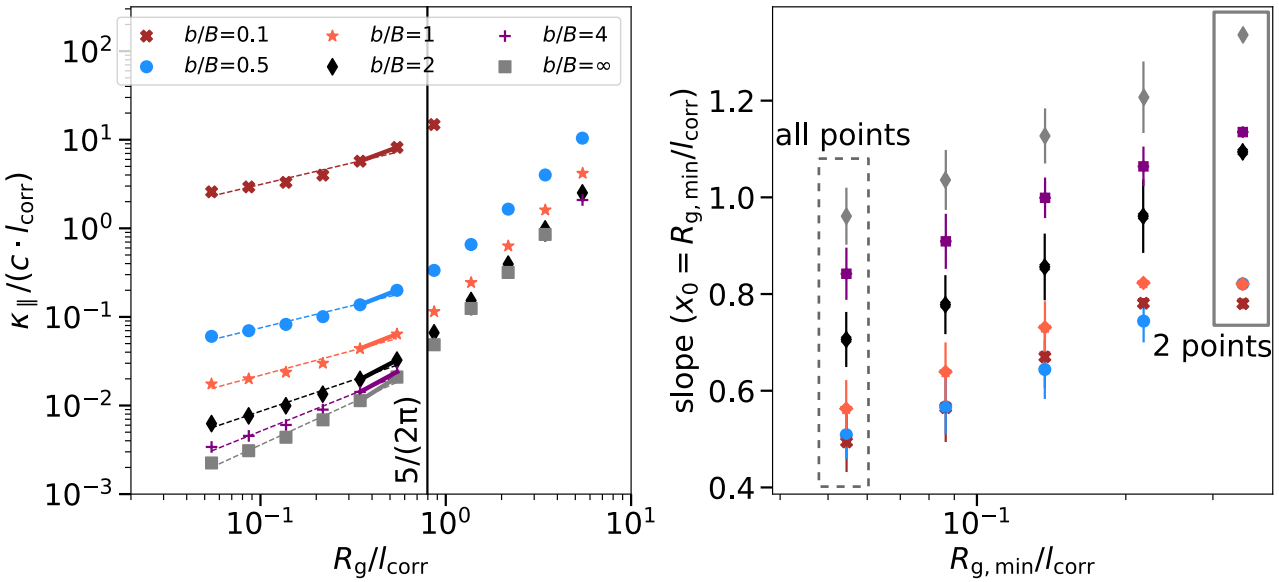

Figure M.1: *Left panel*: Analysis of resonant scattering regime based on the analysis resulting in Equ. (3.13) applied on data taken from [17]. The black line represents the upper boundary according to Equ. (3.18). The lower boundary based on Equ. (3.17) cannot be calculated with the given information. *Right panel*: The slopes of fits within the diffusion-energy regime. Each fit starts with the ratio shown on the x-axis in the right panel and ends at the value closest to the upper border, while taking all values in between into account. Decreasing the ratio R_g/l_{corr} increases the number of missing scatterings, which artificially pollute the diffusion coefficients such that γ artificially decreases in the expression $\kappa_\parallel \propto E^\gamma$.

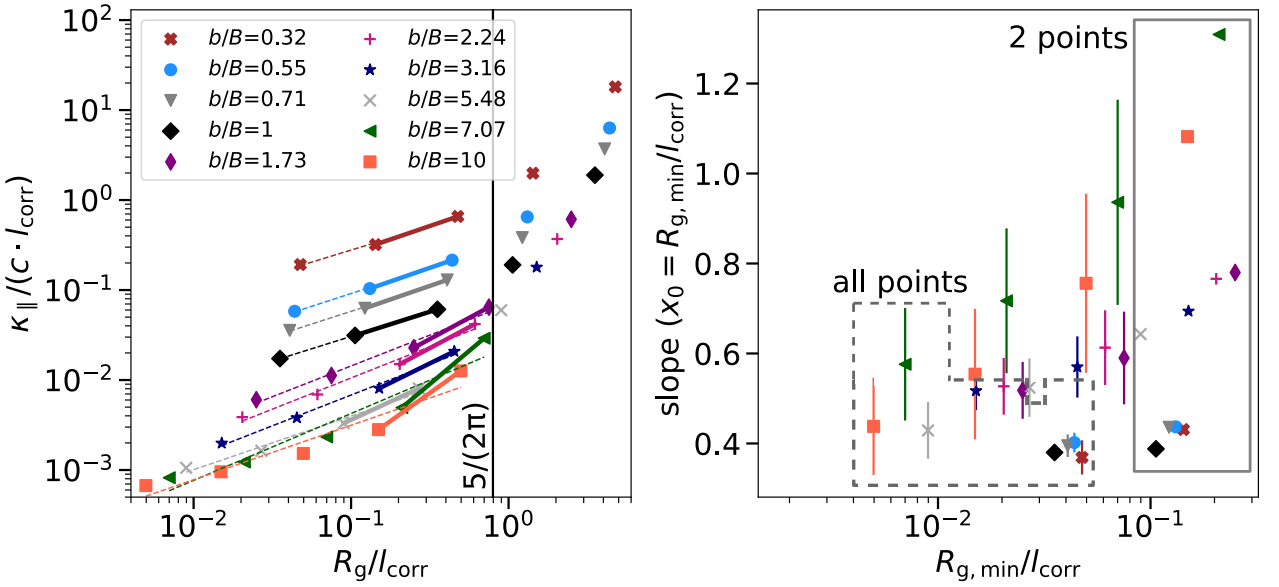

Figure M.2: *Left panel*: Analysis of resonant scattering regime based on the analysis resulting in Equ. (3.13) applied on data taken from [51]. The black line represents the upper border according to Equ. (3.18). The lower boundary based on Equ. (3.17) cannot be calculated with the given information. *Right panel*: The slopes of fits within the diffusion-energy regime. Each fit starts with the ratio shown on the x-axis in the right panel and ends at the value closest to the upper border, while taking all values in between into account.

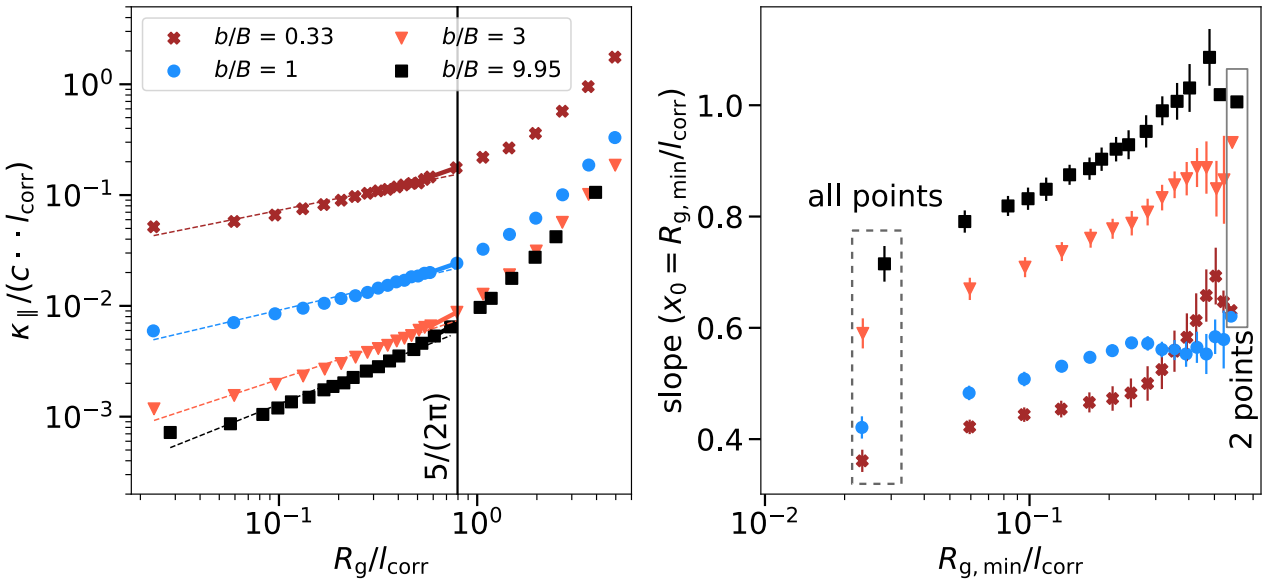

Figure M.3: *Left panel*: Analysis of resonant scattering regime based on the analysis resulting in Equ. (3.13) applied on data taken from [11]. The black line represents the upper border according to Equ. (3.18). The lower boundary based on Equ. (3.17) cannot be calculated with the given information. *Right panel*: The slopes of fits within the diffusion-energy regime. Each fit starts with the ratio shown on the x-axis in the right panel and ends at the value closest to the upper border, while taking all values in between into account. Decreasing the ratio R_g/l_{corr} increases the number of missing scatterings, which artificially pollute the diffusion coefficients such that γ artificially decreases.

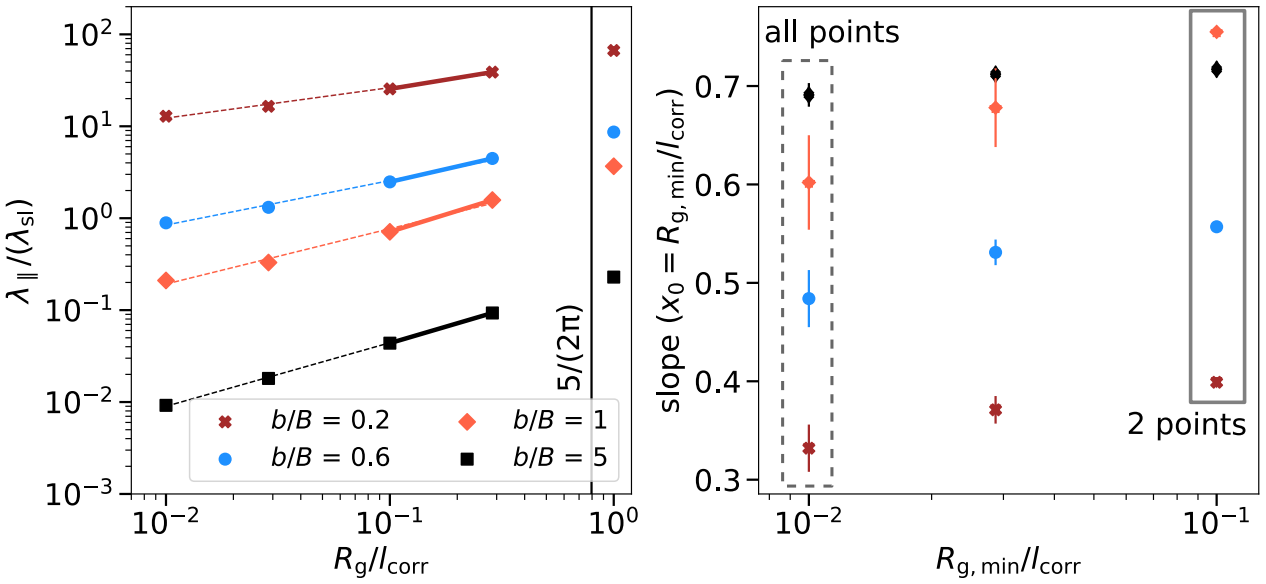

Figure M.4: *Left panel*: Analysis of resonant scattering regime based on the analysis resulting in Equ. (3.13) applied on data taken from [16]. The black line represents the upper border according to Equ. (3.18). The lower boundary based on Equ. (3.17) cannot be calculated with the given information. *Right panel*: The slopes of fits within the diffusion-energy regime. Each fit starts with the ratio shown on the x-axis in the right panel and ends at the value closest to the upper border, while taking all values in between into account. Decreasing the ratio R_g/l_{corr} increases the number of missing scatterings, which artificially pollute the diffusion coefficients such that γ artificially decreases.

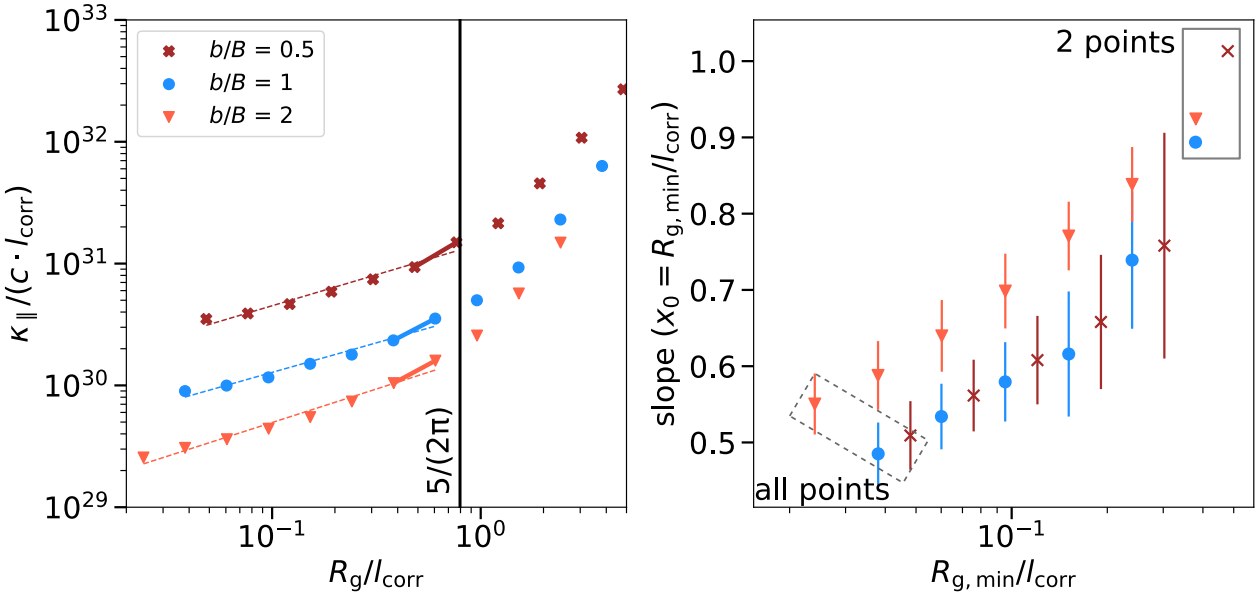

Figure M.5: *Left panel*: Analysis of resonant scattering regime based on the analysis resulting in Equ. (3.13) applied on data taken from [52]. The black line represents the upper border according to Equ. (3.18). The lower boundary based on Equ. (3.17) cannot be calculated with the given information. *Right panel*: The slopes of fits within the diffusion-energy regime. Each fit starts with the ratio shown on the x-axis in the right panel and ends at the value closest to the upper border, while taking all values in between into account. Decreasing the ratio R_g/l_{corr} increases the number of missing scatterings, which artificially pollute the diffusion coefficients such that γ artificially decreases.

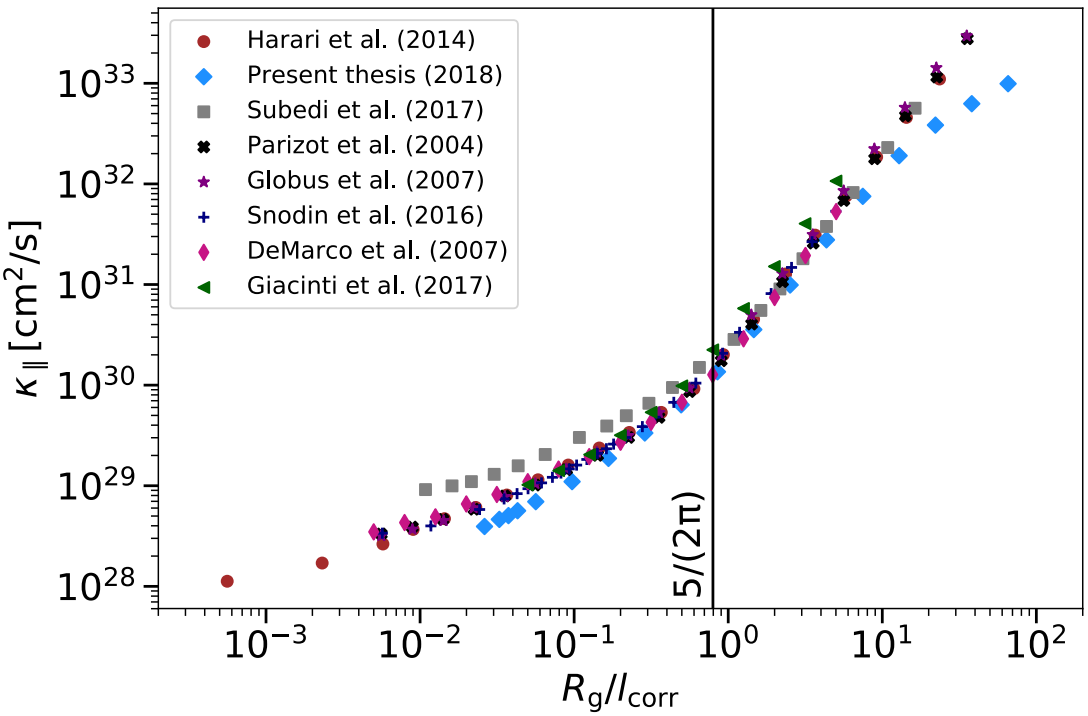

Figure M.6: Parallel diffusion coefficients as functions of the ratio R_g/l_{corr}. All data points taken from the indicated studies are converted into the presented units except for data from [11]. Data points from [11] are shifted in the y-axis so that the data point coincide with that of the others studies at $R_g/l_{corr} = 5/(2\pi)$ because the exact conversion into the presented unit was not possible with the given information in [11].

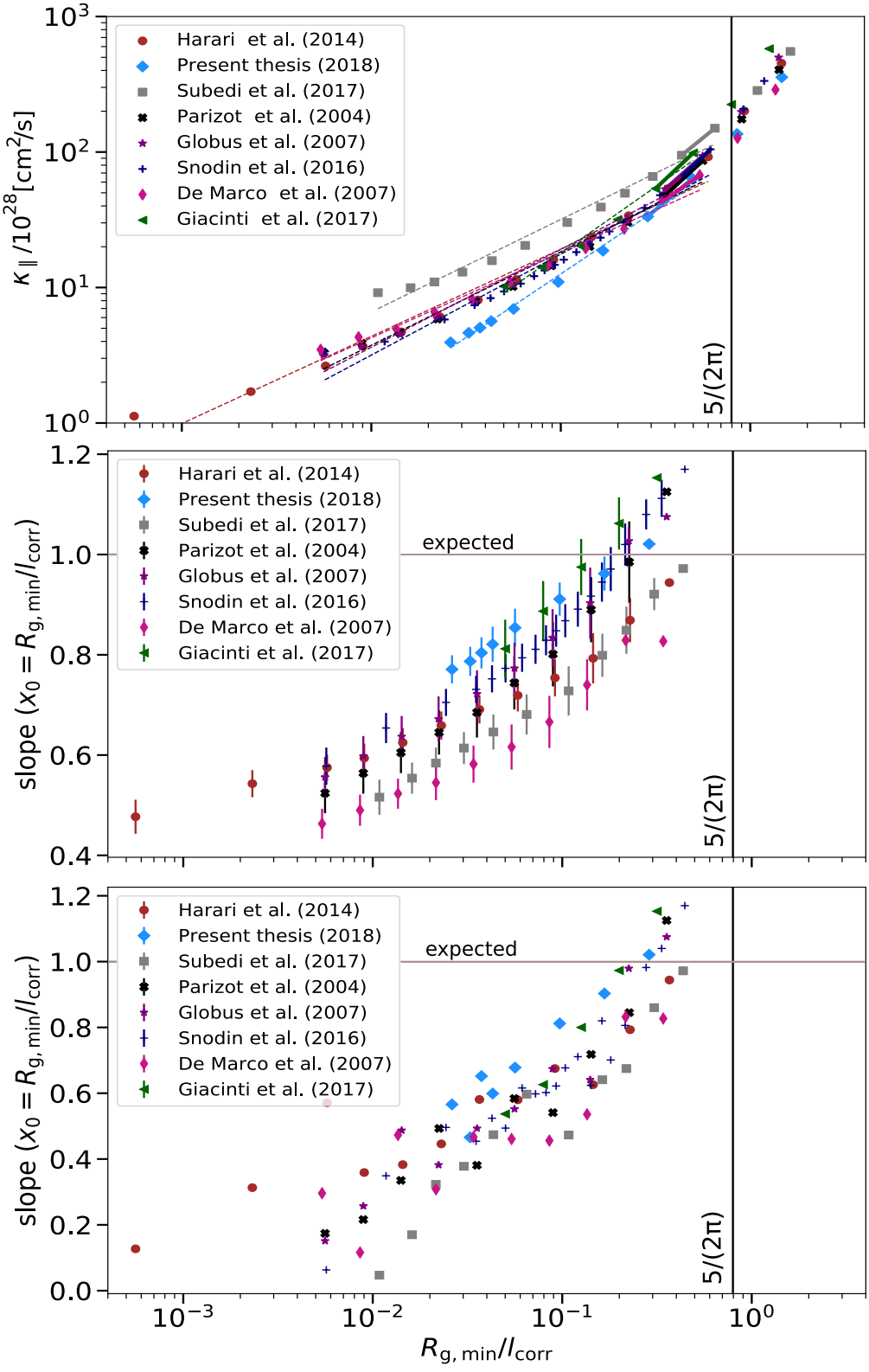

Figure M.7: *Upper panel*: Analysis of resonant scattering regime based on the analysis resulting in Equ. (3.13) applied on data taken from studies indicated in the legend (zoom of Fig. M.6 with the same conversions of units for better comparison). The black line represents the upper border according to Equ. (3.18). The lower boundaries are indicated by the dashed lines according to Equ. (3.14). *Middle panel*: The slopes of the fits within the diffusion-energy regime are presented. Each fit starts with the ratio shown on the x-axis and ends at the value closest to the upper border at $2/(5\pi)$, while taking all values in between into account. *Lower panel*: Each fit takes only the value at the ratio shown on the x-axis and the value at the next higher ratio of R_g/l_{corr} into account.

Bibliography

[1] Ellen G. Zweibel. "The microphysics and macrophysics of cosmic rays". In: 20 (May 2013).

[2] Barbara Wiebel-Sooth, Peter L. Biermann, and Hinrich Meyer. "Cosmic rays vii. individual element spectra: prediction and data". In: *Astron. Astrophys.* 330 (1998), p. 389. arXiv: astro-ph/9709253 [astro-ph].

[3] Julia K. Becker and Peter L. Biermann. "Neutrinos from active black holes, sources of ultra high energy cosmic rays". In: *Astropart. Phys.* 31 (2009), pp. 138–148. DOI: 10.1016/j.astropartphys.2008.12.006. arXiv: 0805.1498 [astro-ph].

[4] J. Abraham et al. "Measurement of the energy spectrum of cosmic rays above 10^{18} eV using the Pierre Auger Observatory". In: *Phys. Lett.* B685 (2010), pp. 239–246. DOI: 10.1016/j.physletb.2010.02.013. arXiv: 1002.1975 [astro-ph.HE].

[5] Lukas Merten et al. "The Propagation of Cosmic Rays from the Galactic Wind Termination Shock: Back to the Galaxy?" In: *The Astrophysical Journal* 859.1 (2018), p. 63. URL: http://stacks.iop.org/0004-637X/859/i=1/a=63.

[6] G. Giacinti et al. "Cosmic ray anisotropy as signature for the transition from galactic to extragalactic cosmic rays". In: *Journal of Cosmology and Astroparticle Physics* 2012.07 (2012), p. 031. URL: http://stacks.iop.org/1475-7516/2012/i=07/a=031.

[7] Pierre Auger Collaboration. "Constraints on the Origin of Cosmic Rays above 10^{18} eV from Large-scale Anisotropy Searches in Data of the Pierre Auger Observatory". In: (Jan. 2013). URL: http://adsabs.harvard.edu/abs/2013ApJ...762L..13P.

[8] Rafael Alves Batista et al. "CRPropa 3 - a Public Astrophysical Simulation Framework for Propagating Extraterrestrial Ultra-High Energy Particles". In: *JCAP* 1605.05 (2016), p. 038. DOI: 10.1088/1475-7516/2016/05/038. arXiv: 1603.07142 [astro-ph.IM].

[9] Ralf Kissmann. "PICARD: A novel code for the Galactic Cosmic Ray propagation problem". In: *Astropart. Phys.* 55 (2014), pp. 37–50. DOI: 10.1016/j.astropartphys.2014.02.002. arXiv: 1401.4035 [astro-ph.HE].

[10] Elena Orlando et al. "GALPROP cosmic-ray propagation code: recent results and updates". In: 2017. arXiv: 1712.09755 [astro-ph.HE].

[11] A. P. Snodin et al. "Global diffusion of cosmic rays in random magnetic fields". In: *Mon. Not. Roy. Astron. Soc.* 457.4 (2016), pp. 3975–3987. DOI: 10.1093/mnras/stw217. arXiv: 1509.03766 [astro-ph.HE].

[12] Lukas Merten et al. "CRPropa 3.1 – A low energy extension based on stochastic differential equations". In: 2017 (Apr. 2017).

[13] G Michalek and M Ostrowski. "Simulations of cosmic ray cross field diffusion in highly perturbed magnetic fields". In: 326 (Sept. 1997), pp. 793–800.

[14] J. Giacalone and J. R. Jokipii. "The Transport of Cosmic Rays across a Turbulent Magnetic Field". In: *The Astrophysical Journal* 520.1 (1999), p. 204. URL: http://stacks.iop.org/0004-637X/520/i=1/a=204.

[15] Fabien Casse, Martin Lemoine, and Guy Pelletier. "Transport of cosmic rays in chaotic magnetic fields". In: *Phys. Rev.* D65 (2002), p. 023002. DOI: 10.1103/PhysRevD.65.023002. arXiv: astro-ph/0109223 [astro-ph].

[16] J. Minnie et al. "On the Ability of Different Diffusion Theories to Account for Directly Simulated Diffusion Coefficients". In: *The Astrophysical Journal* 663.2 (2007), p. 1049. URL: http://stacks.iop.org/0004-637X/663/i=2/a=1049.

[17] G. Giacinti, M. Kachelriess, and D. V. Semikoz. "Reconciling cosmic ray diffusion with Galactic magnetic field models". In: *JCAP* 1807.07 (2018), p. 051. DOI: 10.1088/1475-7516/2018/07/051. arXiv: 1710.08205 [astro-ph.HE].

[18] B. Wake W. Fillius. In: (1983).

[19] Benjamin D. G. Chandran. "AGN-driven Convection in Galaxy-Cluster Plasmas". In: *The Astrophysical Journal* 632.2 (2005), p. 809. URL: http://stacks.iop.org/0004-637X/632/i=2/a=809.

[20] Dan Hooper, Tim Linden, and Alejandro Lopez. "Radio Galaxies Dominate the High-Energy Diffuse Gamma-Ray Background". In: *JCAP* 1608.08 (2016), p. 019. DOI: 10.1088/1475-7516/2016/08/019. arXiv: 1604.08505 [astro-ph.HE].

[21] Carlos Blanco and Dan Hooper. "High-Energy Gamma Rays and Neutrinos from Nearby Radio Galaxies". In: *JCAP* 1712 (2017), p. 017. DOI: 10.1088/1475-7516/2017/12/017. arXiv: 1706.07047 [astro-ph.HE].

[22] F. W. Stecker et al. "High-energy neutrinos from active galactic nuclei". In: *Phys. Rev. Lett.* 66 (21 May 1991), pp. 2697–2700. DOI: 10.1103/PhysRevLett.66.2697. URL: https://link.aps.org/doi/10.1103/PhysRevLett.66.2697.

[23] J. Becker Tjus et al. "High-energy neutrinos from radio galaxies". In: *Phys. Rev.* D89.12 (2014), p. 123005. DOI: 10.1103/PhysRevD.89.123005. arXiv: 1406.0506 [astro-ph.HE].

[24] Kohta Murase. "Active Galactic Nuclei as High-Energy Neutrino Sources". In: (2017), pp. 15–31. DOI: 10.1142/9789814759410_0002. arXiv: 1511.01590 [astro-ph.HE].

[25] ENRICO Fermi. "On the Origin of the Cosmic Radiation". In: *Phys. Rev.* 75 (8 Apr. 1949), pp. 1169–1174. DOI: 10.1103/PhysRev.75.1169. URL: https://link.aps.org/doi/10.1103/PhysRev.75.1169.

[26] A.R. Bell. "Cosmic ray acceleration". In: *Astroparticle Physics* 43 (2013). Seeing the High-Energy Universe with the Cherenkov Telescope Array - The Science Explored with the CTA, pp. 56–70. ISSN: 0927-6505. DOI: https://doi.org/10.1016/j.astropartphys.2012.05.022. URL: http://www.sciencedirect.com/science/article/pii/S0927650512001272.

[27] Sladjana Nikolić et al. "An Integral View of Fast Shocks around Supernova 1006". In: *Science* 340 (2013), pp. 45–48. DOI: 10.1126/science.1228297. arXiv: 1302.4328 [astro-ph.HE].

[28] J. G. Kirk. "First-order fermi acceleration at relativistic shock fronts". In: *Hot Spots in Extragalactic Radio Sources*. Ed. by Klaus Meisenheimer and Hermann-Josef Röser. Berlin, Heidelberg: Springer Berlin Heidelberg, 1989, pp. 241–246. ISBN: 978-3-540-46126-5.

[29] Jacek Niemiec and Michal Ostrowski. "First-order Fermi particle acceleration at relativistic shock waves with a 'realistic' magnetic field turbulence model". In: *Proceedings, 28th International Cosmic Ray Conference (ICRC 2003): Tsukuba, Japan, July 31-August 7, 2003*. [4,2015(2003)]. 2003, pp. 2015–2018. arXiv: astro-ph/0307238 [astro-ph]. URL: http://www-rccn.icrr.u-tokyo.ac.jp/icrc2003/PROCEEDINGS/PDF/498.pdf.

[30] Maria V. del Valle, E. M. de Gouveia Dal Pino, and G. Kowal. "Properties of the first-order Fermi acceleration in fast magnetic reconnection driven by turbulence in collisional magnetohydrodynamical flows". In: *Mon. Not. Roy. Astron. Soc.* 463.4 (2016), pp. 4331–4343. DOI: 10.1093/mnras/stw2276. arXiv: 1609.08598 [astro-ph.HE].

[31] A. R. Bell. "The Acceleration of cosmic rays in shock fronts. I". In: *Mon. Not. Roy. Astron. Soc.* 182 (1978), pp. 147–156.

[32] W. J. Macquorn Rankine. "On the Thermodynamic Theory of Waves of Finite Longitudinal Disturbance". In: *Philosophical Transactions of the Royal Society of London Series I* 160 (1870), pp. 277–288.

[33] Inkscape Project. *Inkscape*. Version 0.92. Mar. 4, 2011. URL: https://inkscape.org.

[34] Alexander Aab et al. "The Pierre Auger Cosmic Ray Observatory". In: *Nucl. Instrum. Meth.* A798 (2015), pp. 172–213. DOI: 10.1016/j.nima.2015.06.058. arXiv: 1502.01323 [astro-ph.IM].

[35] M. G. Aartsen et al. "The IceCube Neutrino Observatory: Instrumentation and Online Systems". In: *JINST* 12.03 (2017), P03012. DOI: 10.1088/1748-0221/12/03/P03012. arXiv: 1612.05093 [astro-ph.IM].

[36] Rene A. Ong. "Cherenkov Telescope Array: The Next Generation Gamma-ray Observatory". In: *PoS* ICRC2017 (2018), p. 1071. DOI: 10.22323/1.301.1071. arXiv: 1709.05434 [astro-ph.HE].

[37] R. Aloisio, V. Berezinsky, and P. Blasi. "Ultra high energy cosmic rays: implications of Auger data for source spectra and chemical composition". In: *JCAP* 1410.10 (2014), p. 020. DOI: 10.1088/1475-7516/2014/10/020. arXiv: 1312.7459 [astro-ph.HE].

[38] Andreas Haungs. "Cosmic Rays from the Knee to the Ankle". In: *Phys. Procedia* 61 (2015), pp. 425–434. DOI: 10.1016/j.phpro.2014.12.094. arXiv: 1504.01859 [astro-ph.HE].

[39] Pasquale Blasi. "The Origin of Galactic Cosmic Rays". In: *Astron. Astrophys. Rev.* 21 (2013), p. 70. DOI: 10.1007/s00159-013-0070-7. arXiv: 1311.7346 [astro-ph.HE].

[40] Venya Berezinsky. "Transition from galactic to extragalactic cosmic rays". In: 6 (2007), pp. 21–33. arXiv: 0710.2750 [astro-ph].

[41] R. Aloisio, V. Berezinsky, and A. Gazizov. "Transition from galactic to extragalactic cosmic rays". In: *Astropart. Phys.* 39-40 (2012), pp. 129–143. DOI: 10.1016/j.astropartphys.2012.09.007. arXiv: 1211.0494 [astro-ph.HE].

[42] G. Giacinti, M. Kachelrieß, and D. V. Semikoz. "Escape model for Galactic cosmic rays and an early extragalactic transition". In: *Phys. Rev. D* 91 (8 Apr. 2015), p. 083009. DOI: 10.1103/PhysRevD.91.083009. URL: https://link.aps.org/doi/10.1103/PhysRevD.91.083009.

[43] N. M. Budnev, A. L. Ivanova, and N. N. Kalmykov. "Investigations of the Transition Region between Galactic and Extragalactic Cosmic Rays with Arrays for Extensive Air-Shower Detection". In: *Moscow University Physics Bulletin* 72.6 (Nov. 2017), pp. 493–506. ISSN: 1934-8460. DOI: 10.3103/S0027134917060054. URL: https://doi.org/10.3103/S0027134917060054.

[44] Elihu Boldt and Pranab Ghosh. "Cosmic rays from remnants of quasars?" In: *Monthly Notices of the Royal Astronomical Society* 307.3 (1999), pp. 491–494. DOI: 10.1046/j.1365-8711.1999.02600.x. eprint: /oup/backfile/content_public/journal/mnras/307/3/10.1046/j.1365-8711.1999.02600.x/2/307-3-491.pdf. URL: http://dx.doi.org/10.1046/j.1365-8711.1999.02600.x.

[45] Kumiko Kotera and Angela V. Olinto. "The Astrophysics of Ultrahigh Energy Cosmic Rays". In: *Ann. Rev. Astron. Astrophys.* 49 (2011), pp. 119–153. DOI: 10.1146/annurev-astro-081710-102620. arXiv: 1101.4256 [astro-ph.HE].

[46] K. Mannheim. "The Proton blazar". In: *Astron. Astrophys.* 269 (1993), p. 67. arXiv: astro-ph/9302006 [astro-ph].

[47] Jorg P. Rachen and Peter L. Biermann. "Extragalactic ultrahigh-energy cosmic rays. 1. Contribution from hot spots in FR-II radio galaxies". In: *Astron. Astrophys.* 272 (1993), pp. 161–175. arXiv: astro-ph/9301010 [astro-ph].

[48] P. L. Biermann. "Synchrotron Emission from Shock Waves in Active Galactic Nuclei". In: *High Energy Astrophysics*. Ed. by Gerhard Börner. Berlin, Heidelberg: Springer Berlin Heidelberg, 1988, pp. 134–143.

[49] Björn Eichmann et al. "Ultra-High-Energy Cosmic Rays from Radio Galaxies". In: *JCAP* 1802.02 (2018), p. 036. DOI: 10.1088/1475-7516/2018/02/036. arXiv: 1701.06792 [astro-ph.HE].

[50] Joydeep Bagchi et al. "Evidence for shock acceleration and intergalactic magnetic fields in a large scale filament of galaxies ZwC1 2341.1+0000". In: *New Astron.* 7 (2002), p. 249. DOI: 10.1016/S1384-1076(02)00137-9. arXiv: astro-ph/0204389 [astro-ph].

[51] Julian Candia and Esteban Roulet. "Diffusion and drift of cosmic rays in highly turbulent magnetic fields". In: *JCAP* 0410 (2004), p. 007. DOI: 10.1088/1475-7516/2004/10/007. arXiv: astro-ph/0408054 [astro-ph].

[52] Daniel De Marco, Pasquale Blasi, and Todor Stanev. "Numerical propagation of high energy cosmic rays in the Galaxy: I. Technical issues". In: *Journal of Cosmology and Astroparticle Physics* 2007.06 (2007), p. 027. URL: http://stacks.iop.org/1475-7516/2007/i=06/a=027.

[53] Andrey Beresnyak, Huirong Yan, and A Lazarian. "Numerical study of Cosmic Ray Diffusion in MHD turbulence". In: (Feb. 2010).

[54] Julian Candia, Silvia Mollerach, and Esteban Roulet. "Cosmic ray spectrum and anisotropies from the knee to the second knee". In: *JCAP* 0305 (2003), p. 003. DOI: 10.1088/1475-7516/2003/05/003. arXiv: astro-ph/0302082 [astro-ph].

[55] S. Mollerach and E. Roulet. "Progress in high-energy cosmic ray physics". In: *Prog. Part. Nucl. Phys.* 98 (2018), pp. 85–118. DOI: 10.1016/j.ppnp.2017.10.002. arXiv: 1710.11155 [astro-ph.HE].

[56] G. V. Kulikov and G. B. Khristiansen. In: *J. Exptl Theoret. Phys. (USSR)* 35 (1958), p. 635.

[57] N. Kalmykov. "The regular galactic magnetic field and primary cosmic ray energy spectrum at the knee region". In: *International Cosmic Ray Conference* 4 (1999), p. 263.

[58] Peter L. Biermann et al. "Cosmic-Ray Transport and Anisotropies". In: *The Astrophysical Journal* 768.2 (2013), p. 124. URL: http://stacks.iop.org/0004-637X/768/i=2/a=124.

[59] Markus Ahlers. "Deciphering the Dipole Anisotropy of Galactic Cosmic Rays". In: *Phys. Rev. Lett.* 117 (15 Oct. 2016), p. 151103. DOI: 10.1103/PhysRevLett.117.151103. URL: https://link.aps.org/doi/10.1103/PhysRevLett.117.151103.

[60] Rafael Alves Batista et al. "Probing Intergalactic Magnetic Fields with Simulations of Electromagnetic Cascades". In: *Phys. Rev.* D94.8 (2016), p. 083005. DOI: 10.1103/PhysRevD.94.083005. arXiv: 1607.00320 [astro-ph.HE].

[61] Ronnie Jansson and Glennys R. Farrar. "A New Model of the Galactic Magnetic Field". In: *The Astrophysical Journal* 757.1 (2012), p. 14. URL: http://stacks.iop.org/0004-637X/757/i=1/a=14.

[62] Ryogo Kubo. "Statistical-Mechanical Theory of Irreversible Processes. I. General Theory and Simple Applications to Magnetic and Conduction Problems". In: *Journal of the Physical Society of Japan* 12.6 (1957), pp. 570–586. DOI: 10.1143/JPSJ.12.570. eprint: https://doi.org/10.1143/JPSJ.12.570. URL: https://doi.org/10.1143/JPSJ.12.570.

[63] Andreas Shalchi. *Nonlinear Cosmic Ray Diffusion Theories*. Vol. 362. Jan. 2009.

[64] J. R. Jokipii. "Cosmic-Ray Propagation. I. Charged Particles in a Random Magnetic Field". In: 146 (Nov. 1966), p. 480. DOI: 10.1086/148912.

[65] R. Schlickeiser. *Cosmic Ray Astrophysics*. 2002.

[66] M. A. Malkov. "Exact solution of the Fokker-Planck equation for isotropic scattering". In: *Phys. Rev.* D95.2 (2017), p. 023007. DOI: 10.1103/PhysRevD.95.023007. arXiv: 1610.01584 [astro-ph.HE].

[67] R. C. Tautz. "Pitch-angle scattering in magnetostatic turbulence. II. Analytical considerations and pitch-angle isotropization". In: *Astron. Astrophys.* 558 (2013), A148. DOI: 10.1051/0004-6361/201322143. arXiv: 1309.7838 [astro-ph.HE].

[68] R C Tautz, A Shalchi, and R Schlickeiser. "Comparison between test-particle simulations and test-particle theories for cosmic ray transport: I. Magnetostatic turbulence". In: *Journal of Physics G: Nuclear and Particle Physics* 32.6 (2006), p. 809. URL: http://stacks.iop.org/0954-3899/32/i=6/a=006.

[69] J. W. Bieber, C. W. Smith, and W. H. Matthaeus. "Cosmic-ray pitch-angle scattering in isotropic turbulence". In: 334 (Nov. 1988), pp. 470–475. DOI: 10.1086/166851.

[70] V. S. Berezinskii et al. *Astrophysics of cosmic rays*. 1990.

[71] P. Subedi et al. "Charged Particle Diffusion in Isotropic Random Magnetic Fields". In: *The Astrophysical Journal* 837.2 (2017), p. 140. URL: http://stacks.iop.org/0004-637X/837/i=2/a=140.

[72] L. A. Fisk and J. W. Sari. "Correlation length for interplanetary magnetic field fluctuations." In: *Journal of Geophysical Research* 78.1 (1973), pp. 6729–6736. URL: https://ntrs.nasa.gov/search.jsp?R=19730060323.

[73] Tilman Dannert. "Gyrokinetische Simulation von Plasmaturbulenz mit gefangenen Teilchen und elektromagnetischen Effekten". In: *Dissertation* (16.11.2004).

[74] J. R. Jokipii. "The Rate of Separation of Magnetic Lines of Force in a Random Magnetic Field". In: 183 (Aug. 1973), pp. 1029–1036. DOI: 10.1086/152289.

[75] Etienne Parizot. "GZK horizon and magnetic fields". In: *Nucl. Phys. Proc. Suppl.* 136 (2004). [,169(2004)], pp. 169–178. DOI: 10.1016/j.nuclphysbps.2004.10.034. arXiv: astro-ph/0409191 [astro-ph].

[76] N. Globus, D. Allard, and E. Parizot. "Propagation of high-energy cosmic rays in extragalactic turbulent magnetic fields: resulting energy spectrum and composition". In: *Astron. Astrophys.* 479 (2008), p. 97. DOI: 10.1051/0004-6361:20078653. arXiv: 0709.1541 [astro-ph].

[77] Diego Harari, Silvia Mollerach, and Esteban Roulet. "Anisotropies of ultrahigh energy cosmic rays diffusing from extragalactic sources". In: *Phys. Rev.* D89.12 (2014), p. 123001. DOI: 10.1103/PhysRevD.89.123001. arXiv: 1312.1366 [astro-ph.HE].

[78] Diego Harari, Silvia Mollerach, and Esteban Roulet. "Anisotropies of ultrahigh energy cosmic ray nuclei diffusing from extragalactic sources". In: *Phys. Rev.* D92.6 (2015), p. 063014. DOI: 10.1103/PhysRevD.92.063014. arXiv: 1507.06585 [astro-ph.HE].

[79] Plotnikov, I., Pelletier, G., and Lemoine, M. "Particle transport in intense small-scale magnetic turbulence with a mean field". In: *A&A* 532 (2011), A68. DOI: 10.1051/0004-6361/201117182. URL: https://doi.org/10.1051/0004-6361/201117182.

[80] M. Fatuzzo et al. "High-energy Cosmic-ray Diffusion in Molecular Clouds: A Numerical Approach". In: *The Astrophysical Journal* 725.1 (2010), p. 515. URL: http://stacks.iop.org/0004-637X/725/i=1/a=515.

[81] J. R. Cash and Alan H. Karp. "A Variable Order Runge-Kutta Method for Initial Value Problems with Rapidly Varying Right-hand Sides". In: *ACM Trans. Math. Softw.* 16.3 (Sept. 1990), pp. 201–222. ISSN: 0098-3500. DOI: 10.1145/79505.79507. URL: http://doi.acm.org/10.1145/79505.79507.

[82] Hong Qin et al. "Why is Boris algorithm so good?" In: *Physics of Plasmas* 20.8 (2013), p. 084503. DOI: 10.1063/1.4818428. URL: https://doi.org/10.1063/1.4818428.

[83] Mathias Winkel, Robert Speck, and Daniel Ruprecht. "Does Boris-SDC conserve phase space volume?" In: *PAMM* 15.1 (2015), pp. 687–688. DOI: 10.1002/pamm.201510333. URL: https://onlinelibrary.wiley.com/doi/abs/10.1002/pamm.201510333.

[84] Kyle Parfrey. "Stumbling Towards Simulations of Collisionless Black Hole Accretion Flows". In: *Einstein Fellows Symposium* (). URL: http://cxc.harvard.edu/fellows/symp_presentations/2016/Parfrey_Kyle_EinsteinSymposium2016.pdf.

[85] Frank C. Jones, J. Randy Jokipii, and Matthew G. Baring. "Charged-Particle Motion in Electromagnetic Fields Having at Least One Ignorable Spatial Coordinate". In: *The Astrophysical Journal* 509.1 (1998), p. 238. URL: http://stacks.iop.org/0004-637X/509/i=1/a=238.

[86] C. J. Cesarsky and R. M. Kulsrud. "Role of Hydromagnetic Waves in Cosmic-Ray Confinement in the Disk. Theory of Behavior in General Wave Spectra". In: 185 (Oct. 1973), pp. 153–166. DOI: 10.1086/152405.

[87] G. M. Felice and R. M. Kulsrud. "Cosmic-Ray Pitch-Angle Scattering through 90 degree". In: 553 (May 2001), pp. 198–210. DOI: 10.1086/320651.

[88] R. Aloisio and Veniamin Berezinsky. "Diffusive propagation of UHECR and the propagation theorem". In: *Astrophys. J.* 612 (2004), pp. 900–913. DOI: 10.1086/421869. arXiv: astro-ph/0403095 [astro-ph].

[89] J Jokipii and E N. Parker. "Stochastic Aspects of Magnetic Lines of Force with Application to Cosmic-Ray Propagation". In: 155 (Apr. 1969).

[90] John W. Bieber and William H. Matthaeus. "Perpendicular Diffusion and Drift at Intermediate Cosmic-Ray Energies". In: *The Astrophysical Journal* 485.2 (1997), p. 655. URL: http://stacks.iop.org/0004-637X/485/i=2/a=655.

[91] M. Ackermann et al. "The spectrum of isotropic diffuse gamma-ray emission between 100 MeV and 820 GeV". In: *Astrophys. J.* 799 (2015), p. 86. DOI: 10.1088/0004-637X/799/1/86. arXiv: 1410.3696 [astro-ph.HE].

[92] F. Acero et al. "Fermi Large Area Telescope Third Source Catalog". In: *Astrophys. J. Suppl.* 218.2 (2015), p. 23. DOI: 10.1088/0067-0049/218/2/23. arXiv: 1501.02003 [astro-ph.HE].

[93] F. Aharonian et al. "Discovery of very high energy gamma-ray emission from Centaurus A with H.E.S.S". In: *Astrophys. J.* 695 (2009), pp. L40–L44. DOI: 10.1088/0004-637X/695/1/L40. arXiv: 0903.1582 [astro-ph.CO].

[94] Michal Dyrda et al. "Discovery of VHE gamma-rays from the radio galaxy PKS 0625-354 with H.E.S.S". In: *PoS* ICRC2015 (2016), p. 801. DOI: 10.22323/1.236.0801. arXiv: 1509.06851 [astro-ph.HE].

[95] M. G. Aartsen et al. "First observation of PeV-energy neutrinos with IceCube". In: *Phys. Rev. Lett.* 111 (2013), p. 021103. DOI: 10.1103/PhysRevLett.111.021103. arXiv: 1304.5356 [astro-ph.HE].

[96] Kohta Murase, Markus Ahlers, and Brian C. Lacki. "Testing the Hadronuclear Origin of PeV Neutrinos Observed with IceCube". In: *Phys. Rev.* D88.12 (2013), p. 121301. DOI: 10.1103/PhysRevD.88.121301. arXiv: 1306.3417 [astro-ph.HE].

[97] L. Oc. Drury. "An introduction to the theory of diffusive shock acceleration of energetic particles in tenuous plasmas". In: *Rept. Prog. Phys.* 46 (1983), pp. 973–1027. DOI: 10.1088/0034-4885/46/8/002.

[98] Mattia Di Mauro and Fiorenza Donato. "Composition of the Fermi-LAT isotropic gamma-ray background intensity: Emission from extragalactic point sources and dark matter annihilations". In: *Phys. Rev.* D91.12 (2015), p. 123001. DOI: 10.1103/PhysRevD.91.123001. arXiv: 1501.05316 [astro-ph.HE].

[99] Andrew M. Taylor. "UHECR Composition Models". In: *Astropart. Phys.* 54 (2014), pp. 48–53. DOI: 10.1016/j.astropartphys.2013.11.006. arXiv: 1401.0199 [astro-ph.HE].

[100] Andrew M. Taylor, Markus Ahlers, and Felix A. Aharonian. "Need for a local source of ultrahigh-energy cosmic-ray nuclei". In: *Phys. Rev. D* 84 (10 Nov. 2011), p. 105007. DOI: 10.1103/PhysRevD.84.105007. URL: https://link.aps.org/doi/10.1103/PhysRevD.84.105007.

[101] M. G. Aartsen et al. "IceCube-Gen2 - The Next Generation Neutrino Observatory at the South Pole: Contributions to ICRC 2015". In: (2015). arXiv: 1510.05228 [astro-ph.IM].

[102] S. Adrian-Martinez et al. "Letter of intent for KM3NeT 2.0". In: *J. Phys.* G43.8 (2016), p. 084001. DOI: 10.1088/0954-3899/43/8/084001. arXiv: 1601.07459 [astro-ph.IM].

[103] Francis Halzen and Dan Hooper. "IceCube-Plus: An Ultrahigh-energy neutrino telescope". In: *JCAP* 0401 (2004), p. 002. DOI: 10.1088/1475-7516/2004/01/002. arXiv: astro-ph/0310152 [astro-ph].

[104] G. K. Batchelor. *The Theory of Homogeneous Turbulence*. 1953.

Acknowledgment

I would like to thank my supervisor Prof. Dr. Julia Tjus for providing me with such a compelling research topic and for her excellent support during my Master's thesis. I am also grateful for the contact to Prof. Dr. Ellen Zweibel initialized by her. Many thanks go out to Ellen Zweibel for introducing me to the world of pitch angle scattering and providing deep insight into the microphysics and macrophysics of cosmic rays as well as being an outstanding host during my stay in Chicago and Madison. Dr. Moritz Püschel was at hand for practically every question concerning my thesis and provided me with fruitful discussions and suggestions for the thesis for which I am really thankful. Additional thanks go to Dr. Daniel Told for agreeing to be on my board of examiners.
I really appreciate the help of the local CRPropa development team lead by Lukas Merten. Lukas Merten was also most supportive during the first weeks and months when everything seemed like a big mystery and only few findings agreed with results of other publications. Among the many from the institute who deserve acknowledgment, I would like to name Julia Ebeling, Lenka Tomankova, Johan Wulff, Anke Yusafzai and Karolin Hymon. I am thankful to the German academic exchange service for providing me with the financial support during my time abroad.
In addition, I would like to thank my parents and family for their support. My deepest thanks and devotion go to my love, Julia Suc.